Wide-angle radiation pattern calculation of paraboloidal reflector antennas : a comparative study

tu/e
Research Report
ISSN 0167-9708
Coden: TEUEDE

Eindhoven
University of Technology
Netherlands

Faculty of Electrical Engineering

Wide-angle Radiation Pattern Calculation of Paraboloidal Reflector Antennas:

A Comparative Study

by
J. Chen
P.J.I. de Maagt
M.H.A.J. Herben

EUT Report 91-E-252
ISBN 90-6144-252-4
June 1991

Eindhoven University of Technology Research Reports

EINDHOVEN UNIVERSITY OF TECHNOLOGY

Faculty of Electrical Engineering
Eindhoven The Netherlands

ISSN 0167–9708 Coden:TEUEDE

WIDE–ANGLE RADIATION PATTERN CALCULATION OF PARABOLOIDAL REFLECTOR ANTENNAS: A COMPARATIVE STUDY

by
J.Chen
P.J.I. de Maagt
M.H.A.J. Herben

EUT Report 91–E–252
ISBN 90–6144–252–4

EINDHOVEN
JUNE 1991

CIP–GEGEVENS KONINKLIJKE BIBLIOTHEEK, DEN HAAG

Chen, J.

Wide–angle radiation pattern calculation of paraboloidal reflector antennas: a comparative study / by J. Chen, P.J.I. de Maagt, M.H.A.J. Herben. – Eindhoven: Eindhoven University of Technology, Faculty of Electrical Engineering.
– Fig., tab. – (EUT report, ISSN 0167–9708; 91–E–252)
Met lit. opg., reg.
ISBN 90–6144–252–4
NUGI 832
Trefw.: reflectorantennes.

Abstract

In the first part of the report, the complete radiation pattern of a symmetrical paraboloidal reflector antenna is calculated by high–frequency asymptotic techniques. These techniques are reviewed and the diffraction coefficients, derived for GTD, UTD, APO, and CAPO, are compared. The angle regions in which these methods are valid, are discussed and some associated conflicting statements in literature are cleared up. It is shown that GTD (or UTD) is the most successful method to calculate the scattered field for reflector antennas in wide–angle (away from the antenna axis) regions. To obtain the correct results in the forward– and rear–axial region, the PO and EEC method are used, respectively. The results obtained agree well with previous theoretical and experimental work.

In the second part of the report, the wide–angle radiation pattern of an offset paraboloidal reflector antenna is calculated using the successful GTD (UTD) method. It is shown that there are two far–field caustics in the symmetry plane of the offset configuration: one in the antenna forward–direction and one at a specific angle determined by the offset configuration. In the latter caustic–region the EEC method is used. Outside the symmetry plane specific far–field angles are found where GTD fails; this phenomenon is explained with the help of far–field "caustic" points. To obtain the complete power pattern, PO is used in the forward axial–region.

Chen, J. and P.J.I. de Maagt, M.H.A.J. Herben
WIDE-ANGLE RADIATION PATTERN CALCULATION OF PARABOLOIDAL REFLECTOR ANTENNAS: A COMPARATIVE STUDY.
Faculty of Electrical Engineering, Eindhoven University of Technology, The Netherlands, 1991.
EUT Report 91-E-252

Address of the authors:

Telecommunications Division,
Faculty of Electrical Engineering,
Eindhoven University of Technology,
P.O. Box 513,
5600 MB EINDHOVEN,
The Netherlands

Acknowledgements

Firstly, the authors would like to thank the Chinese Government and Chengdu Aircraft Company for their financial support and for giving mr. Chen the opportunity to work at the Eindhoven University of Technology for the period from September, 1989 to December, 1990.

Furthermore, we want to thank prof.dr.ir. G. Brussaard for his continued interest.

Finally, we want to thank dr. P.R. Attwood for reading and correcting the grammar of the original version of this report.

TABLE OF CONTENTS PAGE

Abstract

Acknowledgements

Contents 1

1 Introduction 4

2 Reflector Configuration and Feed Patterns 7
2.1 Configuration and Coordinate Systems 7
2.2 Feed Radiation Patterns 7

3 Far–Field Angle Region Definition 10

4 GTD Analysis of the Radiation from Paraboloidal Structures 12
4.1 Introduction 12
4.2 Calculation of the Caustic Divergence Factor 14
4.2.1 $A_1(\rho_{c1},s_1^d)$ for the Upper Point Q_1 15
4.2.2 $A_2(\rho_{c2},s_2^d)$ for the Lower Point Q_2 16
4.3 Calculation of the Diffraction Coefficients 17
4.3.1 Diffraction Coefficient for the Upper Point Q_1 20
4.3.2 Diffraction Coefficient for the Lower Point Q_2 24
4.4 The Total Field 28
4.5 Modification of GTD 31
4.6 Comparison with Literature 31

5 APO Analysis of the Radiation from Paraboloidal Structures 33
5.1 Introduction 33
5.2 Current Calculation by GO 33
5.3 Field Integration by Stationary Phase Method 34
5.4 APO Method for the Shadow Boundary Region 43
5.5 Corrected APO (CAPO) 44

6 Caustic Region Analysis by EEC 49
6.1 Introduction 49
6.2 Equivalent Edge Current Calculation 49
6.3 Edge Current Integration 53

7 Comparison of the Different High Frequency Asymptotic Techniques 57
7.1 Comparison of GTD and UTD 57
7.2 Comparison of APO and CAPO 58
7.3 Comparison of GTD (UTD) and APO (CAPO) 59
7.3.1 Diffraction Coefficient Comparison of GTD and APO 59
7.3.2 Radiation Pattern Comparison of UTD and APO 64
7.3.3 Radiation Pattern Comparison of UTD and CAPO 64
7.4 Transition Region Between EEC and GTD (UTD) 64
7.5 Transition Region Between PO and GTD (UTD) 71

8 Offset Paraboloidal Reflector Antenna Configuration 74
8.1 Reflector Geometry 74
8.2 Feed Radiation Properties 76

9 Radiation Pattern Analysis by GTD (UTD) for an Offset Paraboloidal Reflector Antenna 77
9.1 Introduction 77
9.2 GTD Diffraction Point Location for an Offset Configuration 77
9.2.1 Coordinate Transformation 78
9.2.2 Diffraction Cone Formed at the Edge Diffraction Points 81
9.2.3 Diffraction Point Location 84
9.2.3.1 Diffraction Points for the E–plane Pattern Calculation 84
9.2.3.2 Diffraction Points for the H–plane Pattern Calculation 86
9.2.3.3 Diffraction Points for an Arbitrary Plane 88
9.2.3.4 Stationary Phase Method(APO) 89
9.2.3.5 Caustics in the Symmetry Plane 94
9.2.3.6 Conclusion for the E– and H–plane Diffraction Point Analysis 96

9.3 Radiation Pattern Calculation 96
9.3.1 E–plane Pattern Calculation 97
9.3.1.1 Caustic Divergence Factor Calculation 97
9.3.1.1.1 Caustic Divergence Factor for the Upper Point 98
9.3.1.1.2 Caustic Divergence Factor for the Lower Point 100
9.3.1.2 Diffraction Coefficient Calculation 101
9.3.1.2.1 Diffraction Coefficients for the Upper Point 102
9.3.1.2.2 Diffraction Coefficients for the Lower Point 103
9.3.1.3 Incident Field at the Edge of the Reflector 104
9.3.1.4 Far–field Pattern Calculation 106
9.3.1.4.1 Contribution of the Upper Point to the Far–field 106
9.3.1.4.2 Contribution of the Lower Point to the Far–field 108
9.3.1.4.3 Total Radiation Pattern in E–plane 110

9.3.2 Arbitrary ϕ–plane Pattern Calculation 110
9.3.2.1 Caustic Divergence Factor Calculation 111
9.3.2.2 Diffraction Coefficient Calculation 114
9.3.2.3 Incident Field at the Edge of the Reflector 116
9.3.2.4 Diffracted Field from the Diffraction Point 119
9.3.2.5 Total Radiation Pattern in an Arbitrary ϕ–plane 120

10 EEC Method for the Far–field Caustic in the Symmetry Plane 121
10.1 EEC for an Offset Configuration 121

11 Numerical Results and Discussions 124
11.1 Offset Configuration 124
11.2 Numerical results 124
11.3 Pattern Discontinuities 134

12 Conclusions 137

References 139

1. Introduction

Reflector antennas have been used for about fifty years in radio astronomy, microwave communication, remote sensing and satellite tracking. The demand for highly sensitive antenna systems asks for an accurate calculation of the wide–angle and the rear–direction antenna patterns in order to examine the harm caused by possible interfering sources within this angle region. Several methods ([1]–[4]) have been introduced to calculate the far–field radiation patterns of reflector antennas. To find the angle region where the results obtained by these methods are valid, some potential methods are reviewed and compared in this report. These methods are GTD [5], UTD [6], APO [7], CAPO [8] and EEC ([9]–[11]).

The geometrical theory of diffraction (GTD) ([12],[13]) introduced by Keller, is an extension of the geometrical optics (GO) by adding diffraction rays to the usual GO ray. The corresponding diffracted waves are assumed to follow the laws of diffraction and to diverge according to GO laws. Consequently, the points of diffraction and the paths of the rays can be found from the laws of diffraction, and the amplitude of the fields along the rays can be found from the principle of energy conservation. So, this theory not only provides a qualitative description of diffraction in terms of the diffracted rays, but also permits a quantitative determination of the diffracted field as well. The initial value of the diffracted field at the point of diffraction is obtained by multiplying the field vector of the incident wave by the dyadic diffraction coefficient, which was first obtained by Keller by comparing his diffraction expressions with Sommerfeld's exact solutions for various canonical problems. Although the GTD results are not exact solutions to the field equations, they are the leading terms of an asymptotic expansion of such solutions for high frequencies. GTD has been widely used to calculate the scattered fields of objects which dimensions are large compared to the wavelength. However, it gives invalid results within a few specific far–field angle–regions.

Kouyoumjian and Pathak [6] extended Keller's GTD to the uniform geometrical theory of diffraction (UTD). UTD gives diffraction coefficients which are also valid in the shadow boundary regions where Keller's theory fails. Moreover, UTD gives a compact form of the dyadic diffraction coefficient for electromagnetic waves obliquely incident on a curved edge (of a perfectly conducting reflector surface). In this report, the term GTD is used for both Keller's GTD and UTD, since the latter is basically an extension of the first and they are based on the same principles.

Physical Optics (PO), simply approximates the currents on the reflector by

the currents derived from the application of the GO theory. By evaluating the contributions from all parts of the reflector to the field in an observation point, PO gives the total field. PO is generally used for the calculation of the main–lobe and the first few sidelobes which appear in an angle–region where GTD fails. The wide–angle far–field calculation using this method is usually complex and includes time consuming numerical integrals. But, if there are stationary points in the integral, so that the stationary phase method can be used, the field integrals can be evaluated asymptotically. The method using stationary phase integration is called Asymptotic Physical Optics (APO). The APO, which was first adopted by Rusch ([7],[14]) and later on extended by Knop [15], has been considered to be a powerful method for the reflector antenna radiation pattern calculation. However, measurements [8] revealed that APO gives results with errors up to 6 dB in some angle regions. These errors can be explained by the unreliable physical optics (PO) approximation of the currents at the edge of the reflector. Therefore Knop and Ostertag [8] derived the corrected APO (CAPO) diffraction coefficients by introducing multiplication factors.

The equivalent edge current method (EEC or ECM) is used to obtain the rear–direction patterns of paraboloidal reflector antennas ([9],[10]) which cannot be calculated with GTD or APO. Therefore, electric and magnetic currents flowing along the edge of the reflector are introduced, which are derived from the GTD edge diffraction coefficients.

In the first part of this report, the wide–angle radiation patterns of axially symmetrical paraboloidal reflector antennas are calculated. In Chapter 2 the configuration of the reflector antenna and its feed radiation patterns are given. The different far–field angle regions are described in Chapter 3, which shows that in each region a different calculation method should be used. In Chapters 4 and 5 the GTD (UTD) method and the APO (CAPO) method are described. The EEC method is dealt with in Chapter 6. In Chapter 7, the calculation methods are compared, using the results of a PASCAL computer program, which was written by the first author.

It is concluded that GTD (UTD) is the most successful method for calculating the scattered field for reflector antennas in wide–angle regions. To obtain the correct results in the forward and rear–axial region, the PO and EEC must be used, respectively. To enssure a smooth transition between the GTD results and those of both other techniques, the transition angle–regions are evaluated in Chapter 7.

The second part of the report deals with the offset paraboloidal reflector antenna[20] which is in use for many years. Compared with the front–fed symmetrical paraboloidal reflector antenna, the offset configuration is free from aperture–blockage

by the feed system and consequently it has a better radiation pattern and VSWR [1]. Its main disadvantage is an inherent cross–polarization, which however can be eliminated in case of an offset double–reflector antenna configuration. Because of these advantages, a lot of attention was paid to the design of the offset parabolic reflector antenna.

However, designing an offset parabolic reflector antenna asks for a more complex theoretical analysis, because its asymmetric geometry results in numerical calculation difficulties. Most of the analyses for offset reflector antennas are based on the work performed by Cook et al.[21], either by making use of the same geometry, or by following a similar approach to a different geometry. All these methods can be classified as being related to the Physical Optics (PO) theory, by using the current–distribution method or the aperture–field integration method. Because these methods can only be used in a limited angle region, another method is needed to calculate the wide–angle radiation pattern.

In this report, the GTD (UTD), which was successfully used for the symmetrical antenna, has been modified so that it can be used for the calculation of the wide–angle radiation pattern of an offset reflector antenna. The papers published on this subject are few [26]. For the analysis of the offset reflector configuration, a two–dimensional diffraction model, as used for the symmetrical configuration, is generally not sufficient and a three–dimensional model is needed. It appears that, because of the asymmetric geometry, one of the caustics which was found for the symmetrical antenna to be in the rear–axial direction, now appears in the symmetry plane at a certain angle with the rear–axial direction.

Chapter 8 of this report describes the offset reflector geometry and the radiation properties of the feed. The corresponding coordinate systems used for the reflector and the feed, and the relation between them are also given in this chapter. In chapter 9 it is shown that the positions of the GTD diffraction points are the same as the positions of the stationary phase points derived by Ierley et al.[23]. Further, expressions for the diffraction coefficients and the radiation patterns of an offset paraboloidal reflector antenna are derived using the GTD (UTD) method. As for the symmetrical antenna, PO is used in the forward–caustic direction, and the EEC method is used at or near the other caustic direction. The use of EEC in this caustic direction is discussed in Chapter 10. The transition angle regions for the three calculation techniques are considered in Chapter 11, where also numerical results are presented from a PASCAL computer program written by the first author. Finally, the conclusions of this research are given in Chapter 12.

2. Reflector Configuration and Feed Patterns

In the first part of this report, the axially symmetric paraboloidal reflector antenna will be considered. Due to its symmetry, the radiation properties of such an antenna can be described more easily than those of the asymmetric offset antenna, which will be dealt with in the second part of this report. It should be noted that possible blockage effects of struts and feed are not considered in this study.

2.1 Configuration and Coordinate Systems

The paraboloidal reflector with focal length f and subtended angle $2a$ is placed in the $z>0$ region of the rectangular coordinate system (see Fig. 2–1). The z–axis is the symmetry axis of the antenna and the feed is placed at the focus (F), which is positioned at the origin of the rectangular (x,y,z) coordinate system. The O' and the O" are the intersections of the z–axis with the aperture plane and reflector surface, respectively.

The paraboloid is given by:

$$\rho = \frac{2f}{1+\cos\psi} \qquad (\psi \le a); \qquad (2\text{–}1)$$

where: (ρ,ψ,ξ) denotes the spherical coordinates to describe the reflection and diffraction points on the paraboloidal reflector and (r,θ,ϕ) are the spherical coordinates indicating the far–field observation point.

2.2 Feed Radiation Patterns

If both Huygens– and dipole feed polarization are considered, the far–field pattern of the feed can, for y–polarization, be written as:

$$\vec{E}_f(\rho,\psi,\xi) = A_0 \frac{e^{-jk\rho}}{\rho} \sqrt{G_f(\psi,\xi)} \left[U_\psi \sin\xi \, \vec{\psi} + \cos\xi \, \vec{\xi} \right] \qquad (2\text{–}2)$$

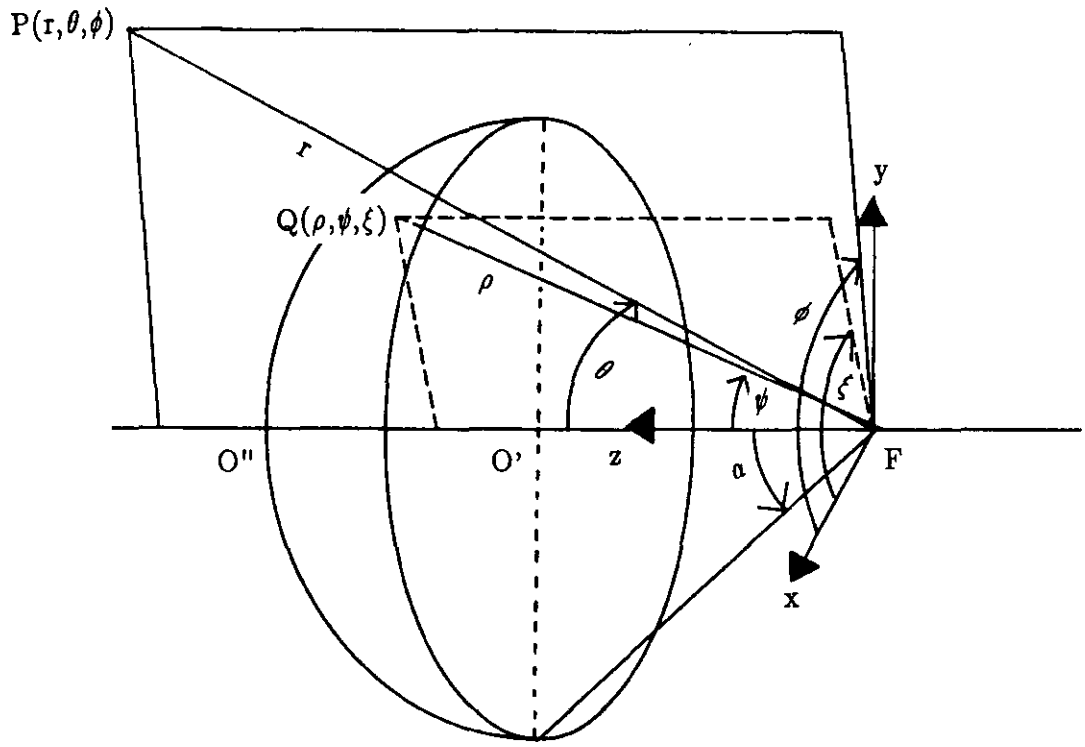

Fig. 2–1 The Geometry of a Paraboloidal Reflector

with

$$U_{\psi} = \begin{cases} \cos\psi & \text{for dipole feed} \\ 1 & \text{for Huygens feed} \end{cases} \qquad (2\text{–}3,a)$$

$$A_0 = \begin{cases} \dfrac{(\eta \frac{P_t}{2\pi})^{\frac{1}{2}}}{\sqrt{1-\sin^2\psi\sin^2\xi}} & \text{for dipole feed} \\ (\eta \frac{P_t}{2\pi})^{\frac{1}{2}} & \text{for Huygens feed} \end{cases} \qquad (2\text{–}3,b)$$

where P_t is the total power radiated by the feed, η the intrinsic impedance of free space, $k = \frac{2\pi}{\lambda}$ the wave number and λ the wavelength.

The feed power functions considered are:

$$G_f(\psi)=\begin{cases} 2(n+1)\cos^n(\psi) & (\psi \le \frac{\pi}{2}) \quad (2\text{–}4,a) \\ 0 & (\psi > \frac{\pi}{2}) \quad (2\text{–}4,b) \end{cases}$$

where n is a positive real.

The electric field incident to the edge of the reflector is obtained from Eq.(2–2) by setting $\psi = \alpha$ and replacing ρ by ρ_0, being the distance from the feed to the edge of the reflector.

3 Far–Field Angle Region Definition

According to geometrical optics, the direct feed radiation is shadowed by the reflector when θ is less than a (see Fig. 3–1). Therefore, we call the region $\theta<a$ the shadow region, the region $\theta>a$ the illuminated region, and the angle $\theta=a$ the shadow boundary.

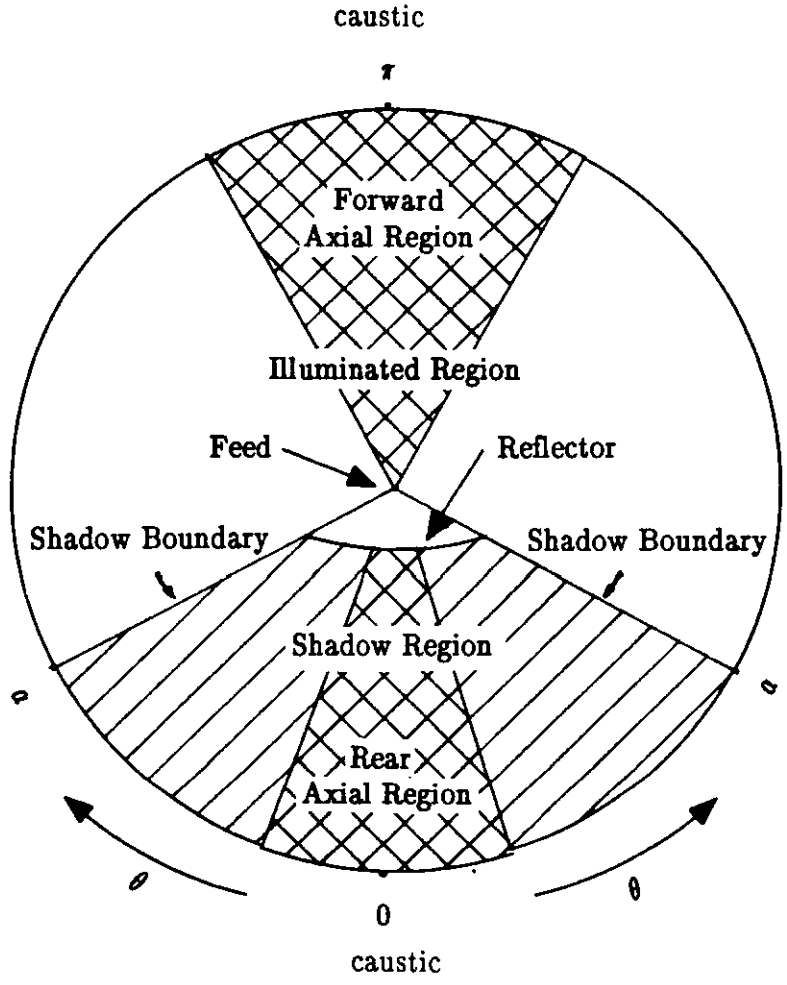

Fig. 3–1 Angle Regions of Far–field Radiation

Due to the focussing properties of the symmetrical parabolic reflector, the forward–direction ($\theta=\pi$) is a caustic of the reflected rays and due to its rotational symmetry with respect to the z–axis, both the forward– and rear–direction ($\theta=0$) are caustics of the diffracted rays from the edge of the reflector. The regions in the vicinity of $\theta=\pi$ and $\theta=0$ directions are named the forward–axial and rear–axial region, respectively.

All the angle regions and the associated fields are listed in Table I. Here, E^i denotes the incident field from the feed, E^r denotes the reflected field from the parabolic surface and E^d denotes the diffracted field from the edge of the parabolic reflector. It is clear that the diffracted fields are significant (especially in the region $\theta<\alpha$), and therefore, have to be considered for finding the total far–field radiation pattern. Table I also includes the techniques which are generally used to calculate the far–field patterns in the individual regions.

Table I Total Field in Different Angle Regions and Techniques for Calculating the Far–field Radiation Pattern

Regions	Angle	Field	Techniques
rear–axial region	$\theta\approx 0$	E^d	EEC
shadow region	$\theta\lesssim\alpha$	E^d	GTD or APO
illuminated region	$\alpha<\theta<\pi$	E^i+E^d	GTD or APO
forward–axial region	$\theta\approx\pi$	$E^i+E^r+E^d$	PO

In the shadow and illuminated regions, the patterns are calculated by means of GTD and APO. In the vicinity of the caustic directions $\theta = \pi$ and $\theta = 0$, where the asymptotic methods fail, PO and EEC are used, respectively.

4. GTD Analysis of the Radiation from Paraboloidal Structures

4.1 Introduction

The GTD ([5],[12],[13]) describes the diffraction phenomena by introducing various kinds of diffracted rays, such as single–diffracted rays and multiple–diffracted rays. The corresponding diffracted waves are assumed to follow the laws of diffraction and to diverge according to GO laws. Consequently, the points of diffraction and the paths of the rays can be found from the laws of diffraction, and the amplitude of the fields along the rays can be found from the principle of energy conservation. So, this theory not only provides a qualitative description of diffraction in terms of the diffracted rays, but also permits a quantitative determination of the diffracted field as well. In this report, only single–diffracted rays are considered; the small contributions of multiple–diffracted rays being neglected.

The initial value of the diffracted field at the point of diffraction is obtained by multiplying the field vector of the incident wave by the dyadic diffraction coefficient, which was first obtained by Keller by comparing his diffraction expressions with Sommerfeld's exact solutions for various canonical problems. Although the diffraction coefficients are derived for canonical problems, such as the diffraction of a plane, cylindrical, conical or spherical wave at a perfectly conducting infinite half plane or wedge, the theory can also be used to calculate the field diffracted from other objects as long as their dimensions are large compared to the wavelength. In that case only the immediate neighbourhood of the points of diffraction effectively contributes so that the diffraction can be considered as a local phenomenon.

According to Keller's GTD ([12],[13]),the contributions to the field in an observation point $P(r,\theta,\phi)$ come, in the case of the symmetrical reflector antenna (Fig. 4–1), mainly from two points Q_i (i=1,2), which are the intersection points of the plane containing the lines O'P and O'F with the edge of the reflector (see Fig. 4–1).

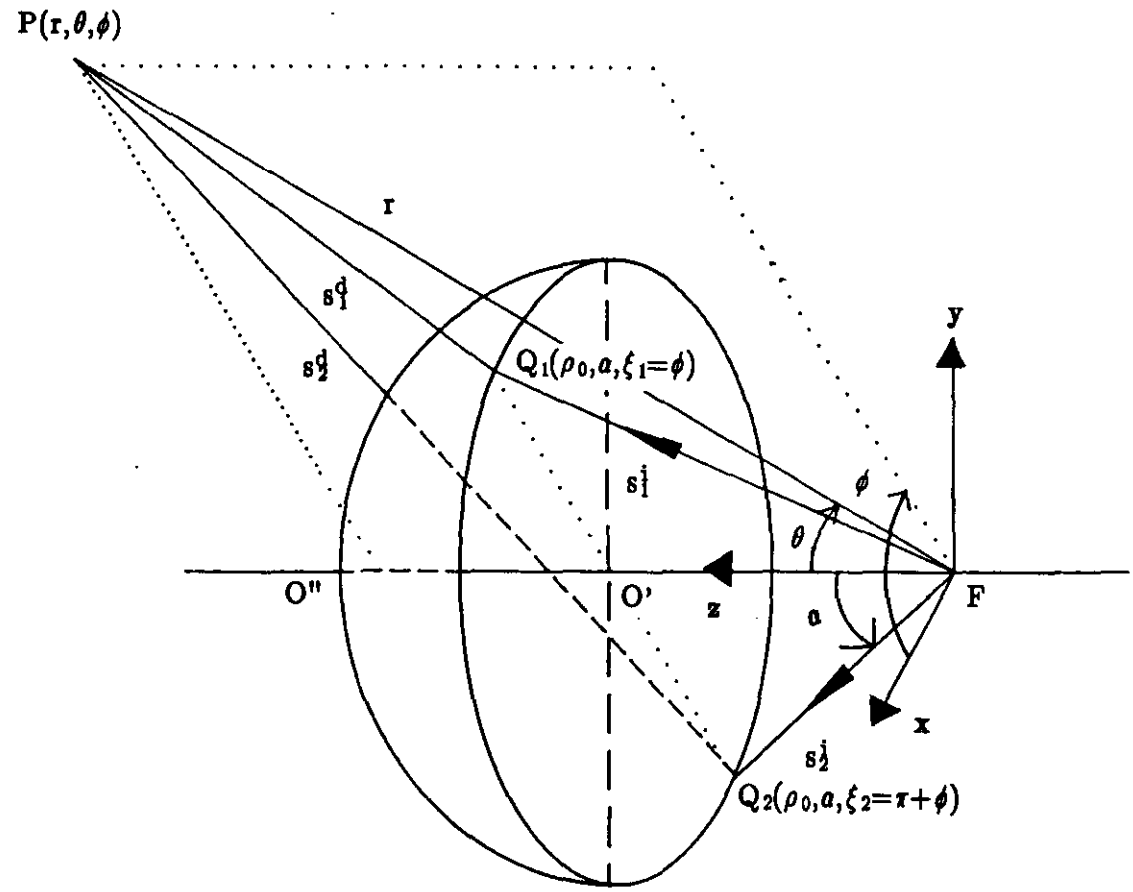

Fig. 4–1 Geometry of Diffracted Rays

The coordinates of these points are thus given by:

$$\xi_1 = \phi \qquad (4\text{–}1,a)$$

$$\xi_2 = \phi + \pi \qquad (4\text{–}1,b)$$

The diffracted field $E^d(P)$ due to the diffraction point Q_i can be expressed by [6]:

$$\vec{E}^d(P) = \overline{D} \cdot \vec{E}^i(Q_i)\, A(s_i^i, s_i^d)\, e^{-jks_1^d} \qquad (4\text{–}2)$$

where $\overline{D}$ is the dyadic diffraction coefficient, $A(s_i^i, s_i^d)$ is the caustic divergence factor, s_i^i is the distance from the feed to the point of diffraction, s_1^d is the distance

from the point of diffraction to the observation point, and $\vec{E}^i(Q_i)$ is the incident field at point Q_i.

Because Q_1, Q_2, P, F and O' are lying in the same ϕ–plane, we can consider the case as a two dimensional problem and only take a single ϕ–plane to analyze the diffracted fields as shown in Fig.4–2.

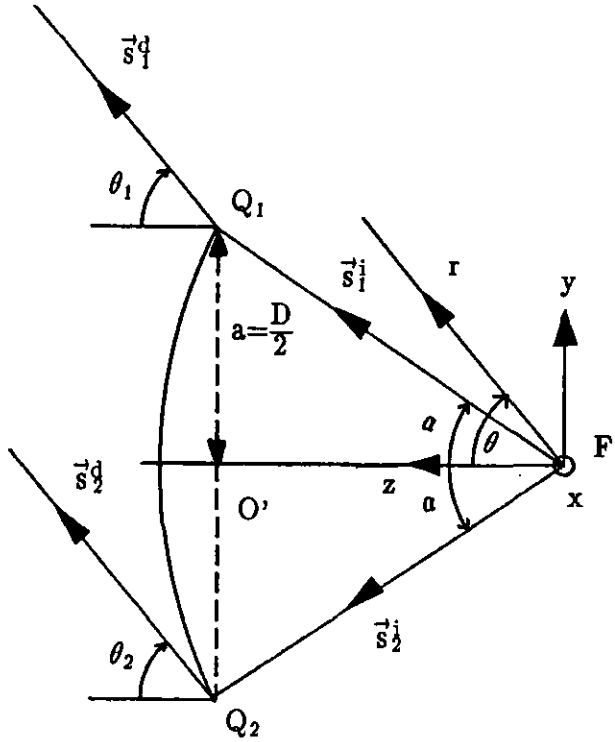

Fig. 4–2 Two Dimensional Geometry to Analyze the Diffracted Field

To be able to calculate the diffracted field, the following procedure is followed; first the caustic divergence factor is determined followed by a derivation of the dyadic diffraction coefficients.

4.2 Calculation of the Caustic Divergence Factor

For diffraction of an incident spherical wave at a curved edge, the caustic divergence factor takes the following form [6]:

$$A(\rho_c, s_1^d) = \sqrt{\frac{\rho_c}{s_1^d(\rho_c + s_1^d)}} \qquad (4\text{–}3)$$

where

$$\frac{1}{\rho_c} = \frac{1}{\rho_e{}^i} - \frac{\vec{n}\cdot(\vec{s}_1^{\,i} - \vec{s}_1^{\,d})}{\rho_g \sin^2\beta_0} \qquad (4\text{–}4)$$

with ρ_c the distance between the caustic at the edge and the second caustic of the diffracted ray,

ρ_g the radius of curvature of the edge at the diffraction point,

$\vec{n}$ the unit vector normal to the edge at Q_i and directed away from the center of the curvature,

$\rho_e{}^i$ the radius of the curvature of the incident wavefront at the edge –fixed plane of incidence which contains the unit vectors $\vec{s}_1^{\,i}$ and the unit vector $\vec{T}$ tangent to the edge at Q_i,

$\vec{s}_1^{\,i}$ the unit vector in the direction of the incident ray,

$\vec{s}_1^{\,d}$ the unit vector in the direction of the diffracted ray,

β_0 the angle between $\vec{s}_1^{\,i}$ and the tangent $\vec{T}$ to the edge at the point of diffraction,

Eq.(4–3) is the general formula for the caustic divergence factor. In the following sections, Eq.(4–3) will be worked out for our specific geometry.

4.2.1 $A_1(\rho_{c1}, s_1{}^d)$ for the Upper Point Q_1

Fig. 4–3 shows the upper point Q_1 and associated vectors in detail. It is easy to find:

$$\vec{n}\cdot\vec{s}_1{}^i = \sin\alpha \qquad (4\text{–}5,a)$$

$$\vec{n}\cdot\vec{s}_1{}^d = \sin\theta_1 \qquad (4\text{–}5,b)$$

$$\rho_e{}^i = \rho_0 \qquad (4\text{–}5,c)$$

$$\rho_g = a \qquad (4\text{–}5,d)$$

$$\beta_0 = \frac{\pi}{2} \qquad (4\text{–}5,e)$$

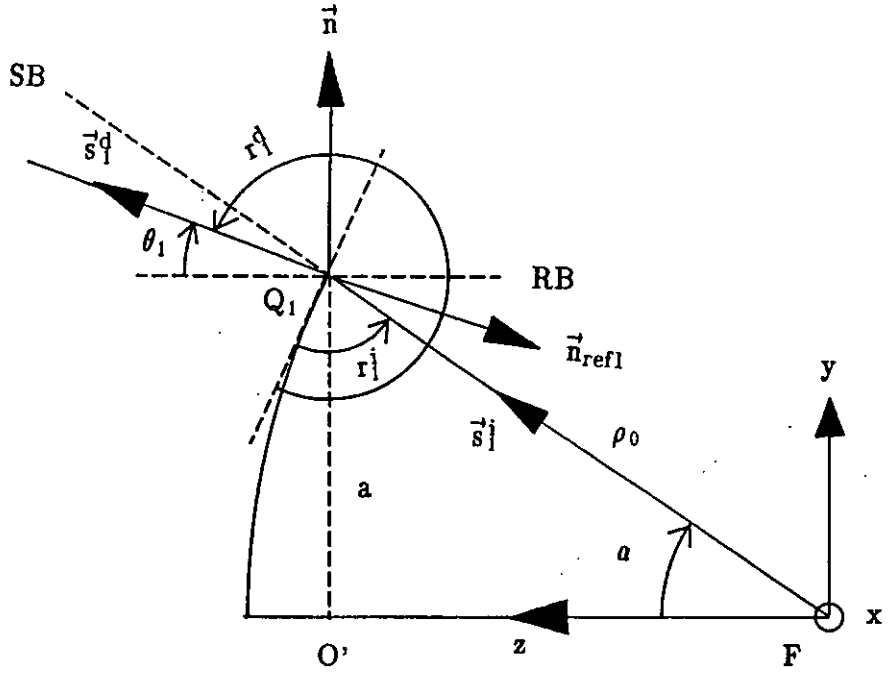

Fig. 4–3 Geometry of Incident and Diffracted Rays at Q_1

Inserting Eq. (4–5) in Eq. (4–4), then in Eq. (4–3) results in:

$$\rho_{c1} = \rho_0 \frac{\sin\alpha}{\sin\theta_i}, \tag{4–6}$$

$$A_1(\rho_{c1}, s_1^d) = \frac{1}{s_1^d}\sqrt{\frac{\rho_0 \sin\alpha}{\sin\theta_1}} \qquad (s_1^d \gg \rho_{c1}) \tag{4–7}$$

4.2.2 $A_2(\rho_{c2}, s_2^d)$ for the Lower Point Q_2

Fig. 4–4 shows the lower point Q_2 and associated vectors in detail. For this diffraction point, it follows that:

$$\vec{n}\cdot\vec{s}_2^{\,i} = \sin\alpha, \tag{4–8,a}$$

$$\vec{n}\cdot\vec{s}_2^{\,d} = -\sin\theta_2 \tag{4–8,b}$$

$$\rho_{e^i} = \rho_0 \qquad (4\text{–}8,c)$$

$$\rho_g = a \qquad (4\text{–}8,d)$$

$$\beta_0 = \frac{\pi}{2} \qquad (4\text{–}8,e)$$

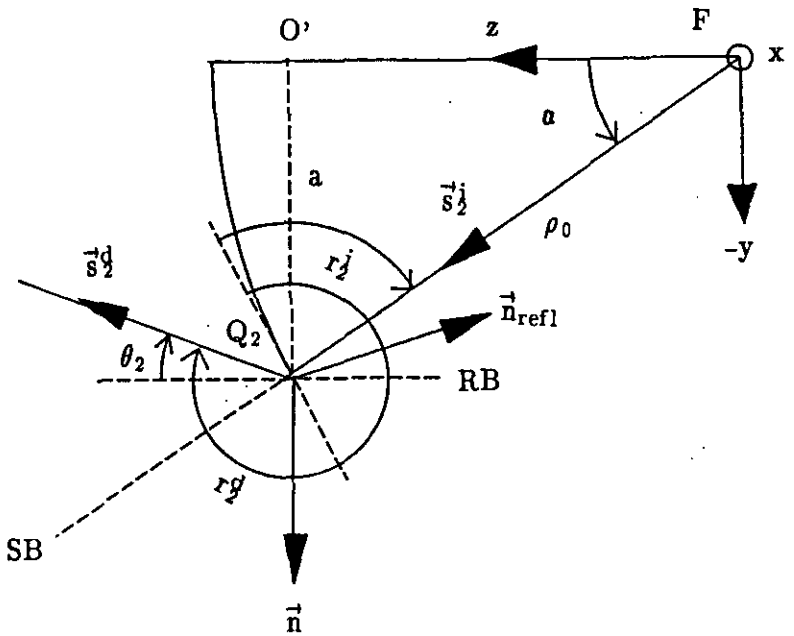

Fig. 4–4 Geometry of Incident and Diffracted Rays at Q_2

Inserting Eq. (4–8) in Eq. (4–4), then inserting into Eq. (4–3) results in:

$$\rho_{c2} = -\rho_0 \frac{\sin\alpha}{\sin\theta_2}, \qquad (4\text{–}9)$$

$$A_2(\rho_{c2}, s_2^d) = \frac{1}{s_2^d}\sqrt{\frac{\rho_0 \sin\alpha}{\sin\theta_2}}\, e^{j(\pi/2)} \qquad (s_2^d \gg \rho_{c2}) \qquad (4\text{–}10)$$

4.3 Calculation of the Diffraction Coefficients

According to Kouyoumjian and Pathak [6], the dyadic diffraction coefficient can be written as:

$$\bar{D} = -\vec{\beta}_0^{\,i}\vec{\beta}_0^{\,d} D_s - \vec{\phi}_0^{\,i}\vec{\phi}_0^{\,d} D_h \qquad (4\text{–}11)$$

with (see Fig. 4–5):

$\vec{\phi}_0^{\,i}$ the unit vector perpendicular to the incident plane, which contains the unit vector $\vec{s}^{\,i}$ and the unit vector $\vec{T}$,

$\vec{\phi}_0^{\,d}$ the unit vector perpendicular to the diffraction plane, which contains the unit vector $\vec{s}^{\,d}$ and the unit vector $\vec{T}$,

$\vec{\beta}_0^{\,i}$ the unit vector parallel to the incident plane and related to $\vec{s}^{\,i}$ and $\vec{\phi}_0^{\,i}$ by $\vec{\beta}_0^{\,i} = \vec{s}^{\,i} \times \vec{\phi}_0^{\,i}$,

$\vec{\beta}_0^{\,d}$ the unit vector parallel to the diffraction plane and related to $\vec{s}^{\,d}$ and $\vec{\phi}_0^{\,d}$ by $\vec{\beta}_0^{\,d} = \vec{s}^{\,d} \times \vec{\phi}_0^{\,d}$,

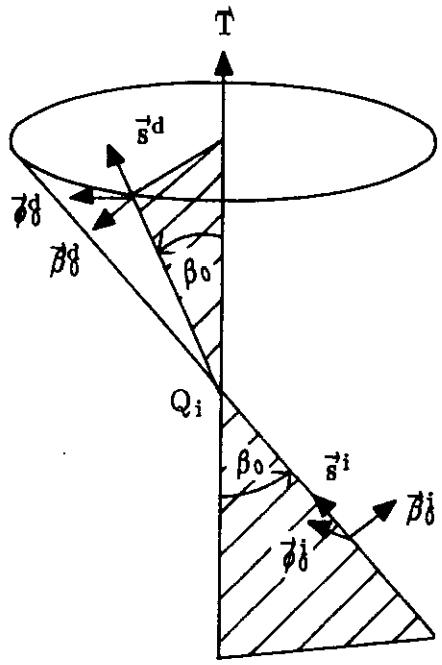

Fig. 4–5 Diffraction at an Edge

and it is shown in [6] that $\overline{D}_{s}^{s}$ can generally be written in the following form:

$$D_{\substack{s\\h}}=\frac{-e^{-j(\pi/4)}}{2\sqrt{2\pi k}\sin\beta_0}\left\{\frac{F[kL^{i}a(r^{d}-r^{i})]}{\cos(\frac{r^{d}-r^{i}}{2})}\mp\frac{F[kL^{r}a(r^{d}+r^{i})]}{\cos(\frac{r^{d}+r^{i}}{2})}\right\} \qquad (4\text{–}12)$$

with D_s the scalar diffraction coefficient for the soft boundary condition,

D_h the scalar diffraction coefficient for the hard boundary condition,

r^i the angle between the incident ray and the paraboloidal surface tangent, which is perpendicular to the plane of incidence,

r^d the angle between the diffraction ray and the paraboloidal surface tangent, which is perpendicular to the plane of diffraction,

$$a(r^{d}\mp r^{i}) = 2\cos^{2}(\frac{r^{d}\mp r^{i}}{2}) \qquad (4\text{–}13)$$

$F(z)= 2j\sqrt{z}\exp(jz)\int_{\sqrt{z}}^{\infty}\exp(-j\tau^{2})\,d\tau$ involving a Fresnel integral,

L^i, L^r denote the distance parameters defined as:

$$L^{i}=\frac{s^{d}(\rho_{e}^{i}+s^{d})\rho_{1}^{i}\rho_{2}^{i}\sin^{2}\beta_0}{\rho_{e}^{i}(\rho_{1}^{i}+s^{d})(\rho_{2}^{i}+s^{d})} \qquad (4\text{–}14,a)$$

$$L^{r}=\frac{s^{d}(\rho_{e}^{r}+s^{d})\rho_{1}^{r}\rho_{2}^{r}\sin^{2}\beta_0}{\rho_{e}^{r}(\rho_{1}^{r}+s^{d})(\rho_{2}^{r}+s^{d})} \qquad (4\text{–}14,b)$$

and

$\rho_1^{i,2}$ the principal radii of curvature of the incident wavefront at $Q_{1,2}$,

$\rho_1^{r,2}$ the principal radii of curvature of the reflected wavefront at $Q_{1,2}$,

$\rho_e{}^r$ given by:

$$\frac{1}{\rho_e{}^r} = \frac{1}{\rho_e{}^i} - \frac{2(\vec{n}_{refl}\cdot\vec{n})\cdot(\vec{s}^i\cdot\vec{n}_{refl})}{\rho_g \sin^2\beta_0} \tag{4–15}$$

with $\vec{n}_{refl}$ as the normal unit vector to the paraboloidal surface at Q_i.

Now, the general formulae for the dyadic diffraction coefficients have been presented. In the following sections the coefficients for the reflector geometry under consideration will be derived.

4.3.1 Diffraction Coefficients for the Upper Point Q_1

For the upper diffraction point Q_1, Fig. 4–3 shows that:

$$r_1^i = \frac{\pi-\alpha}{2} \tag{4–16,a}$$

$$r_1^d = \frac{\alpha+3\pi}{2} - \theta_1 \tag{4–16,b}$$

$$\cos\left(\frac{r_1{}^d - r_1{}^i}{2}\right) = -\sin\left(\frac{\alpha-\theta_1}{2}\right) \tag{4–16,c}$$

$$\cos\left(\frac{r_1{}^d + r_1{}^i}{2}\right) = -\cos\left(\frac{\theta_1}{2}\right) \tag{4–16,d}$$

Further, it is easy to see that L^i, L^r, $\cos\left(\frac{r_1{}^d - r_1{}^i}{2}\right)$ and $\cos\left(\frac{r_1{}^d + r_1{}^i}{2}\right)$ can be replaced by ρ_0, ∞, $-\sin\left(\frac{\alpha-\theta_1}{2}\right)$ and $\cos\left(\frac{\theta_1}{2}\right)$, respectively, due to the focusing properties of the rotational symmetric parabolic reflector surface. This means that the arguments of the two functions F(z) in Eq.(4–12) can be written as:

$$kL^i a(r^d - r^i) = 2k\rho_0 \sin^2\left(\frac{\alpha-\theta_1}{2}\right) \tag{4–17}$$

$$kL^r a(r^d + r^i) = 2kL^r \cos^2\left(\frac{\theta_1}{2}\right) \longrightarrow \infty \quad (\text{when } \theta_1 \neq \pi) \tag{4–18}$$

So, Eq.(4–12) for the scalar diffraction coefficients becomes:

$$D_{\substack{s\\h}} = \frac{e^{-j(\pi/4)}}{2\sqrt{2\pi k}} \left\{ \frac{F[2k\rho_0 \sin^2(\frac{a-\theta_1}{2})]}{\sin(\frac{a-\theta_1}{2})} \mp \frac{F[2kL^r \cos^2\frac{\theta_1}{2}]}{\cos(\frac{\theta_1}{2})} \right\} \qquad (4\text{–}19)$$

The function F(z) will approach one if $z \longrightarrow \infty$ (see Fig. 4–6). Since in the case $\theta \neq \pi$ (away from the axial direction), $z=2kL^r\cos^2(\frac{\theta_1}{2})$ approaches infinity, the function F(z) can be approximated by one.

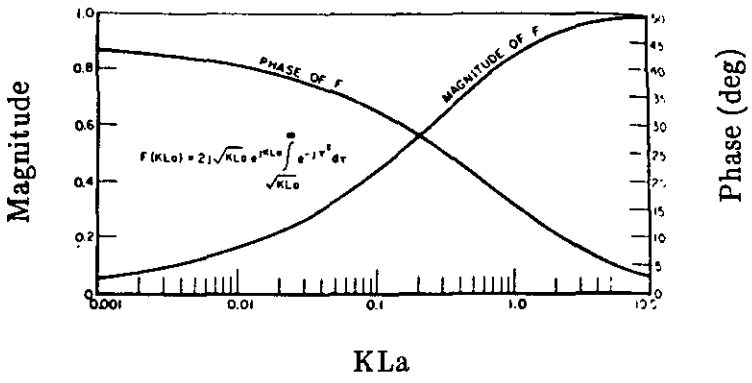

KLa

Fig. 4–6 Modified Fresnel Transition Function [6]

Then Eq. (4–19) becomes:

$$D_{\substack{s\\h}} = \frac{e^{-j(\pi/4)}}{2\sqrt{2\pi k}} \left\{ \frac{F[2k\rho_0 \sin^2(\frac{a-\theta_1}{2})]}{\sin(\frac{a-\theta_1}{2})} \mp \frac{1}{\cos(\frac{\theta_1}{2})} \right\} \qquad (4\text{–}20)$$

Now, the scalar diffraction coefficients have been obtained. But, the vector property of the fields still have to be considered. This can be done by expressing the incident and diffracted fields in terms of two components according to the two orthogonal directions defined in Fig. 4–5:

$$\vec{E}^i = E_{\beta_0}^i \cdot \vec{\beta}_0^i + E_{\phi_0}^i \cdot \vec{\phi}_0^i \qquad (4\text{–}21,a)$$

$$\vec{E}^d = E_{\beta_0}^d \cdot \vec{\beta}_0^d + E_{\phi_0}^d \cdot \vec{\phi}_0^d \qquad (4\text{–}21,b)$$

Inserting Eq. (4–21) in Eq. (4–2), and then comparing it with Eq. (4–11) shows that the relation between the incident fields and the diffracted fields can be written in the form [6]:

$$\begin{bmatrix} E_{\beta_0}^{d} \\ E_{\phi_0}^{d} \end{bmatrix} = \begin{bmatrix} -D_s & 0 \\ 0 & -D_h \end{bmatrix} \begin{bmatrix} E_{\beta_0}^{i} \\ E_{\phi_0}^{i} \end{bmatrix} \sqrt{\frac{\rho_c}{s_i^d(\rho_c + s_i^d)}} \exp(-jks_i^d) \qquad (4\text{–}22)$$

For the symmetrical antenna configuration considered in this part of the report, the incident radiation from the feed is normal to the edge of the paraboloid. So, β_0 equals $\pi/2$ and the directions of the different vectors can be shown as in Fig. 4–7, where the incident fields are projected on the plane containing $\vec{s}^i$ and $\vec{T}$, and the diffracted field from diffraction point Q_i is projected on the plane containing $\vec{s}^d$ and $\vec{T}$. Since these two planes generally do not coincide, the projection of all vectors onto the plane through the diffraction point (Q_i) and perpendicular to the tangent ($\vec{T}$) of the edge at Q_i are drawn in Fig. 4–8. The figure, which will be used later on to determine the relations between the incident and diffracted field vector components, shows the relation between the two planes as given in Fig. 4–7.

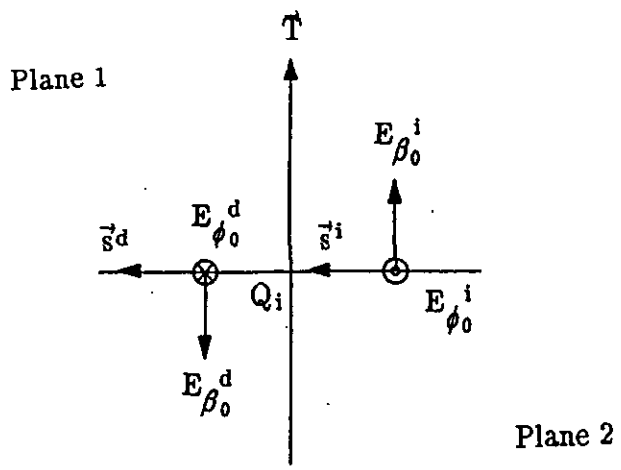

Fig. 4–7 Diffraction at Edge (two dimensional in plane parallel to $\vec{T}$ at Q_i)

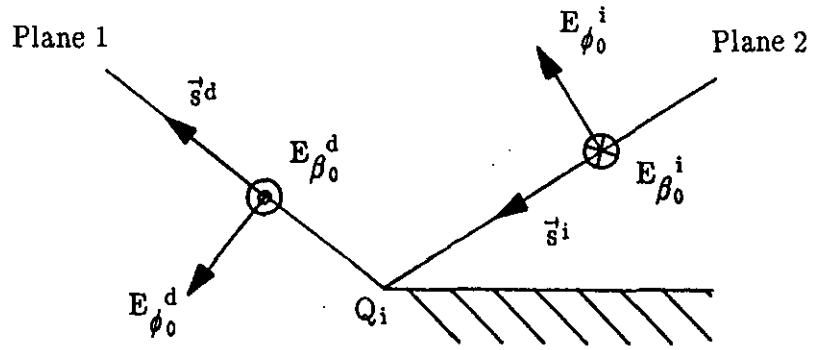

Fig. 4–8 Diffraction at Edge (in the plane perpendicular to $\vec{T}$ at Q_i)

Considering the diffraction point on the edge of the paraboloidal reflector the following relations are found for the vector components of the incident and diffracted fields at the diffraction point Q_1 (see Fig. 4–9):

$$E^d_{\phi_1} = -E^d_{\beta_{01}} \tag{4–23,a}$$

$$E^d_{\theta_1} = -E^d_{\phi_{01}} \tag{4–23,b}$$

$$E^i_{\beta_{01}} = E^i_{f\phi_1} \tag{4–24,a}$$

$$E^i_{\phi_{01}} = E^i_{f\theta_1} \tag{4–24,b}$$

$$\begin{bmatrix} E^d_{\phi_1} \\ E^d_{\theta_1} \end{bmatrix} = -\begin{bmatrix} E^d_{\beta_{01}} \\ E^d_{\phi_{01}} \end{bmatrix} = -\begin{bmatrix} -D_s & 0 \\ 0 & -D_h \end{bmatrix} \begin{bmatrix} E^i_{\beta_{01}} \\ E^i_{\phi_{01}} \end{bmatrix} \sqrt{\frac{\rho_{c1}}{s_1^d(\rho_{c1}+s_1^d)}}\, \exp(-jks_1^d)$$

$$= \begin{bmatrix} D_s & 0 \\ 0 & D_h \end{bmatrix} \begin{bmatrix} E^i_{f\phi_1} \\ E^i_{f\theta_1} \end{bmatrix} \sqrt{\frac{\rho_{c1}}{s_1^d(\rho_{c1}+s_1^d)}}\, \exp(-jks_1^d) \tag{4–25}$$

Writing $\vec{E}_f(\rho_0,\alpha,\xi_1=\phi_1)$ in the form:

$$\begin{bmatrix} E_f{}^i_{\phi_1} \\ E_f{}^i_{\theta_1} \end{bmatrix} = A_0 \frac{e^{-jk\rho_0}}{\rho_0} \sqrt{G_f(\alpha)} \begin{bmatrix} \cos\phi_1 \\ U_\alpha \sin\phi_1 \end{bmatrix} \tag{4–26}$$

and using the far–field approximation:

$$s_1 \cong r \qquad \text{for amplitude} \tag{4–27,a}$$

$$s_1 \cong r - \rho_0 \cos(\alpha - \theta_1) \qquad \text{for phase} \tag{4–27,b}$$

the field in P, diffracted at Q_1, yields:

$$\begin{bmatrix} E_{\phi_1}^d \\ E_{\theta_1}^d \end{bmatrix} = \frac{A_0}{2} \frac{e^{-jkr}}{r} \sqrt{\frac{G_f(\alpha)\sin\alpha}{2\pi k\rho_0 \sin\theta_1}} \left\{ \frac{F[2k\rho_0 \sin^2(\frac{\alpha-\theta_1}{2})]}{\sin(\frac{\alpha-\theta_1}{2})} \mp \frac{1}{\cos(\frac{\theta_1}{2})} \right\}$$

$$\cdot e^{-j[2k\rho_0 \sin^2(\frac{\alpha-\theta_1}{2})+\frac{\pi}{4}]} \begin{bmatrix} \cos\phi_1 \\ U_\alpha \sin\phi_1 \end{bmatrix} \tag{4–28}$$

4.3.2 Diffraction Coefficient for the Lower Point Q_2

Proceeding similarly as in the previous section for Q_2, it is possible to find (see Fig.4–4):

$$r_2{}^i = \frac{\pi-\alpha}{2} \tag{4–29}$$

$$r_2{}^d = \begin{cases} \theta_2 + \dfrac{\alpha+3\pi}{2} & (\theta_2 < \dfrac{\pi-\alpha}{2}) \qquad (4–30,a) \\ \theta_2 + \dfrac{\alpha-\pi}{2} & (\theta_2 > \dfrac{\pi-\alpha}{2}) \qquad (4–30,b) \end{cases}$$

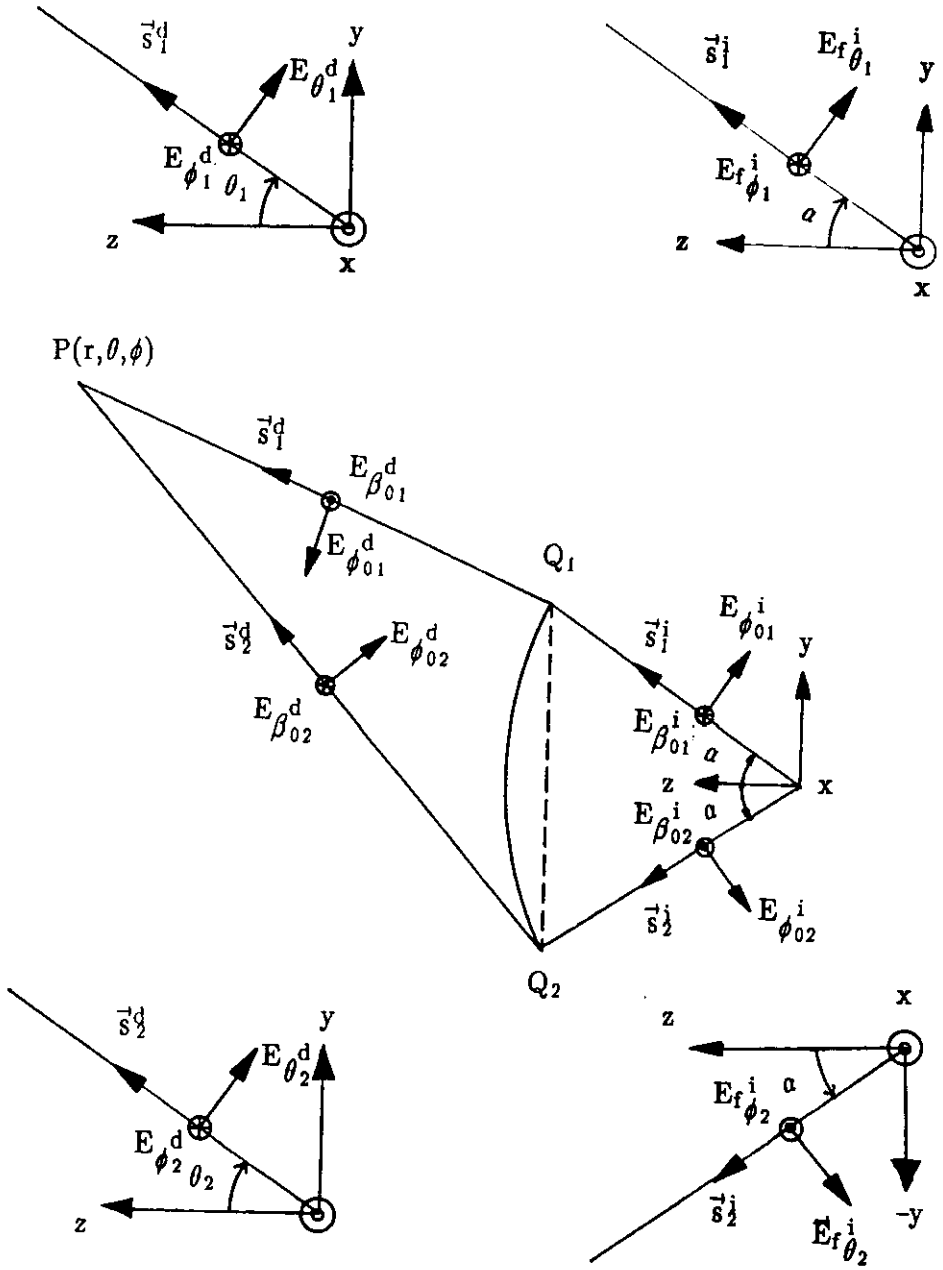

Fig. 4–9 Diffraction at Paraboloid

$$\cos\left(\frac{r_2^d - r_2^i}{2}\right) = -\sin\left(\frac{\alpha+\theta_2}{2}\right) \qquad (4\text{–}31,a)$$

$$\left.\right\} (\theta_2 < \frac{\pi-\alpha}{2})$$

$$\cos\left(\frac{r_2^d + r_2^i}{2}\right) = -\cos\left(\frac{\theta_2}{2}\right) \qquad (4\text{–}31,b)$$

$$\cos\left(\frac{r_2^d - r_2^i}{2}\right) = \sin\left(\frac{\alpha+\theta_2}{2}\right) \qquad (4\text{–}32,a)$$

$$\left.\right\} (\theta_2 > \frac{\pi-\alpha}{2})$$

$$\cos\left(\frac{r_2^d + r_2^i}{2}\right) = \cos\left(\frac{\theta_2}{2}\right) \qquad (4\text{–}32,b)$$

So, the scalar diffraction coefficients for Q_2 are obtained as:

$$D_{s,h} = \epsilon_0 \frac{e^{-j(\pi/4)}}{2\sqrt{2\pi k}} \left\{ \frac{F[2k\rho_0 \sin^2(\frac{\alpha+\theta_2}{2})]}{\sin(\frac{\alpha+\theta_2}{2})} \mp \frac{1}{\cos(\frac{\theta_2}{2})} \right\} \qquad (4\text{–}33)$$

with

$$\epsilon_0 = \begin{cases} 1 & (\theta_2 < \frac{\pi-\alpha}{2}) \\ 0 & (\frac{\pi-\alpha}{2} \le \theta_2 \le \frac{\pi}{2}) \\ -1 & (\theta_2 > \frac{\pi}{2}) \ . \end{cases} \qquad (4\text{–}34)$$

The ϵ_0 is introduced because GTD assumes that $D_{s,h}$ at the diffraction point Q_2 changes its sign when the observation point moves from the region $(\theta_2 < \frac{\pi-\alpha}{2})$ to the region $(\theta_2 > \frac{\pi}{2})$. Furthermore, the single–diffracted ray from edge point Q_2 does not contribute to the scattered field in the region $(\frac{\pi-\alpha}{2} \le \theta_2 \le \frac{\pi}{2})$ because the ray from Q_2 to the observation point P is blocked by the reflector.

From Fig. 4–9 it follows for Q_2 that:

$$E_{\phi_2}^{d}=E_{\beta_{02}}^{d} \tag{4–35,a}$$

$$E_{\theta_2}^{d}=E_{\phi_{02}}^{d} \tag{4–35,b}$$

$$E_{\beta_{02}}^{i}=E_{f\phi_2}^{i} \tag{4–36,a}$$

$$E_{\phi_{02}}^{i}=E_{f\theta_2}^{i} \tag{4–36,b}$$

$$\begin{bmatrix} E_{\phi_2}^{d} \\ E_{\theta_2}^{d} \end{bmatrix} = \begin{bmatrix} E_{\beta_{02}}^{d} \\ E_{\phi_{02}}^{d} \end{bmatrix} = \begin{bmatrix} -D_s & 0 \\ 0 & -D_h \end{bmatrix} \begin{bmatrix} E_{\beta_{02}}^{i} \\ E_{\phi_{02}}^{i} \end{bmatrix} \sqrt{\frac{\rho_{c\,2}}{s_2^{d}(\rho_{c2}+s_2^{d})}}\exp(-jks_2^{d})$$

$$= \begin{bmatrix} -D_s & 0 \\ 0 & -D_h \end{bmatrix} \begin{bmatrix} E_{f\phi_2}^{i} \\ E_{f\theta_2}^{i} \end{bmatrix} \sqrt{\frac{\rho_{c\,2}}{s_2^{d}(\rho_{c2}+s_2^{d})}}\exp(-jks_2^{d}) \tag{4–37}$$

Writing $\vec{E}_f(\rho_0,a,\xi_2=\phi_2+\pi)$ at Q_2 in the form:

$$\begin{bmatrix} E_{f\phi_2}^{i} \\ E_{f\theta_2}^{i} \end{bmatrix} = A_0\frac{e^{-jk\rho_0}}{\rho_0}\sqrt{G_f(a)} \begin{bmatrix} \cos(\phi_2+\pi) \\ U_a\sin(\phi_2+\pi) \end{bmatrix}$$

$$= A_0\frac{e^{-jk\rho_0}}{\rho_0}\sqrt{G_f(a)} \begin{bmatrix} -\cos\phi_2 \\ -U_a\sin\phi_2 \end{bmatrix} \tag{4–38}$$

and using the far–field approximation:

$$s_2 \cong r \qquad \text{for amplitude} \tag{4–39,a}$$

$$s_2 \cong r-\rho_0\cos(a+\theta_2) \qquad \text{for phase} \tag{4–39,b}$$

the field in P, diffracted at Q_2, yields:

$$\begin{bmatrix} E_{\phi_2}^{d} \\ E_{\theta_2}^{d} \end{bmatrix} = \epsilon_0 \frac{A_0}{2} \frac{e^{-jkr}}{r} \sqrt{\frac{G_f(a)\sin a}{2\pi k\rho_0 \sin\theta_2}} \left\{ \frac{F[2k\rho_0 \sin^2(\frac{a+\theta_2}{2})]}{\sin(\frac{a+\theta_2}{2})} \mp \frac{1}{\cos(\frac{\theta_2}{2})} \right\}$$

$$\cdot e^{-j[2k\rho_0 \sin^2(\frac{a+\theta_2}{2}) - \frac{\pi}{4}]} \begin{bmatrix} \cos\phi_2 \\ U_a \sin\phi_2 \end{bmatrix} \qquad (4\text{–}40)$$

4.4 The Total Field

The total field is the sum of the fields originating from the diffraction points Q_1, Q_2 and the direct field from the feed.

Because the observation point $P(r,\theta,\phi)$ is a far–field point and P, Q_i and F are lying in one ϕ–plane, it is possible to write:

$$\theta_1 \cong \theta_2 \cong \theta, \qquad (4\text{–}41,a)$$

$$\phi_1 = \phi_2 = \phi, \qquad (4\text{–}41,b)$$

Then, the total field can be written as:

$$\begin{bmatrix} E_{\phi}^{d} \\ E_{\theta}^{d} \end{bmatrix} = \begin{bmatrix} E_{\phi_1}^{d} \\ E_{\theta_1}^{d} \end{bmatrix} + \begin{bmatrix} E_{\phi_2}^{d} \\ E_{\theta_2}^{d} \end{bmatrix} + \begin{bmatrix} E_{f\phi}^{i} \\ E_{f\theta}^{i} \end{bmatrix}$$

$$= A_0 \frac{e^{-jkr}}{r} \left\{ \frac{1}{2} \sqrt{\frac{G_f(a)\sin a}{2\pi k\rho_0 \sin\theta}} \left[\left\{ \frac{F[2k\rho_0 \sin^2(\frac{a-\theta}{2})]}{\sin(\frac{a-\theta}{2})} \mp \frac{1}{\cos(\frac{\theta}{2})} \right\} \cdot e^{-j[2k\rho_0 \sin^2(\frac{a-\theta}{2}) + \frac{\pi}{4}]} \right.\right.$$

$$\left. + \epsilon_0 \left\{ \frac{F[2k\rho_0 \sin^2(\frac{a+\theta}{2})]}{\sin(\frac{a+\theta}{2})} \mp \frac{1}{\cos(\frac{\theta}{2})} \right\} \cdot e^{-j[2k\rho_0 \sin^2(\frac{a+\theta}{2}) - \frac{\pi}{4}]} \right] \begin{bmatrix} \cos\phi \\ U_a \sin\phi \end{bmatrix}$$

$$\left. + \sqrt{G_f(\theta)} \begin{bmatrix} \cos\phi \\ U_\theta \sin\phi \end{bmatrix} U[(\theta - a)] \right\} \qquad (4\text{–}42)$$

Eq. (4–42) gives the complete field radiation in all the regions excluding the directions of θ=0, π and their vicinities. Radiation patterns calculated using the above formula are shown in Figs.4–10(a) and 4–10(b) for the E–plane and the H–plane, respectively. The aperture diameter of the reflector is 1.5 meters, the half subtended angle a is 60^0 degrees and the operating frequency of the antenna is 3 GHz. The observation angles θ=180–θ in the following figures are measured from boresight as commonly done in literature.

It can be seen from Fig. 4–10(a) that there are discontinuities at $\theta=\frac{\pi}{2}$ and $\theta=\frac{\pi-a}{2}$. These discontinuities are caused by the ϵ_0, defined by Eq.(4–34) and used in Eq.(4–42), which accounts for the blocking effect that the reflector has on the lower diffraction point Q_2. Since the single edge–diffracted field is blocked by the reflector, the surface diffracted field from the back surface of the reflector gives an important contribution to the far–field in this region. Therefore, the surface diffracted field has to be calculated in that region to obtain the continuous radiation patterns.

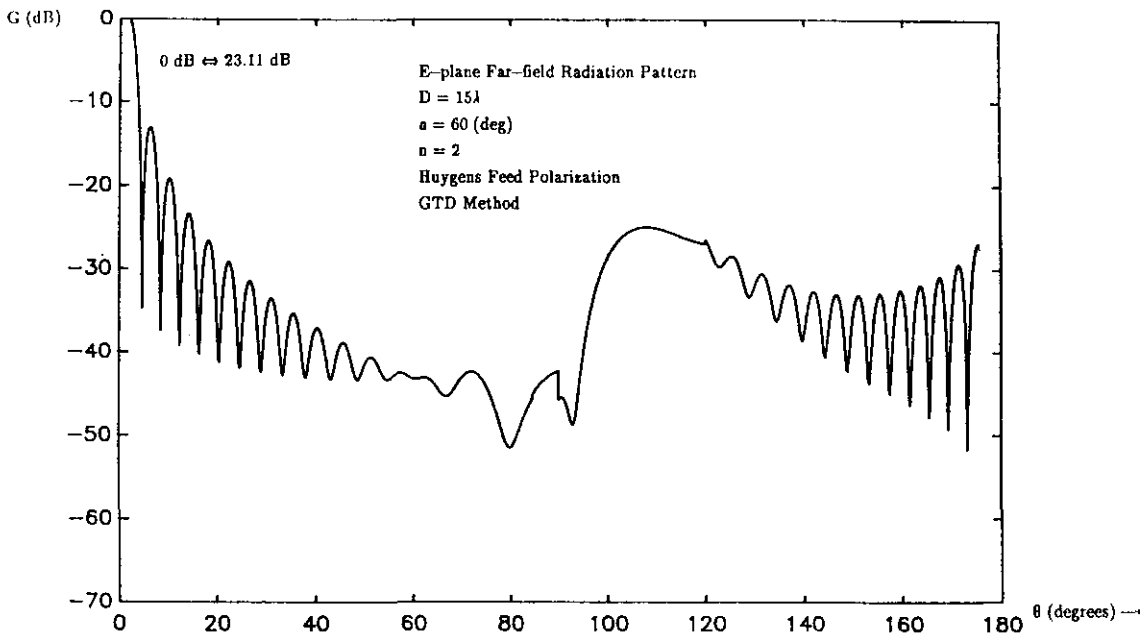

Fig. 4–10(a) E–plane Far–field Radiation Pattern of a Focus–fed Axially Symmetrical Paraboloid

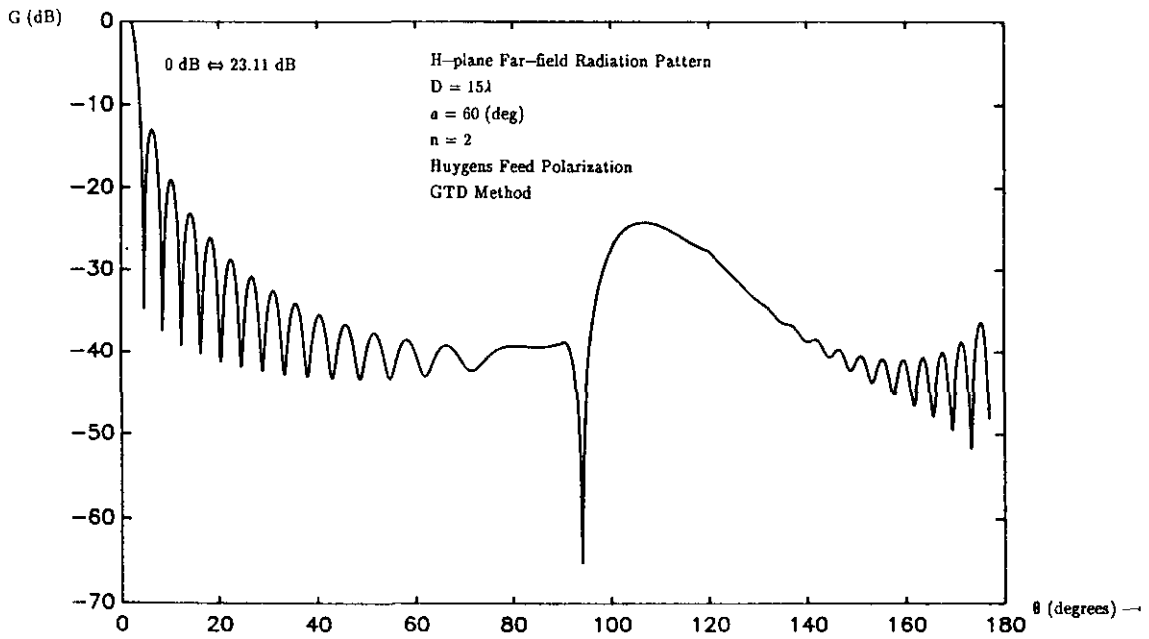

Fig. 4–10(b) H–plane Far–field Radiation Pattern of a Focus–fed Axially Symmetrical Paraboloid

4.5 Modification of GTD

To calculate the contributions from the surface diffracted field, we can replace the edge diffraction coefficient for Q_2 by the surface diffraction coefficients in the blocked angle region (see Fig. 4–11). It is stated in [12] that the field diffracted around a curved surface decreases exponentially with λ, and is weaker than the field diffracted by an edge where the diffraction coefficient is proportional to $\sqrt{\lambda}$.

Instead of using the GTD edge diffraction coefficient, the GTD diffraction coefficients are used, multiplied with R_{se} [25]:

$$R_{se}=(\sqrt{\lambda}-(\sqrt{\lambda}-(e^{\lambda}-1))\sin((\theta-\frac{\pi-\alpha}{2})/(\frac{\alpha}{2\pi})))/\sqrt{\lambda} \qquad (4\text{–}43)$$

to obtain the surface diffracted field. As indicated in [12] the R_{se} shows that the surface diffracted field is weaker than the edge diffracted field, because:

$$\lim_{\lambda\to 0}\frac{e^{\lambda}-1}{\sqrt{\lambda}}=0$$

The sin function is employed analogous to the correction factor in APO (Knop and Ostertag [8]). Furthermore, $\sin((\theta-\frac{\pi-\alpha}{2})/(\frac{\alpha}{2\pi}))$ is continuous even at the angles $\theta=\frac{\pi}{2}$ and $\theta=\frac{\pi-\alpha}{2}$. So the R_{se} is choosen equal to 1 outside the blocked region and gradually changes from the edge diffraction coefficient (proportional to $\sqrt{\lambda}$) to the surface diffraction coefficient (proportional to $e^{\lambda}-1$) in the region $\frac{\pi-\alpha}{2}<\theta<\frac{\pi}{2}$.
The E–plane radiation pattern obtained by this modified GTD method is shown in Fig.4–12, for the same antenna configuration as in Fig. 4–10(a).

4.6 Comparison with literature

A comparison of our formulae with those of Safak [17] shows that some of his equations (e.g. the ϵ_0) differ from ours. However, the pattern presented by Safak agree with our pattern as shown in Fig. 4–12.

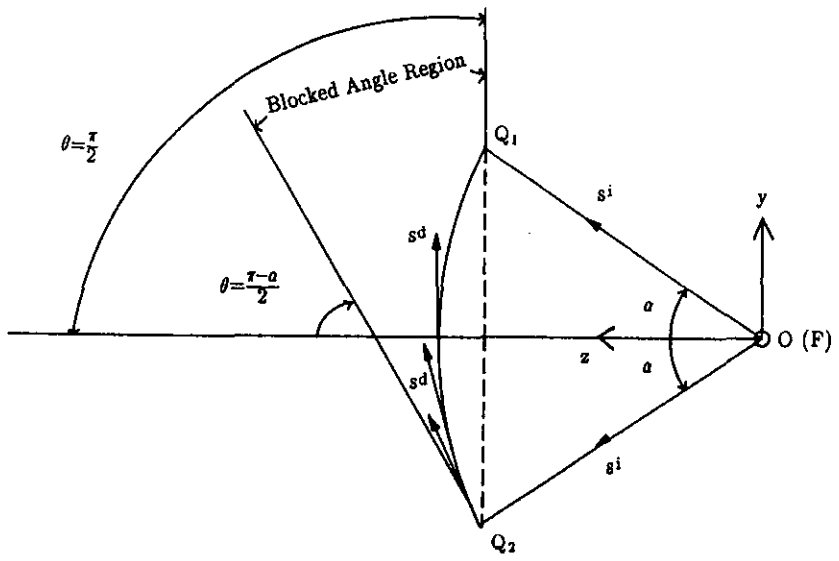

Fig. 4–11 Surface Diffraction Rays

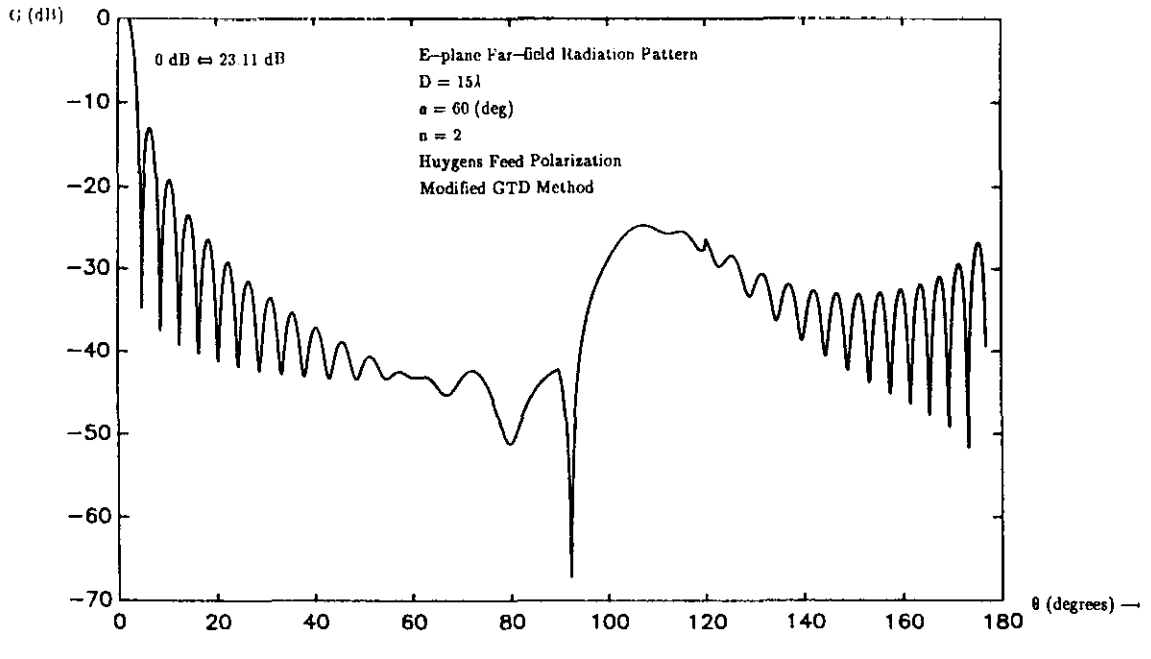

Fig. 4–12 E–plane Far–field Radiation Pattern of a Focus–fed Axially Symmetrical Paraboloid

5. APO Analysis of the Radiation from Paraboloidal Structures

5.1 Introduction

A technique known as Physical Optics (PO), simply approximates the currents at the reflector by the currents calculated from the theory of GO. By evaluating the contributions from all parts of the reflector to the field in an observation point, PO gives the total field. The accuracy of this method is determined by the accuracy of the currents approximated by the theory of GO. The far–field calculation using this method is usually complex and includes time consuming numerical integrals. Only for some special reflector current distributions can closed–form expressions be derived and the integrations carried out analytically. But, if there are stationary points in the integral so that the stationary phase method can be used, the field integrals can be evaluated asymptotically. The method using stationary phase integration to calculate the PO field asymptotically is called Asymptotic Physical Optics (APO).

Rusch ([7],[14]) first used the APO method to calculate the scattered field from paraboloidal reflector antennas and gave the corresponding diffraction coefficients. This method will be used throughout this chapter.

It should be noted that the expressions for the far–field presented in this chapter do not include the direct radiation from the feed.

5.2 Current Calculation by GO

According to geometrical optics, the induced currents on the reflector are:

$$\vec{J}_s = \begin{cases} 2(\vec{n}_{refl} \times \vec{H}_f) & \text{illuminated surface} \quad (5\text{–}1,a) \\ 0 & \text{shadowed surface} \quad (5\text{–}1,b) \end{cases}$$

with

$$\vec{H}_f(\rho,\psi,\xi) = \frac{1}{\eta}[\vec{\rho} \times \vec{E}_f] \qquad (5\text{–}2)$$

Eq. (5–1), shows explicitly that the currents at the back of the reflector are assumed to be zero while they are nonzero at the front of the reflector. So, there has to be a current discontinuity at the edge of the reflector. For the reason of notation economy, Eq. (5–1,b) has been ignored in the following section.

Substitution of Eq.(2–2) into Eq.(5–2) and then into Eq. (5–1,a), yields for an y–polarized feed with Huygens source polarization:

$$\vec{J}_s(\rho,\psi,\xi)= A_0 \frac{2}{\eta}\frac{e^{-jk\rho}}{\rho}\begin{Bmatrix}\sqrt{G(\psi)}\sin(\frac{\psi}{2})\sin\xi\ \vec{\rho}\\ \sqrt{G(\psi)}\cos(\frac{\psi}{2})\sin\xi\ \vec{\psi}\\ \sqrt{G(\psi)}\cos(\frac{\psi}{2})\cos\xi\ \vec{\xi}\end{Bmatrix} \qquad (5–3)$$

Transforming $\vec{J}_s$ from the (ρ,ψ,ξ) coordinate system to the (x,y,z) coordinate system gives:

$$\vec{J}_s(x,y,z)=A_0 \frac{2e^{-jk\rho}}{\eta\rho}[c_x\,\vec{x} + c_y\,\vec{y} + c_z\,\vec{z}] \qquad (5–4)$$

with

$c_x= 0$

$c_y= \sqrt{G(\psi)}\cos(\frac{\psi}{2})$

$c_z= -\sqrt{G(\psi)}\sin(\frac{\psi}{2})\sin\xi.$

5.3 Field Integration by the Stationary Phase Method

The induced current distribution results in a far–field radiation pattern, which is given by the following formula [2]:

$$\vec{E}(r,\theta,\phi)= -j\frac{k\eta}{4\pi r}e^{-jkr}\iint_{S_{refl}}[\vec{J}_s-(\vec{J}_s\cdot\vec{r})\vec{r}]\,e^{jk(\vec{\rho}\cdot\vec{r})}ds \qquad (5–5)$$

For the paraboloid geometry of Fig. 2–1, Eq. (5–5) can be expressed in terms of two components as:

$$\begin{bmatrix} E_\theta \\ E_\phi \end{bmatrix} = -j\frac{k\eta}{4\pi r} e^{-jkr} \iint_{S_{refl}} \begin{bmatrix} \vec{J}_s \cdot \vec{\theta} \\ \vec{J}_s \cdot \vec{\phi} \end{bmatrix} e^{jk(\vec{\rho} \cdot \vec{r})} ds \tag{5–6}$$

where

$$\vec{J}_s \cdot \vec{\theta} = A_0 \frac{2e^{-jk\rho}}{\eta\rho} c_\theta \tag{5–7,a}$$

$$\vec{J}_s \cdot \vec{\phi} = A_0 \frac{2e^{-jk\rho}}{\eta\rho} c_\phi \tag{5–7,b}$$

$$\rho - \vec{\rho} \cdot \vec{r} = \rho(1 - \sin\psi\cos\xi\sin\theta\cos\phi - \sin\psi\sin\xi\sin\theta\sin\phi - \cos\psi\cos\theta) \tag{5–7,c}$$

$$ds = \frac{dxdy}{\cos(\frac{\psi}{2})} \tag{5–7,d}$$

with

$$c_\theta = c_x\cos\theta\cos\phi + c_y\cos\theta\sin\phi - c_z\sin\theta \tag{5–7,e}$$

$$c_\phi = -c_x\sin\phi + c_y\cos\phi. \tag{5–7,f}$$

Taking:

$$G_\theta = -j\frac{k\eta}{4\pi r} e^{-jkr} A_0 \frac{2}{\eta} \frac{c_\theta}{\rho\cos(\frac{\psi}{2})} \tag{5–8,a}$$

$$G_\phi = -j\frac{k\eta}{4\pi r} e^{-jkr} A_0 \frac{2}{\eta} \frac{c_\phi}{\rho\cos(\frac{\psi}{2})} \tag{5–8,b}$$

$$\Phi(x,y) = \rho - \vec{\rho} \cdot \vec{r}, \tag{5–8,c}$$

Eq. (5–6) can be written as:

$$E_{\theta}(r,\theta,\phi)=\iint_{S\,refl} G_{\theta}e^{-jk\Phi(x,y)}dxdy \qquad (5\text{–}9,a)$$

$$E_{\phi}(r,\theta,\phi)=\iint_{S\,refl} G_{\phi}e^{-jk\Phi(x,y)}dxdy. \qquad (5\text{–}9,b)$$

Using Eq.(5–7,c), Eq.(5–8,c) can be writen as:

$$\Phi(x,y)=\frac{1}{2f}\left\{\left[\,x\cos\frac{\theta}{2}-2f\sin\frac{\theta}{2}\cos\phi\,\right]^2+\left[\,y\cos\frac{\theta}{2}-2f\sin\frac{\theta}{2}\sin\phi\,\right]^2\right\} \qquad (5\text{–}10)$$

For the integral form of Eq. (5–9), it has been proven that if the real and imaginary parts of the integrand are fast oscillating while G_{θ} and G_{ϕ} are smoothly varying functions, the major contributions to the integral come from points $(x_{s,i}, y_{s,i})$ where the phase function $\Phi(x_{s,i}, y_{s,i})$ is stationary. The method for calculating the contributions from these stationary points is the stationary phase integration method.

Because both requirements are fulfilled away from the caustic directions ($\theta=0,\pi$), it is possible to use the stationary phase integration method for the integrals of Eq.(5–9). Because the stationary points of the first kind give a crude solution, i.e., the geometric optics solution [14], the stationary points of the second kind are used, satisfying [15]:

$$\frac{\partial\Phi}{\partial x}\frac{\partial\Psi}{\partial y}-\frac{\partial\Phi}{\partial y}\frac{\partial\Psi}{\partial x}=0 \qquad (5\text{–}11)$$

where

$$\Psi(x,y)=x^2+y^2-a^2=0 \qquad (5\text{–}12)$$

is the edge of the reflector.

After inserting Eq. (5–10) and Eq. (5–12) into Eq. (5–11), two stationary points of the second kind are found:

$$\begin{bmatrix} x_{si} \\ y_{si} \end{bmatrix} = a \begin{bmatrix} \cos\xi_i \\ \sin\xi_i \end{bmatrix} \qquad (i=1,2) \qquad (5\text{–}13)$$

where

$$\xi_1 = \phi \qquad (5\text{–}14,a)$$

$$\xi_2 = \phi + \pi. \qquad (5\text{–}14,b)$$

These points coincide with the GTD diffraction points (see the GTD diffraction points of Eq. (4–1)).

In order to be able to calculate the integrals of Eq. (5–9), we must first change the variables in such a way that the origin of the coordinate system is at the stationary point($x_{s,i}$, $y_{s,i}$) and the x'–axis directed to the center of the aperture circle (shown in Fig. 5–1) via :

$$x = x_{si} - \frac{x_{si}}{a} x' + \frac{y_{si}}{a} y' \qquad (5\text{–}15,a)$$

$$y = y_{si} - \frac{y_{si}}{a} x' - \frac{x_{si}}{a} y' \qquad (5\text{–}15,b)$$

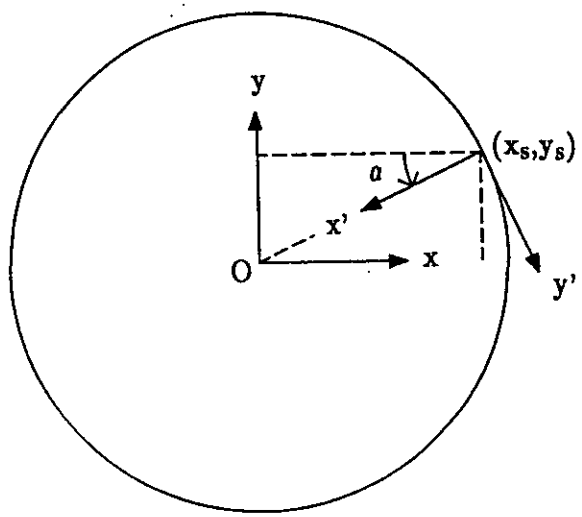

Fig. 5–1 Coordinate System Transformation

A second transformation is used:

$$x' = x'' + \frac{(y'')^2}{2a} \tag{5–16,a}$$

$$y' = y'', \tag{5–16,b}$$

so that:

$$x = x_{si} - \frac{x_{si}}{a} x'' + \frac{y_{si}}{a} y'' - \frac{x_{si}}{2a^2} (y'')^2 \tag{5–17,a}$$

$$y = y_{si} - \frac{y_{si}}{a} x'' - \frac{x_{si}}{a} y'' - \frac{y_{si}}{2a^2} (y'')^2 \tag{5–17,b}$$

Inserting Eq. (5–17) and Eq. (5.13) in Eq. (5–10), gives the following phase function:

$$4f\Phi(x'',y'') = 4f\Phi(x_{si},y_{si}) + x''\left[\pm 4f\sin\theta - 2a(1+\cos\theta)\right] + (y'')^2\left[\pm\frac{2f\sin\theta}{a}\right] \tag{5–18}$$

where

$$4f\Phi(x_{si},y_{si}) = 4f^2(1-\cos\theta) \mp 4af\sin\theta + a^2(1+\cos\theta) \tag{5–19}$$

the minus sign in the formula applies to for the upper stationary point (x_{s1},y_{s1}) and the plus sign to the lower stationary point(x_{s2},y_{s2}).

Equation (5–18) can be written more compactly as:

$$\Phi(x'',y'') = \Phi(x_{si},y_{si}) + (x'')\Phi_{10,i} + (y'')^2\Phi_{02,i} \tag{5–20}$$

where

$$\Phi_{10,i} = \pm \sin\theta - \frac{a}{2f}(1+\cos\theta) \tag{5–21,a}$$

$$\Phi_{02,i} = \pm \frac{\sin\theta}{2a} \tag{5–21,b}$$

and

$$E_{\theta,i}(r,\theta,\phi)\approx G_{\theta}(x_{si},y_{si})e^{-jk\Phi(x_{si},y_{si})}\int_0^{\infty}e^{-jk\Phi_{10,i}x''}dx''\int_{-\infty}^{\infty}e^{-jk\Phi_{02,i}(y'')^2}dy'' \quad (5\text{–}22,a)$$

$$E_{\phi,i}(r,\theta,\phi)\approx G_{\phi}(x_{si},y_{si})e^{-jk\Phi(x_{si},y_{si})}\int_0^{\infty}e^{-jk\Phi_{10,i}x''}dx''\int_{-\infty}^{\infty}e^{-jk\Phi_{02,i}(y'')^2}dy'' \quad (5\text{–}22,b)$$

Evaluating the integrals:

$$\int_{-\infty}^{\infty}e^{-jk\Phi_{02,i}(y'')^2}dy''=\sqrt{\frac{\pi}{k\Phi_{02,i}}}\,e^{-j(\pi/4)} \quad (5\text{–}23,a)$$

$$\int_0^{\infty}e^{-jk\Phi_{10,i}x''}dx''=\frac{1}{jk\Phi_{10,i}} \quad (5\text{–}23,b)$$

then

$$E_{\theta,i}\approx -j\frac{e^{-jk\Phi(x_{si},y_{si})}}{k^{(3/2)}}\cdot\frac{\sqrt{2\pi}\;\;e^{\mp j(\pi/4)}}{[\pm\sin\theta-\frac{a}{2f}(1+\cos\theta)]\sqrt{\frac{\sin\theta}{a}}}\,G_{\theta}(x_{si},y_{si}) \quad (5\text{–}24,a)$$

$$E_{\phi,i}\approx -j\frac{e^{-jk\Phi(x_{si},y_{si})}}{k^{(3/2)}}\cdot\frac{\sqrt{2\pi}\;\;e^{\mp j(\pi/4)}}{[\pm\sin\theta-\frac{a}{2f}(1+\cos\theta)]\sqrt{\frac{\sin\theta}{a}}}\,G_{\phi}(x_{si},y_{si}) \quad (5\text{–}24,b)$$

where

$$\Phi(x_{s1},y_{s1})=\rho_0-(a\sin\theta+z_{sp}\cos\theta) \quad (5\text{–}25,a)$$

$$\Phi(x_{s2},y_{s2})=\rho_0+(a\sin\theta-z_{sp}\cos\theta) \quad (5\text{–}25,b)$$

$$G_{\theta}(x_{si},y_{si}) = -j\frac{k\eta}{4\pi r}e^{-jkr}\,A_0\,\frac{2}{\eta}\,\frac{c_{\theta}}{\rho_0\cos(\frac{a}{2})} \quad (5\text{–}26,a)$$

$$G_{\phi}(x_{si},y_{si}) = -j\frac{k\eta}{4\pi r} e^{-jkr} A_0 \frac{2}{\eta} \frac{c_{\phi}}{\rho_0 \cos(\frac{a}{2})} \qquad (5\text{–}26,b)$$

and

$$c_{\theta} = \sqrt{G_f(a)}\sin\phi(\cos\tfrac{a}{2}\cos\theta \pm \sin\theta\sin\tfrac{a}{2}) \qquad (5\text{–}27,a)$$

$$c_{\phi} = \sqrt{G_f(a)}\cos\phi\cos\tfrac{a}{2} \qquad (5\text{–}27,b)$$

$$z_{sp} = \rho_0\cos a \qquad (5\text{–}27,c)$$

So, inserting of Eq. (5–25), Eq. (5–26) and Eq. (5–27) in Eq. (5–24) gives the far–field radiation patterns from the induced currents at the reflector:

$$E_{\theta,1}(r,\theta,\phi) \approx \left\{ A_0 \frac{\sqrt{G_f(a)}\sin\phi}{\rho_0} e^{-jk\rho_0} \right\} \left\{ e^{-jkr} e^{jk(a\sin\theta + z_{sp}\cos\theta)} \right\} \cdot \left\{ \frac{1}{r}\sqrt{\frac{a}{\sin\theta}} \right\}$$

$$\left\{ -\frac{e^{-j(\pi/4)}}{2\sqrt{2\pi k}} \left[\frac{2(\cos\frac{a}{2}\cos\theta + \sin\theta\sin\frac{a}{2})/\cos\frac{a}{2}}{\sin\theta - (\frac{\sin a}{1+\cos a})(1+\cos\theta)} \right] \right\} \qquad (5\text{–}28,a)$$

$$E_{\phi,1}(r,\theta,\phi) \approx \left\{ A_0 \frac{\sqrt{G_f(a)}\cos\phi}{\rho_0} e^{-jk\rho_0} \right\} \left\{ e^{-jkr} e^{jk(a\sin\theta + z_{sp}\cos\theta)} \right\} \left\{ \frac{1}{r}\sqrt{\frac{a}{\sin\theta}} \right\}$$

$$\left\{ -\frac{e^{-j(\pi/4)}}{2\sqrt{2\pi k}} \left[\frac{2}{\sin\theta - (\frac{\sin a}{1+\cos a})(1+\cos\theta)} \right] \right\} \qquad (5\text{–}28,b)$$

$$E_{\theta,2}(r,\theta,\phi) \approx \left\{ A_0 \frac{\sqrt{G_f(a)}\sin\phi}{\rho_0} e^{-jk\rho_0} \right\} \left\{ e^{-jkr} e^{-jk(a\sin\theta - z_{sp}\cos\theta)} \right\} \left\{ \frac{e^{j(\pi/2)}}{r}\sqrt{\frac{a}{\sin\theta}} \right\}$$

$$\left\{ -\frac{e^{-j(\pi/4)}}{2\sqrt{2\pi k}} \left[\frac{-2(\cos\frac{a}{2}\cos\theta - \sin\theta\sin\frac{a}{2})/\cos\frac{a}{2}}{\sin\theta + (\frac{\sin a}{1+\cos a})(1+\cos\theta)} \right] \right\} \qquad (5\text{–}28,c)$$

$$E_{\phi,2}(r,\theta,\phi)\approx\left\{A_0\sqrt{\frac{G_f(a)\cos\phi}{\rho_0}}e^{-jk\rho_0}\right\}\left\{e^{-jkr}e^{-jk(a\sin\theta-z_{sp}\cos\theta)}\right\}\left\{\frac{e^{j(\pi/2)}}{r}\sqrt{\frac{a}{\sin\theta}}\right\}$$

$$\left\{-\frac{e^{-j(\pi/4)}}{2\sqrt{2\pi k}}\left[\frac{-2}{\sin\theta+(\frac{\sin a}{1+\cos a})(1+\cos\theta)}\right]\right\} \qquad (5\text{–}28,d)$$

These results agree with those given by Rusch [7]. Using Eq.(5–28), the radiation patterns have been calculated and shown in Fig. 5–2(a) and Fig. 5–2(b). Although the direct feed radiation is not included in the formulae for calculating the radiation pattern, it has been included in the patterns shown in the following figures. It is obvious that there is a singularity at the shadow boundary $\theta=a$.

Later on, Knop [15] extended Rusch's formulas to include the shadow boundary region. These formulas will be derived in the next section.

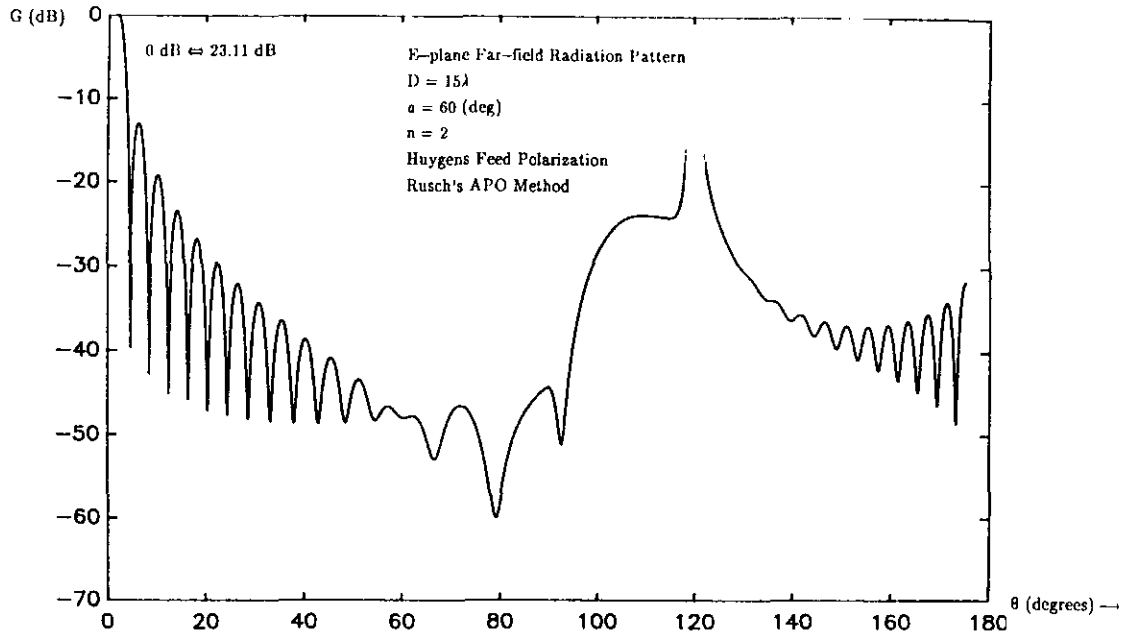

Fig. 5–2(a) E–plane Far–field Radiation Pattern of a Focus–fed Axially Symmetrical Paraboloid

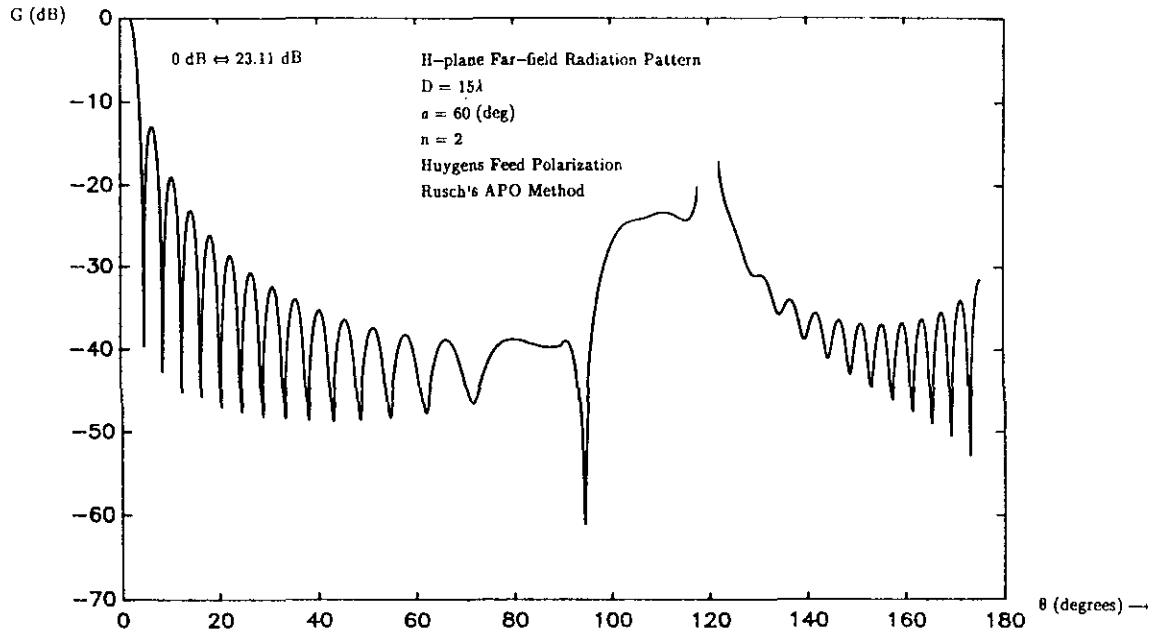

Fig. 5–2(b) H–plane Far–field Radiation Pattern of a Focus–fed Axially Symmetrical Paraboloid

5.4 APO Method for the Shadow Boundary Region

To remove the singularity at the shadow boundary of Rusch's results for the paraboloidal reflector, Knop [15] used the following transformations instead of the ones given by Eq. (5–16):

$$x' = x'' + \frac{(x'')^2}{2a} + \frac{(y'')^2}{2a} \tag{5–29,a}$$

$$y' = y'' \tag{5–29,b}$$

and

$$x = x_{si} - \frac{x_{si}}{a}x'' - \frac{x_{si}}{2a^2}(x'')^2 - \frac{x_{si}}{2a^2}(y'')^2 + \frac{y_{si}}{a}y'' \tag{5–30,a}$$

$$y = y_{si} - \frac{y_{si}}{a}x'' - \frac{y_{si}}{2a^2}(x'')^2 - \frac{y_{si}}{2a^2}(y'')^2 - \frac{x_{si}}{a}y''. \tag{5–30,b}$$

Substitution of Eq.(5.13) and Eq.(5–30) in Eq. (5–10) gives:

$$\Phi(x'',y'') = \Phi(x_{si},y_{si}) + x''\Phi_{10,i} + (x'')^2\Phi_{02,i} + (y'')^2\Phi_{02,i} \tag{5–31}$$

By including a second–order term $(x'')^2\Phi_{02,i}$ in the phase function of Eq.(5–20), Knop obtained the fields:

$$\begin{bmatrix} E_{\theta,i} \\ E_{\phi,i} \end{bmatrix} = A_0 \frac{e^{-jk\rho_0 - jk(r \mp a\sin\theta - z_{sp}\cos\theta)}}{\rho_0 r} \begin{bmatrix} \frac{jae^{\mp j(\pi/4)}}{\sqrt{2}\,\sin\theta} \end{bmatrix}$$

$$\exp\left\{\pm j\frac{ka\sin\theta}{2}\left[1 \mp \frac{\mathrm{ctg}(\theta/2)}{\mathrm{ctg}(a/2)}\right]^2\right\}\left[(C_\pm - \tfrac{1}{2}) \mp j(S_\pm - \tfrac{1}{2})\right]$$

$$U^\pm(\theta)\begin{bmatrix} \left[\cos\theta \pm \frac{\sin\theta}{\mathrm{ctg}(a/2)}\right] \\ 1 \end{bmatrix}\begin{bmatrix} \sqrt{G_f(a)}\sin\phi \\ \sqrt{G_f(a)}\cos\phi \end{bmatrix} \tag{5–32}$$

where

$$\tan(\alpha/2)=a/(2f) \tag{5–33,a}$$

$$C_{\pm}=C(W^{\pm}) \tag{5–33,b}$$

$$S_{\pm}=S(W^{\pm}) \tag{5–33,c}$$

$$W^{\pm}=\left| \sqrt{\frac{ka\sin\theta}{\pi}} \left[1\mp \operatorname{ctg}(\theta/2)/\operatorname{ctg}(\alpha/2)\right] \right| \tag{5–33,d}$$

$$U^{\pm}(\theta)=\begin{cases} 1 & (\theta \geq \alpha) \\ \mp 1 & (\theta < \alpha) \end{cases} \tag{5–33,e}$$

$$C(x)=\int_0^x \cos\left(\frac{\pi}{2}x^2\right)dx \tag{5–33,f}$$

$$S(x)=\int_0^x \sin\left(\frac{\pi}{2}x^2\right)dx \tag{5–33,g}$$

By factorizing out the field incident to the edge, the phase factor and the caustic divergence factor, the remaining items of Eq.(5–32) can be identified as the physical optics diffraction coefficients:

$$\begin{bmatrix} D_{spo,i} \\ D_{hpo,i} \end{bmatrix} = e^{j(\pi/4)}\sqrt{a/(2\sin\theta)}\,\exp\left\{ \pm j\frac{ka\sin\theta}{2}\left[1\mp\frac{\operatorname{ctg}(\theta/2)}{\operatorname{ctg}(\alpha/2)}\right]^2\right\}\cdot$$
$$[(C_{\pm}-\tfrac{1}{2})\mp j(S_{\pm}-\tfrac{1}{2})]U^{\pm}(\theta)\begin{bmatrix} 1 \\ \left[\cos\theta\pm\frac{\sin\theta}{\operatorname{ctg}(\alpha/2)}\right] \end{bmatrix} \tag{5–34}$$

These physical optics diffraction coefficients, first obtained by Knop, have no singularity at the shadow boundary ($\theta=\alpha$) and are therefore continuous at and through the shadow boundary region. Fig. 5–3(a) and Fig. 5–3(b) show the E–plane and the H–plane radiation pattern calculated by means of Knop's improved formulas.

5.5 Corrected APO (CAPO)

Measurements presented by Knop and Ostertag [8] revealed that APO gave

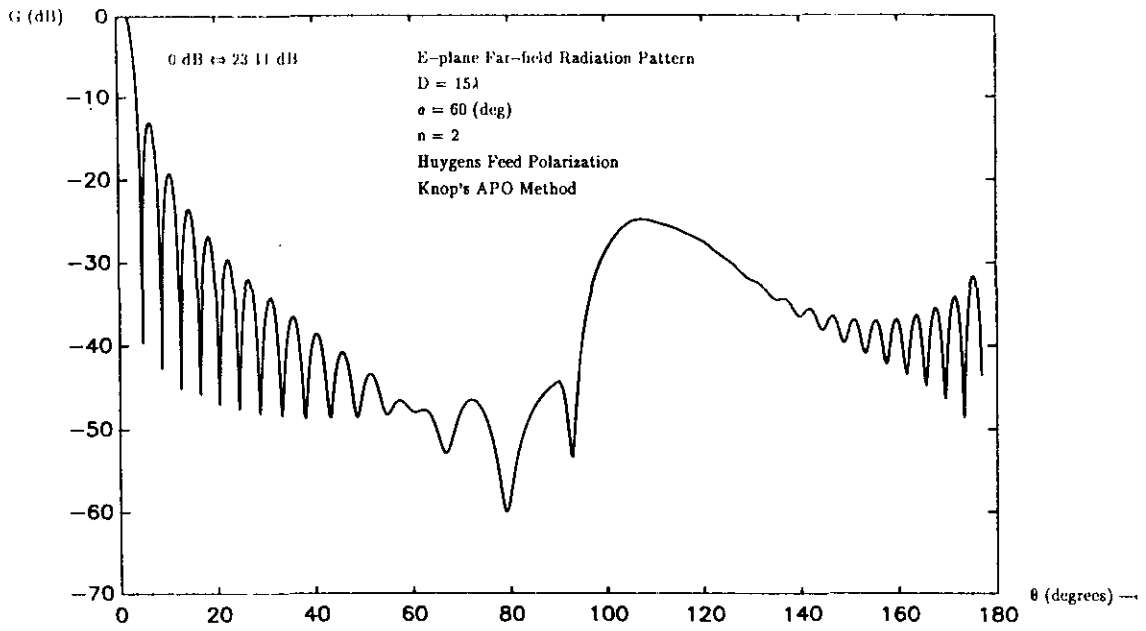

Fig. 5–3(a) E–plane Far–field Radiation Pattern of a Focus–fed Axially Symmetrical Paraboloid

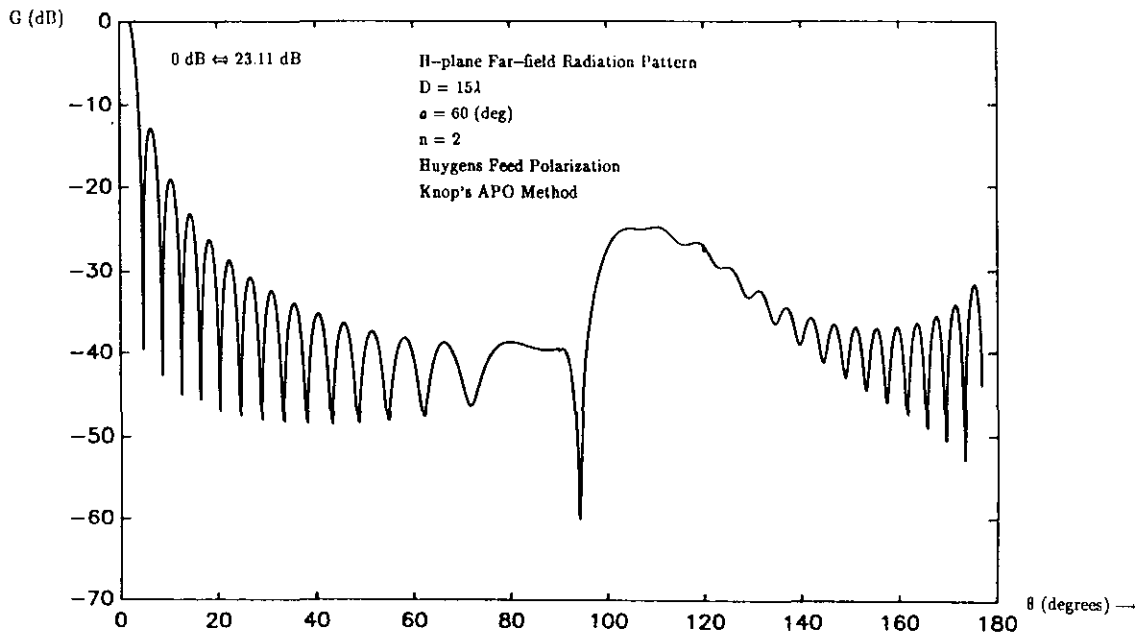

Fig. 5–3(b) H–plane Far–field Radiation Pattern of a Focus–fed Axially Symmetrical Paraboloid

errors up to 6dB in the shadow region (about $130^o \leq \theta \leq 175^o$ in their case). Since there are currents at the front of the reflector and no currents at the back of the reflector according to GO theory, a current discontinuity must occur at the edge of the reflector. Knop and Ostertag [8] suggested that the incorrect nature of the GO edge currents used in APO is the cause of errors in the far–field calculation and this was proved by measurements. They applied Sommerfeld's exact results and the PO results to the equivalent diffraction problem for a half plane, and gave the ratio of Sommerfeld's exact results to the PO results in order to correct the APO results.

These ratios are expressed by [8]:

$$\begin{bmatrix} K_s \\ K_h \end{bmatrix} = \begin{bmatrix} E_{exact}/E_{po} \\ H_{exact}/H_{po} \end{bmatrix} = \begin{bmatrix} |\sin(\frac{r^d}{2})/\cos(\frac{r^i}{2})| \\ |\cos(\frac{r^i}{2})/\sin(\frac{r^d}{2})| \end{bmatrix} \qquad (5\text{–}35)$$

where

E_{exact}	denotes Sommerfeld's exact results for the electric field parallel to the edge of a half plane,
H_{exact}	denotes Sommerfeld's exact results for the magnetic field parallel to the edge of a half plane,
E_{po}	denotes the PO results for the electric field parallel to the edge of a half plane,
H_{po}	denotes the PO results for the magnetic field parallel to the edge of a half plane,
r^i, r^d	defined as before (see Fig. 4–3 and Fig. 4–4).

By multiplying the APO diffraction coefficients with these ratios, the corrected APO (CAPO) diffraction coefficients will be obtained. Using the CAPO diffraction coefficients instead of the ones of APO, a new set of radiation patterns can be calculated. If a feed with an omnidirectional power pattern (n=0) is assumed and the direct feed radiation is not included, the radiation patterns shown in Fig. 5–4(a) and Fig. 5–4(b) are obtained, they agree with the patterns calculated by Knop for such an antenna system in [8]. Comparing CAPO with the measurements found by Knop and Ostertag [8] showed that the CAPO prediction agrees with measurements even in the shadow region. The radiation patterns found with CAPO for our antenna system have also been calculated and shown in Fig. 5–5(a), and Fig.5–5(b).

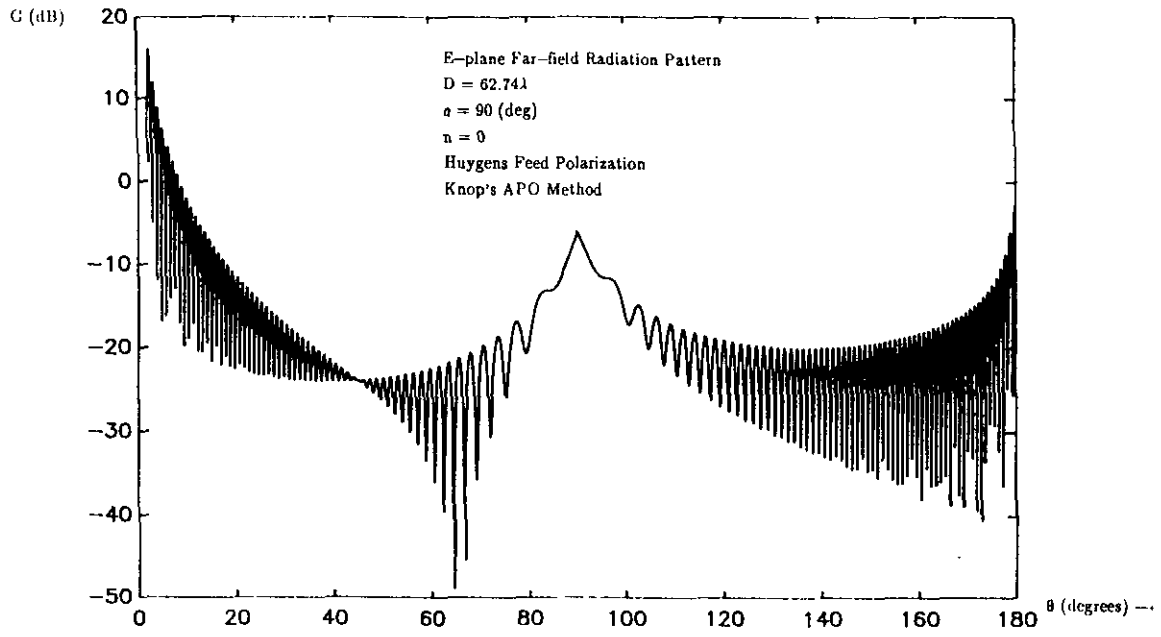

Fig. 5–4(a) E–plane Far–field Radiation Pattern of a Focus–fed Axially Symmetrical Paraboloid

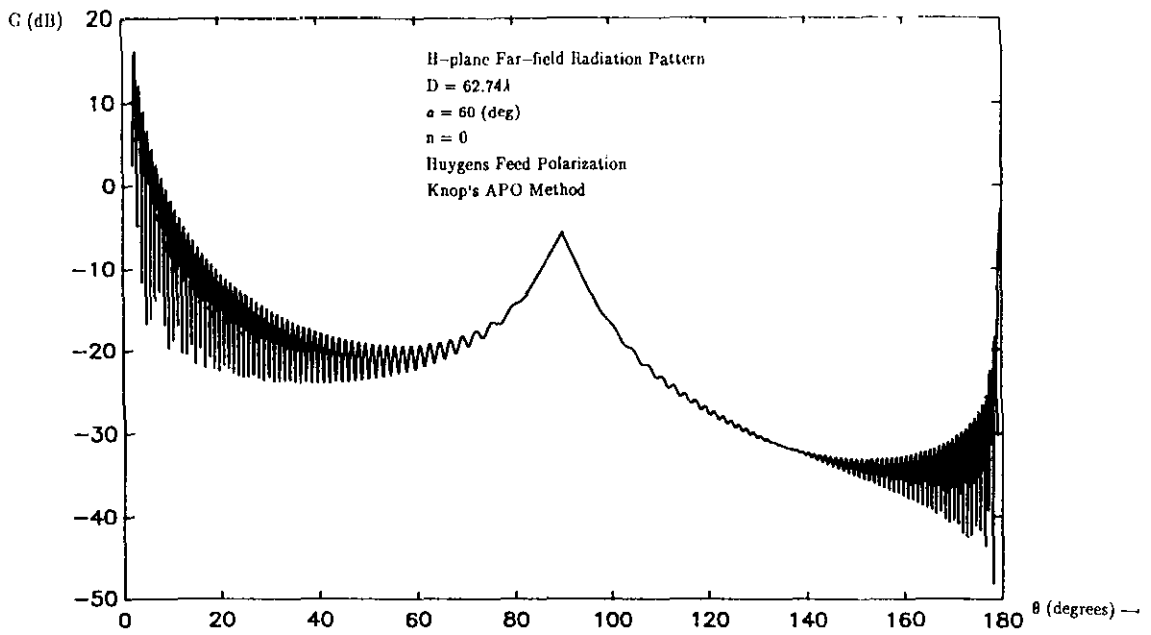

Fig. 5–4(b) H–plane Far–field Radiation Pattern of a Focus–fed Axially Symmetrical Paraboloid

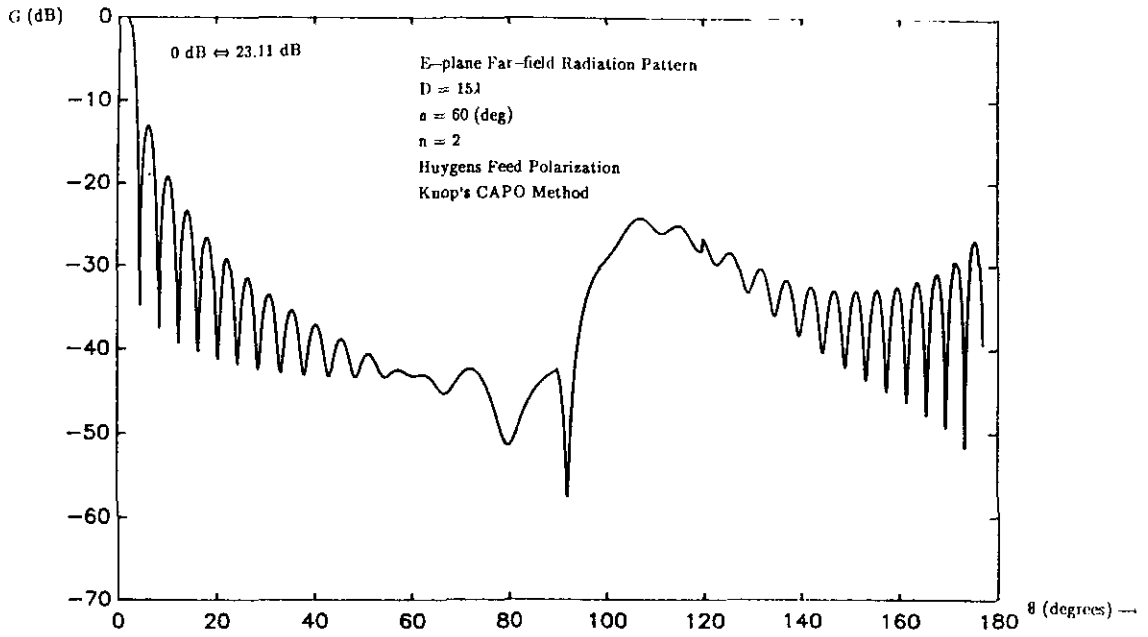

Fig. 5–5(a) E–plane Far–field Radiation Pattern of a Focus–fed Axially Symmetrical Paraboloid

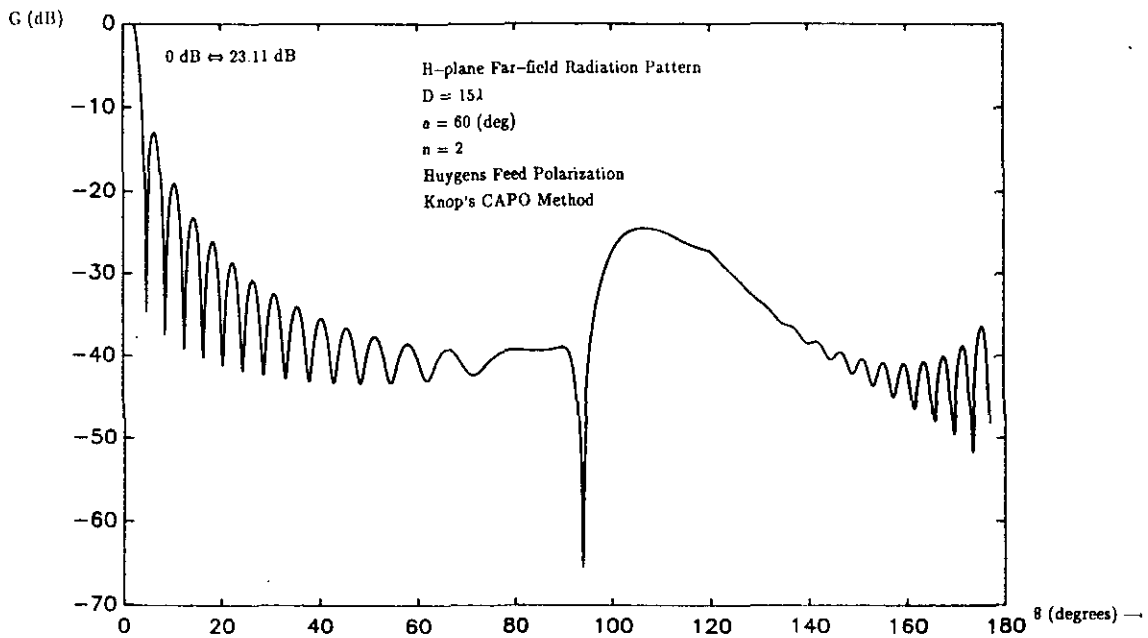

Fig. 5–5(b) H–plane Far–field Radiation Pattern of a Focus–fed Axially Symmetrical Paraboloid

6. Caustic Region Analysis by EEC

6.1 Introduction

The rear–axial direction of the symmetrical parabolic reflector must be one of the caustics since diffracted rays from the whole edge of the reflector effectively contribute to the field on the symmetry axis. Therefore, we cannot use the GTD method which only takes into account two edge points (see chapter 4). Now, a technique, named the Equivalent Edge Current Method (EEC or ECM [9]–[11]), is employed to calculate the field in the rear–direction. The EEC method uses both the diffraction theory (to obtain the equivalent edge currents) and radiation field integrals (to sum the contribution from the edge) in order to obtain the total field in the rear–axial region.

6.2 Equivalent Edge Current Calculation

Again we must assume that the paraboloid is in the far–field zone of the feed and the feed has the same pattern form as in Chapter 2. For an y–axis polarized feed with the polarization properties of an Huygens source, the following holds:

$$\vec{E}_f(\rho,\psi,\xi)=A_0\frac{e^{-jk\rho}}{\rho}\left[\sqrt{G_f(\psi)}\sin\xi\ \vec{\psi}+\sqrt{G_f(\psi)}\cos\xi\ \vec{\xi}\right] \qquad (6\text{–}1,a)$$

$$\vec{H}_f(\rho,\psi,\xi)=A_0\frac{e^{-jk\rho}}{\eta\rho}\left[-\sqrt{G_f(\psi)}\cos\xi\ \vec{\psi}+\sqrt{G_f(\psi)}\sin\xi\ \vec{\xi}\right] \qquad (6\text{–}1,b)$$

The incident fields on the edge of the paraboloid are:

$$\vec{E}_f(\rho_0,a,\xi)=A_0\frac{e^{-jk\rho_0}}{\rho_0}\left[\sqrt{G_f(a)}\sin\xi\ \vec{\psi}+\sqrt{G_f(a)}\cos\xi\ \vec{\xi}\right] \qquad (6\text{–}2,a)$$

$$\vec{H}_f(\rho_0,a,\xi)=A_0\frac{e^{-jk\rho_0}}{\eta\,\rho_0}\left[-\sqrt{G_f(a)}\cos\xi\ \vec{\psi}+\sqrt{G_f(a)}\sin\xi\ \vec{\xi}\right] \qquad (6\text{–}2,b)$$

Using the GTD diffraction coefficients presented previously, the diffracted fields can be expressed by (see Fig. 6–1):

$$E_{\phi}^{d} = E_{f_{\xi}}^{i} \cdot D_s \cdot \frac{1}{\sqrt{s}} \cdot e^{-jks} \tag{6–3,a}$$

$$E_{\theta}^{d} = E_{f_{\psi}}^{i} \cdot D_h \cdot \frac{1}{\sqrt{s}} \cdot e^{-jks} \tag{6–3,b}$$

Due to the relation between the diffracted field components:

$$H_{\phi}^{d} = \frac{1}{\eta} E_{\theta}^{d} \tag{6–3,c}$$

and the relation between the incident field components:

$$H_{f_{\xi}}^{i} = \frac{1}{\eta} E_{f_{\psi}}^{i}, \tag{6–3,d}$$

it is possible to derive:

$$\begin{aligned} H_{\phi}^{d} &= \frac{1}{\eta} E_{\theta}^{d} \\ &= \frac{1}{\eta} E_{f_{\psi}}^{i} \cdot D_h \cdot \frac{1}{\sqrt{s}} \cdot e^{-jks} \\ &= H_{f_{\xi}}^{i} \cdot D_h \cdot \frac{1}{\sqrt{s}} \cdot e^{-jks} \end{aligned} \tag{6–3,e}$$

where

E_{ϕ}^{d}, $E_{f_{\xi}}^{i}$ are the electric fields in the ϕ–direction parallel to the edge of the reflector,

E_{θ}^{d}, $E_{f_{\psi}}^{i}$ are the electric fields in the θ–direction perpendicular to the edge of the reflector,

H_{ϕ}^{d}, $H_{f\xi}^{i}$ are the magnetic fields in the ϕ–direction parallel to the edge of the reflector,

H^{d}_{θ}, $H_{f}{}^{i}_{\psi}$ are the magnetic fields in the θ–direction perpendicular to the edge of the reflector,

$\frac{1}{\sqrt{s}}$ is the caustic divergence factor derived from Eq. (4–7), or Eq. (4–10), in the rear–direction $\theta \to 0$, $\rho_c \to \infty$.

It is possible to obtain any field with knowledge of two out of the four components E_θ, E_ϕ, H_θ and H_ϕ through the relation given by the Eq. (5–2), E_ϕ and H_ϕ are used in the calculations.

Further, the electromagnetic far–field produced by an infinite long electric current filament I along the z–axis of a rectangular coordinate system (see Fig. 6–2) is given by:

$$E_z = -\eta k I \sqrt{\frac{j}{8\pi ks}}\, e^{-jks} \qquad \text{for } s \gg \lambda \qquad (6\text{–}4)$$

$$H_\phi = -kI \sqrt{\frac{j}{8\pi ks}}\, e^{-jks}$$

where s is the distance from the current filament to the observation point.

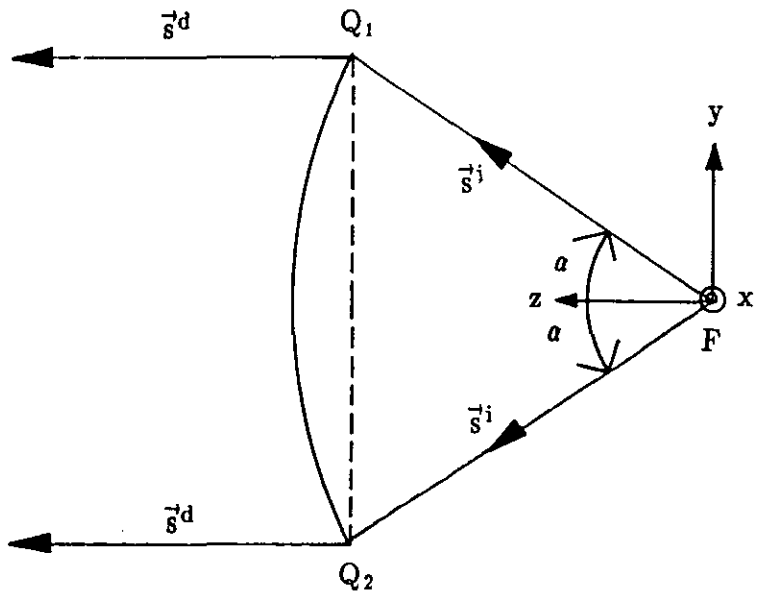

Fig. 6–1 Diffracted Rays in the Rear Caustic Direction

If there is an electric current I_ξ^e and a magnetic current I_ξ^m on the edge and if these currents can be locally taken as infinite straight line currents (shown in Fig.6–2) by considering them as local diffraction phenomena at high frequencies, the electric current I_ξ^e and the magnetic current I_ξ^m on the edge of the reflector will be:

$$E_\phi^d = -\eta k I_\xi^e \sqrt{\frac{j}{8\pi ks}}\, e^{-jks} \qquad (6\text{–}5,a)$$

$$H_\phi^d = -\frac{k}{\eta} I_\xi^m \sqrt{\frac{j}{8\pi ks}}\, e^{-jks} \qquad (6\text{–}5,b)$$

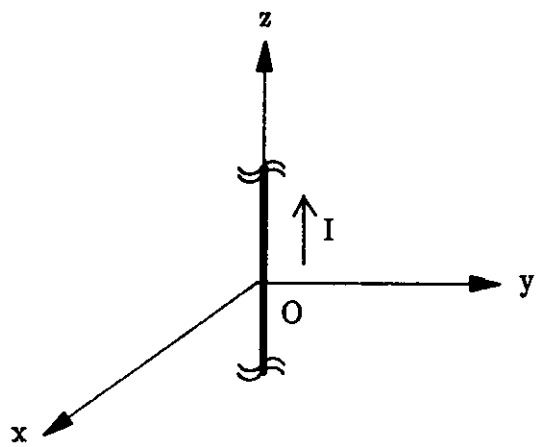

Fig. 6–2 An Infinite Filament I Along the z–axis

Comparing Eq. (6–5) with Eq. (6–3) and using the equivalence conception, it is possible to see the diffracted fields as induced by a proper electric current I_ξ^e and a magnetic current I_ξ^m on the edge. The currents, called the equivalent edge currents (see Fig. 6–3), are given by:

$$I_{\xi}^{e} = -\frac{2\sqrt{2\pi k}}{\eta k} e^{-j(\pi/4)} E_{f_{\xi}}^{i} \cdot D_s \qquad (6\text{–}6,a)$$

$$I_{\xi}^{m} = -\eta \frac{2\sqrt{2\pi k}}{k} e^{-j(\pi/4)} H_{f_{\xi}}^{i} \cdot D_h \qquad (6\text{–}6,b)$$

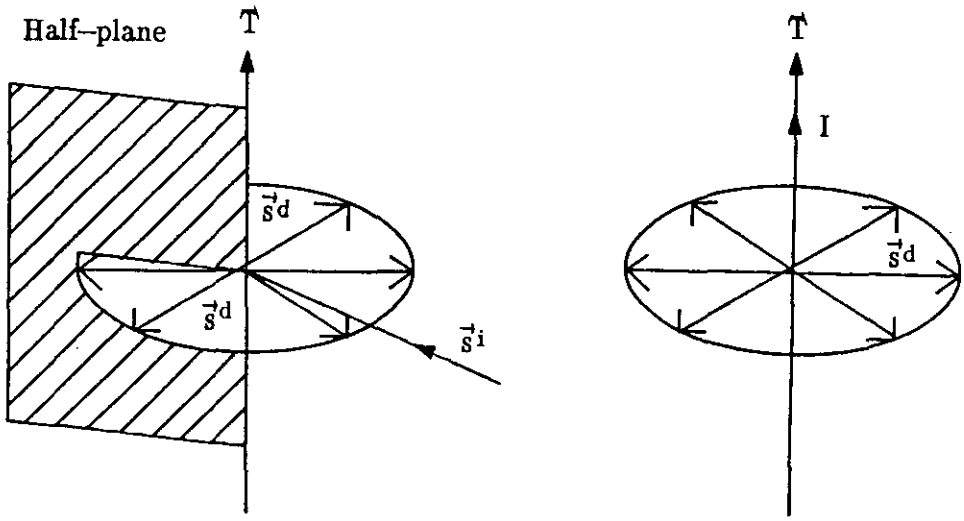

(a) Diffraction at the Edge of Half–plane

(b) Equivalent Edge Current Sources

Fig. 6–3 Equivalence Conception

6.3 Edge Current Integration

The field in the rear–axial region is obtained by integrating the fields produced by the equivalent currents on the edge of the reflector:

$$\vec{E}^{e}(r,\theta,\phi) = -j\frac{k\eta}{4\pi r} e^{-jkr} \int_{l} [\vec{I}_{\xi}^{e} - (\vec{I}_{\xi}^{e} \cdot \vec{r})\vec{r}] e^{jk\rho_0(\vec{\rho}\cdot\vec{r})} dl \qquad (6\text{–}7,a)$$

$$\vec{H}^{m}(r,\theta,\phi) = -j\frac{k/\eta}{4\pi r} e^{-jkr} \int_{l} [\vec{I}_{\xi}^{m} - (\vec{I}_{\xi}^{m} \cdot \vec{r})\vec{r}] e^{jk\rho_0(\vec{\rho}\cdot\vec{r})} dl \qquad (6\text{–}7,b)$$

The vectors $\vec{E}^e(r,\theta,\phi)$ and $\vec{H}^m(r,\theta,\phi)$ of Eq. (6–7) can also be written in the form:

$$\begin{bmatrix} E^e_\theta \\ E^e_\phi \end{bmatrix} = -j\frac{k\eta}{4\pi r} e^{-jkr} \int_0^{2\pi} \begin{bmatrix} I^e_\xi \cos\theta \sin(\phi-\xi) \\ I^e_\xi \cos(\phi-\xi) \end{bmatrix} e^{j[\tau\cos(\phi-\xi)+\delta]} a\, d\xi \qquad (6\text{–}8,a)$$

$$\begin{bmatrix} H^m_\theta \\ H^m_\phi \end{bmatrix} = -j\frac{k/\eta}{4\pi r} e^{-jkr} \int_0^{2\pi} \begin{bmatrix} I^m_\xi \cos\theta \sin(\phi-\xi) \\ I^m_\xi \cos(\phi-\xi) \end{bmatrix} e^{j[\tau\cos(\phi-\xi)+\delta]} a\, d\xi \qquad (6\text{–}8,b)$$

where

$$k\rho_0(\vec{\rho}\cdot\vec{r}) = k\rho_0 \sin\alpha \sin\theta \cos(\phi-\xi) + k\rho_0 \cos\alpha \cos\theta = \tau\cos(\phi-\xi) + \delta \qquad (6\text{–}8,c)$$

and

$$\begin{bmatrix} E^m_\theta \\ E^m_\phi \end{bmatrix} = \eta \begin{bmatrix} H^m_\phi \\ -H^m_\theta \end{bmatrix} = -j\frac{k}{4\pi r} e^{-jkr} \int_0^{2\pi} \begin{bmatrix} I^m_\xi \cos(\phi-\xi) \\ -I^m_\xi \cos\theta \sin(\phi-\xi) \end{bmatrix} e^{j[\tau\cos(\phi-\xi)+\delta]} a\, d\xi \qquad (6\text{–}8,d)$$

Substitution of I^e_ξ and I^m_ξ in Eq. (6–8) yields:

$$\begin{bmatrix} E^e_\theta \\ E^e_\phi \end{bmatrix} = \frac{E_0\sqrt{G_f(a)}\nu_s}{4\pi r} e^{-jkr} \left\{ \int_0^{2\pi} \cos\xi \begin{bmatrix} \cos\theta \sin(\phi-\xi) \\ \cos(\phi-\xi) \end{bmatrix} e^{j\tau\cos(\phi-\xi)} d\xi \right\} a e^{j\delta} \qquad (6\text{–}9,b)$$

$$\begin{bmatrix} E^m_\theta \\ E^m_\phi \end{bmatrix} = \frac{E_0\sqrt{G_f(a)}\nu_h}{4\pi r} e^{-jkr} \left\{ \int_0^{2\pi} \sin\xi \begin{bmatrix} \cos(\phi-\xi) \\ -\cos\theta \sin(\phi-\xi) \end{bmatrix} e^{j\tau\cos(\phi-\xi)} d\xi \right\} a e^{j\delta} \qquad (6\text{–}9,a)$$

where

$$E_0 = A_0 \frac{e^{-jk\rho_0}}{\rho_0} \qquad (6\text{–}10,a)$$

$$\nu_s = D_s \cdot 2\sqrt{2\pi k} \cdot e^{j(\pi/4)} = \frac{1}{\sin(\frac{a}{2})} - 1 \qquad (6\text{–}10,b)$$

$$\nu_h = D_h \cdot 2\sqrt{2\pi k}\cdot e^{j(\pi/4)} = \frac{1}{\sin(\frac{a}{2})} + 1. \qquad (6\text{–}10,c)$$

For the rear–axial direction $\theta=0$, the modified Fresnel integrals in D_h and D_s equals unity (see Fig. 4–6); so, the integrals can be expressed in the form of Bessel functions:

$$\begin{bmatrix} E^e_\theta \\ E^e_\phi \end{bmatrix} = \frac{E_0\sqrt{G_f(a)}\nu_s}{4r} e^{-jkr} \begin{bmatrix} \cos\theta[J_0(\tau)+J_2(\tau)]\sin\phi \\ [J_0(\tau)-J_2(\tau)]\cos\phi \end{bmatrix} a e^{j\delta} \qquad (6\text{–}11,a)$$

$$\begin{bmatrix} E^m_\theta \\ E^m_\phi \end{bmatrix} = \frac{E_0\sqrt{G_f(a)}\nu_h}{4r} e^{-jkr} \begin{bmatrix} [J_0(\tau)-J_2(\tau)]\sin\phi \\ \cos\theta[J_0(\tau)+J_2(\tau)]\cos\phi \end{bmatrix} a e^{j\delta} \qquad (6\text{–}11,b)$$

This finally results in the total field in the rear–axial direction:

$$\begin{bmatrix} E_\theta \\ E_\phi \end{bmatrix} = \begin{bmatrix} E^e_\theta \\ E^e_\phi \end{bmatrix} + \begin{bmatrix} E^m_\theta \\ E^m_\phi \end{bmatrix} = \frac{aE_0 e^{j\delta}}{4r} e^{-jkr}$$

$$\begin{bmatrix} \{\sqrt{G_f(a)}\nu_s\cos\theta[J_0(\tau)+J_2(\tau)]+\sqrt{G_f(a)}\nu_h[J_0(\tau)-J_2(\tau)]\}\sin\phi \\ \{\sqrt{G_f(a)}\nu_s[J_0(\tau)-J_2(\tau)]+\sqrt{G_f(a)}\nu_h\cos\theta[J_0(\tau)+J_2(\tau)]\}\cos\phi \end{bmatrix} \qquad (6\text{–}12)$$

Here, we will keep the angle θ in the Eq. (6–12) because Ratnasiri et al. [18] found that D_s and D_h are slowly varying functions in the rear–axial region and the formula can also be used to calculate the field in the angel region close to the rear–axial direction ($\theta=0$).

Eq. (6–12) holds for all ϕ angles. The E–plane ($\phi=\frac{\pi}{2}$) and H–plane ($\phi=0$) radiation patterns, calculated with EEC are shown in Fig. 6–4(a) and Fig. 6–4(b), respectively.

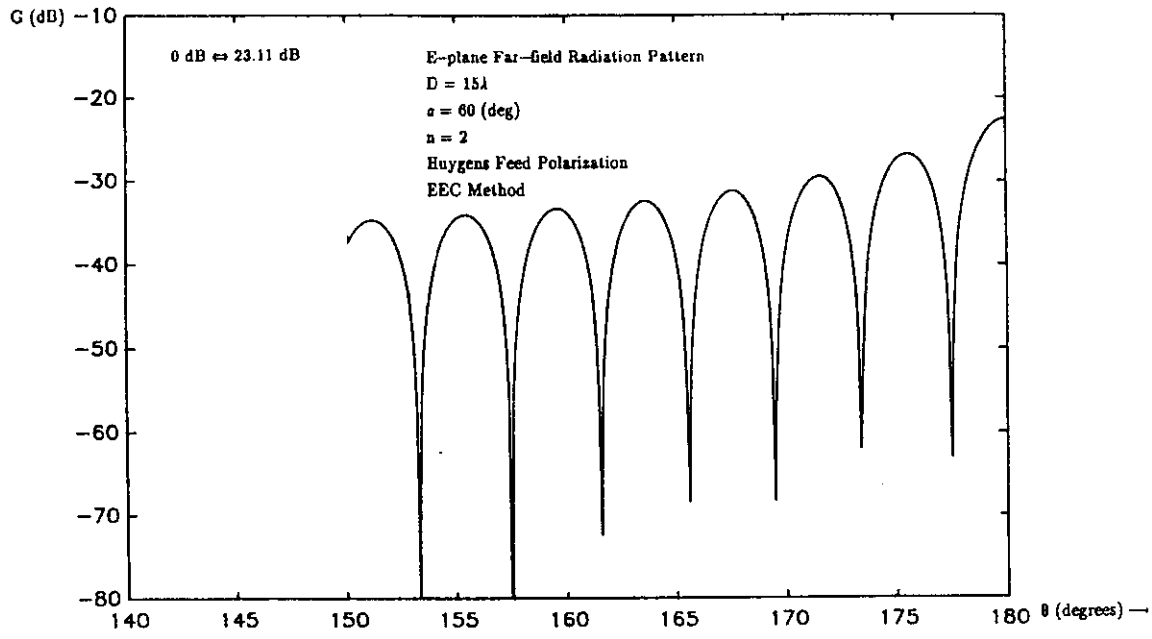

Fig. 6–4(a) Far–field Radiation Pattern in the Rear–axial Region of a Focus–fed Axially Symmetrical Paraboloid

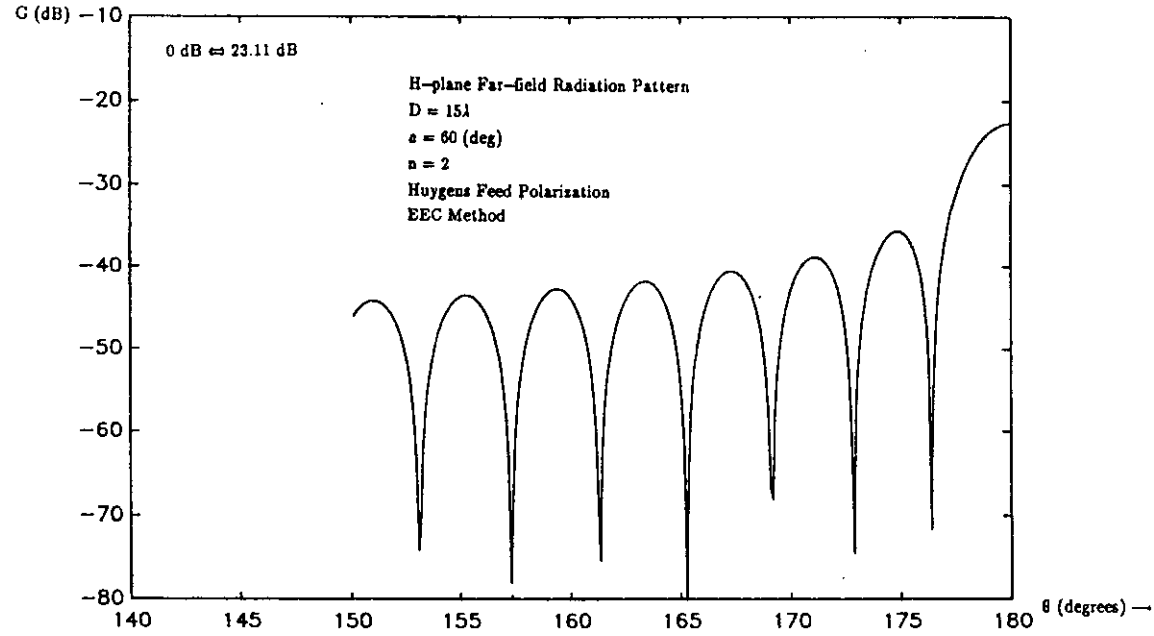

Fig. 6–4(b) Far–field Radiation Pattern in the Rear–axial Region of a Focus–fed Axially Symmetrical Paraboloid

7. Comparison of the Different High Frequency Asymptotic Techniques

In the preceding sections, the GTD (UTD), APO (CAPO) and EEC methods were used to calculate the wide–angle radiation pattern of a symmetric parabolic reflector antenna. Therefore, it is interesting to compare the results obtained by these methods.

7.1 Comparison of GTD and UTD

As mentioned before, Kouyoumjian's UTD [6] is an extension to Keller's GTD [12] and they are based on the same principles. Therefore, both methods are generally called GTD, although they do have differences. In this part of the report, we will compare both methods and emphasize the principle differences between them, in order to distinguish between them we will use the terms GTD and UTD in the following part of the report.

For the sake of a comparison, we will repeat the expressions for the diffracted fields that are obtained when using these methods. The expression given by Keller in [12] for the diffraction of a plane scalar wave at a straight edge of a half plane is:

$$U_e = D \cdot U_i \cdot \frac{1}{\sqrt{r}} \cdot e^{-jkr} \tag{7–1}$$

where U_e is the scalar diffracted field, U_i is the scalar incident field at the diffraction point, r is the distance from the diffraction point to the observation point, and D is the diffraction coefficient given by:

$$D_{\substack{s \\ h}} = -\frac{e^{-j(\pi/4)}}{2\sqrt{2\pi k}\sin\beta_0}\left[\frac{1}{\cos\frac{r^d - r^i}{2}} \mp \frac{1}{\cos\frac{r^d + r^i}{2}}\right] \tag{7–2}$$

The expression given by Kouyoumjian [6] for the diffracted field is:

$$\vec{E}^d(P) = \overline{D} \cdot \vec{E}^i(Q_i) \cdot A(s_i^i, s_i^d) e^{-jks_i^d} \tag{7–3}$$

where all the parameters are those defined in Chapter 4.

It is obvious that Eq. (7–1) is a scalar formula and Eq. (7–3) is a vector formula. So, the latter can be used to calculate field vectors. Due to the vector property of Eq. (7–3), the diffraction coefficient $\overline{D}$ in Eq. (7–3) takes the form of a matrix. In the ray–fixed coordinate system [6], the matrix $\overline{D}$ reduces to a diagonal dyadic matrix, having two non–zero elements: D_s being the diffraction coefficient under the soft boundary condition and D_h the diffraction coefficient under the hard boundary condition given by:

$$D_{\substack{s\\h}}=-\frac{e^{-j(\pi/4)}}{2\sqrt{2\pi k}\sin\beta_0}\left\{\frac{F[kL^i a(r^d-r^i)]}{\cos\frac{r^d-r^i}{2}}\mp\frac{F[kL^r a(r^d+r^i)]}{\cos\frac{r^d+r^i}{2}}\right\} \tag{7–4}$$

as in Eq. (4–12) with

$$F(z)=2j\sqrt{z}\exp(jz)\int_{\sqrt{z}}^{\infty}\exp(-j\tau^2)d\tau, \tag{7–4,a}$$

$$a(r^d\mp r^i)=2\cos^2\left(\frac{r^d\mp r^i}{2}\right), \tag{7–4,b}$$

L^i and L^r are the distance parameters. (7–4,c)

The only difference between $D_{s,h}$ from Eq. (7–2) and those given by Eq. (7–4), is in the modified Fresnel integral which was introduced by Kouyoumjian to remove the discontinuity of the edge diffraction coefficients given by Keller. It is shown in Fig. 4–6 that the integral $F(z) \to 1$ when $z \to \infty$. So, Eq. (7–2) becomes (7–4) when the observation point concerned is away from the forward–direction ($\theta=\pi$) and shadow boundary ($\theta=\alpha$).

Due to the vector property of UTD and its validity for all wide–angle regions, the UTD formulas have been used to calculate the radiation patterns in Chapter 4.

7.2 Comparison of APO and CAPO

Since both APO and CAPO are derived in detail in Chapter 5, it is possible

to make a comparison between the results calculated by APO and by CAPO. They are plotted together in Figs. 7–1(a) and 7–1(b).

It can be seen that there are regions where the difference is great. CAPO is supposed to correct the errors in APO, which is supported by measurements [8].

7.3 Comparison of GTD (UTD) and (C)APO

7.3.1 Diffraction Coefficient Comparison of GTD and APO

Finally, for ease and clarity, Keller's GTD and Rusch's APO diffraction coefficients are compared (because Kouyoumjian's GTD and Knop's APO affect only the fields at or near the shadow boundary of $\theta=\alpha$).

After deleting the direct radiation from the feed, the GTD results from Eq.(4–42), can be written as:

$$\begin{bmatrix} E^d_{\theta_1} \\ E^d_{\phi_1} \end{bmatrix} = A_0 \frac{e^{-jk\rho_0}}{\rho_0} \sqrt{G_f(\alpha)} \begin{bmatrix} U_\alpha \sin\phi \\ \cos\phi \end{bmatrix} \left[\frac{1}{r} \sqrt{\frac{a}{\sin\theta}} \right] e^{-jkr} \cdot e^{jk\rho_0 \cos(\alpha-\theta)}$$

$$\left\{ \frac{e^{-j(\pi/4)}}{2\sqrt{2\pi k}} \left[\frac{1}{\sin(\frac{\alpha-\theta}{2})} \pm \frac{1}{\cos(\frac{\theta}{2})} \right] \right\} \qquad (7\text{–}5,a)$$

$$\begin{bmatrix} E^d_{\theta_2} \\ E^d_{\phi_2} \end{bmatrix} = A_0 \frac{e^{-jk\rho_0}}{\rho_0} \sqrt{G_f(\alpha)} \begin{bmatrix} U_\alpha \sin\phi \\ \cos\phi \end{bmatrix} \left[\frac{e^{j(\pi/2)}}{r} \sqrt{\frac{a}{\sin\theta}} \right] e^{-jkr} \cdot e^{jk\rho_0 \cos(\alpha+\theta)}$$

$$\left\{ \epsilon_0 \frac{e^{-j(\pi/4)}}{2\sqrt{2\pi k}} \left[\frac{1}{\sin(\frac{\alpha+\theta}{2})} \pm \frac{1}{\cos(\frac{\theta}{2})} \right] \right\} \qquad (7\text{–}5,b)$$

From the above formulas it is easy to extract the diffraction coefficients:

$$D_{sgtd,1} = \frac{e^{-j(\pi/4)}}{2\sqrt{2\pi k}} \left[\frac{1}{\sin(\frac{\alpha-\theta}{2})} - \frac{1}{\cos(\frac{\theta}{2})} \right] \qquad (7\text{–}6,a)$$

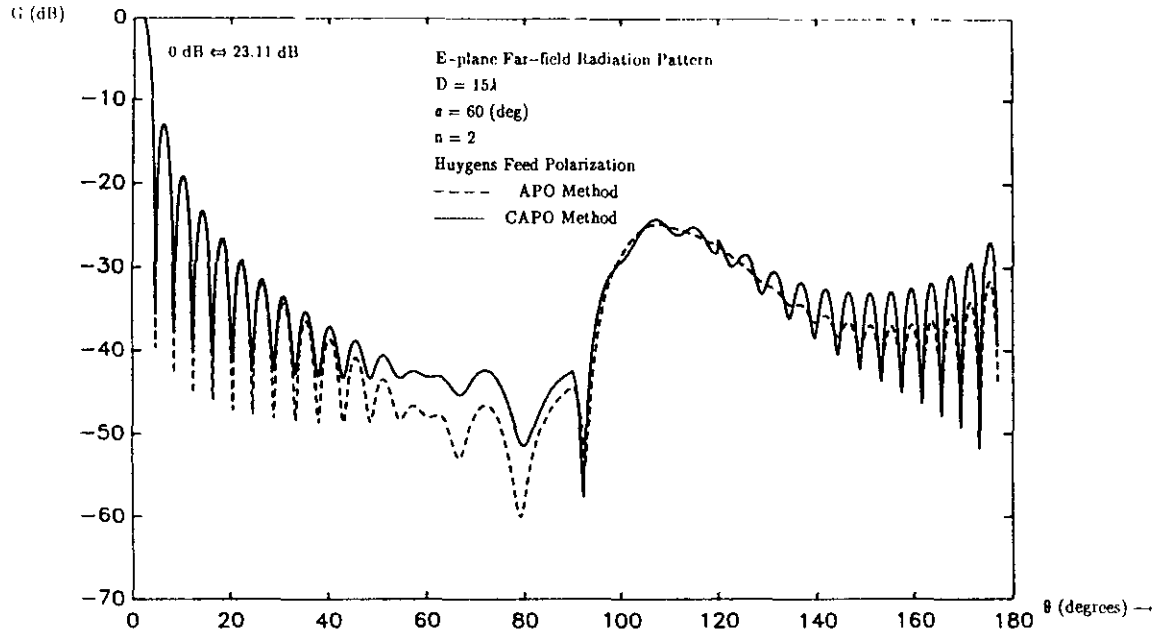

Fig. 7–1(a) E–plane Far–field Radiation Pattern of a Focus–fed Axially Symmetrical Paraboloid

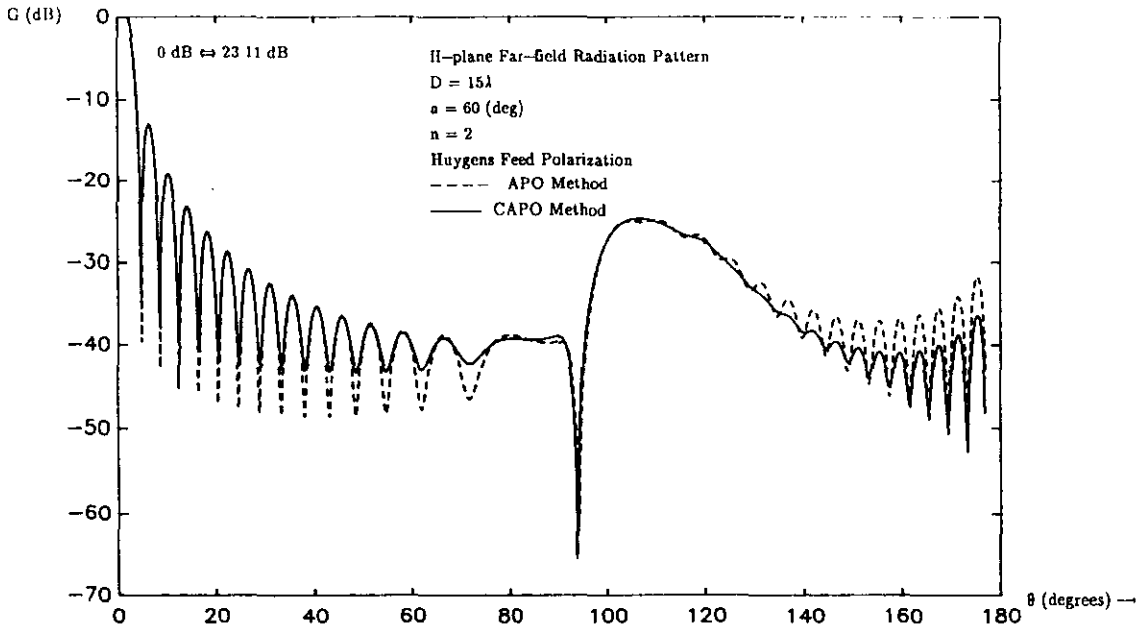

Fig. 7–1(b) H–plane Far–field Radiation Pattern of a Focus–fed Axially Symmetrical Paraboloid

$$D_{hgtd,1}=\frac{e^{-j(\pi/4)}}{2\sqrt{2\pi k}}\left[\frac{1}{\sin(\frac{a-\theta}{2})}+\frac{1}{\cos(\frac{\theta}{2})}\right] \tag{7-6,b}$$

$$D_{sgtd,2}=\epsilon_0\frac{e^{-j(\pi/4)}}{2\sqrt{2\pi k}}\left[\frac{1}{\sin(\frac{a+\theta}{2})}-\frac{1}{\cos(\frac{\theta}{2})}\right] \tag{7-6,c}$$

$$D_{hgtd,2}=\epsilon_0\frac{e^{-j(\pi/4)}}{2\sqrt{2\pi k}}\left[\frac{1}{\sin(\frac{a+\theta}{2})}+\frac{1}{\cos(\frac{\theta}{2})}\right] \tag{7-6,d}$$

The diffraction coefficients from the APO method can also be derived from Eq. (5–28) easily:

$$D_{sapo,1}=-\frac{e^{-j(\pi/4)}}{2\sqrt{2\pi k}}\left[\frac{2}{\sin\theta-(\frac{\sin a}{1+\cos a})(1+\cos\theta)}\right] \tag{7-7,a}$$

$$D_{hapo,1}=-\frac{e^{-j(\pi/4)}}{2\sqrt{2\pi k}}\left[\frac{2(\cos\frac{a}{2}\cos\theta+\sin\theta\sin\frac{a}{2})/\cos\frac{a}{2}}{\sin\theta-(\frac{\sin a}{1+\cos a})(1+\cos\theta)}\right] \tag{7-7,b}$$

$$D_{sapo,2}=-\frac{e^{-j(\pi/4)}}{2\sqrt{2\pi k}}\left[\frac{-2}{\sin\theta+(\frac{\sin a}{1+\cos a})(1+\cos\theta)}\right] \tag{7-7,c}$$

$$D_{hapo,2}=-\frac{e^{-j(\pi/4)}}{2\sqrt{2\pi k}}\left[\frac{-2(\cos\frac{a}{2}\cos\theta-\sin\theta\sin\frac{a}{2})/\cos\frac{a}{2}}{\sin\theta+(\frac{\sin a}{1+\cos a})(1+\cos\theta)}\right] \tag{7-7,d}$$

The diffraction coefficients (the quantities in square–brackets) in Eqs. (7–6) and (7–7) are included in Figs. 7–2(a) and 7–2(b). The comparison performed is not only for the D_s of the upper diffraction points (Fig. 7–2(a)) but also for the lower (Fig. 7–2(b)), also for the D_h of both points (which was not included by Rusch[7]). The diffraction coefficients of the lower point have not been compared in the angle region $\frac{\pi-a}{2}\leq\theta\leq\frac{\pi}{2}$, because the diffracted ray from the lower diffraction point to the observation point is blocked by the reflector there.

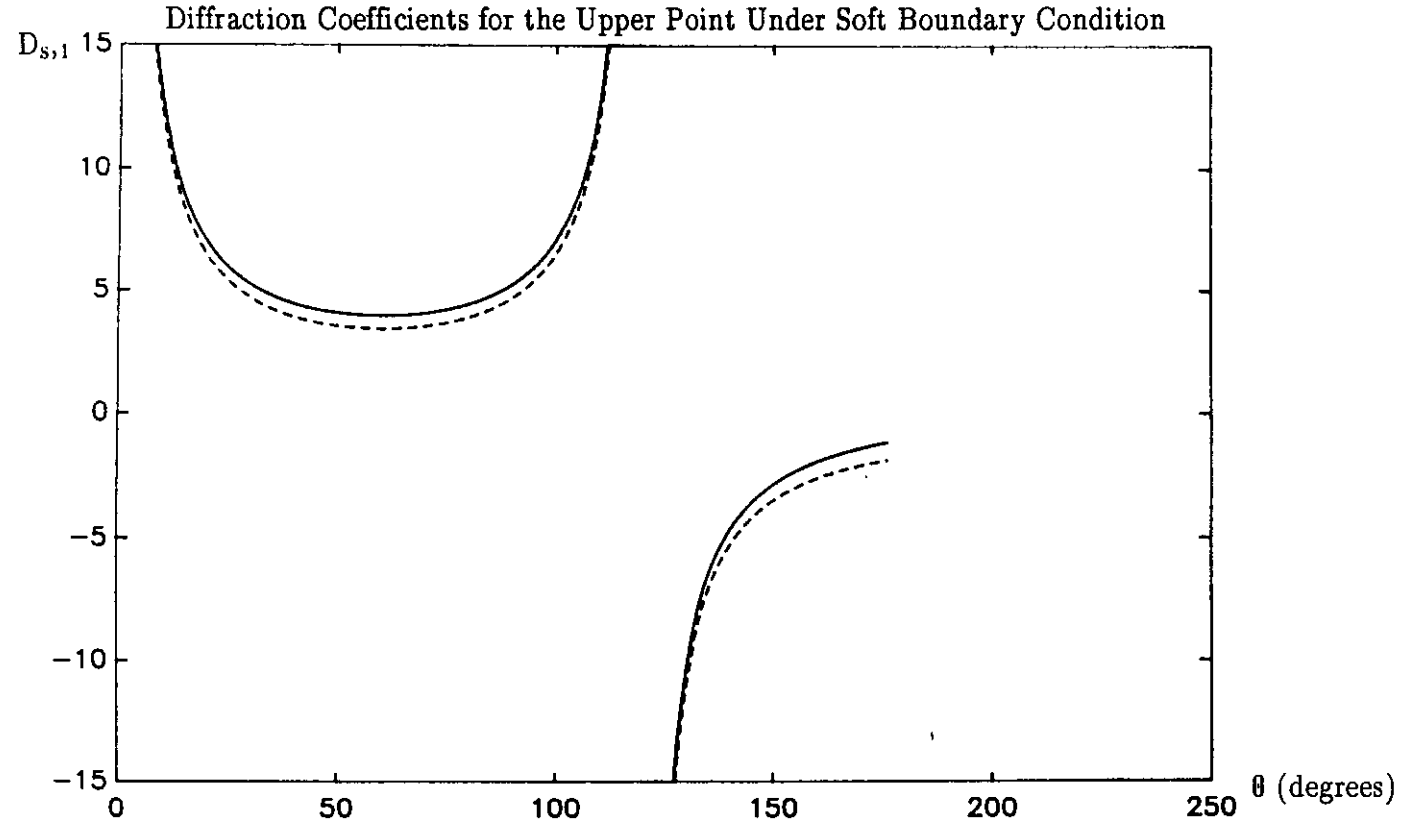

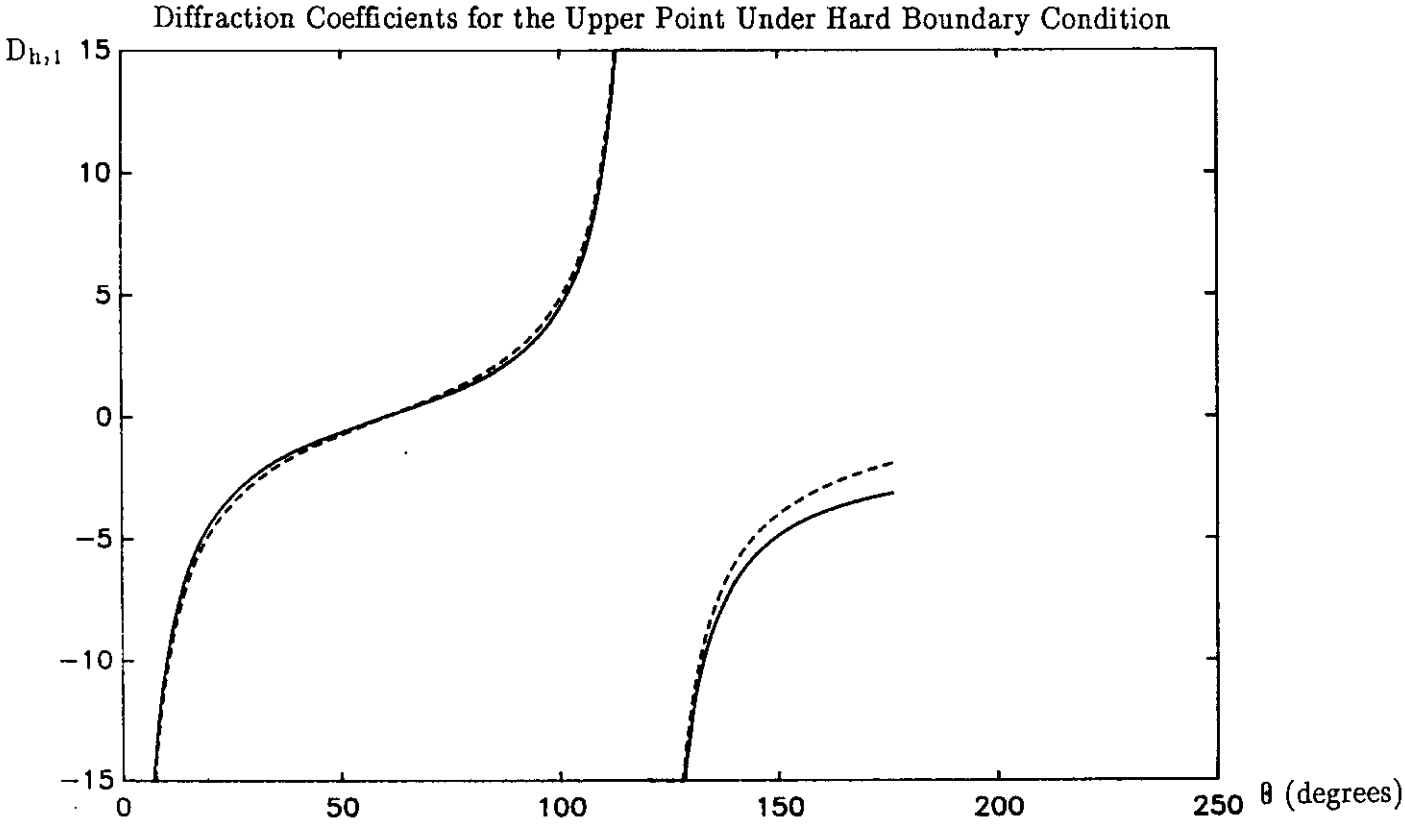

Fig. 7–2(a) Diffraction Coefficients of GTD and APO

F/D = 0.43 $D/\lambda = 15$

——— GTD results

– – – – APO results

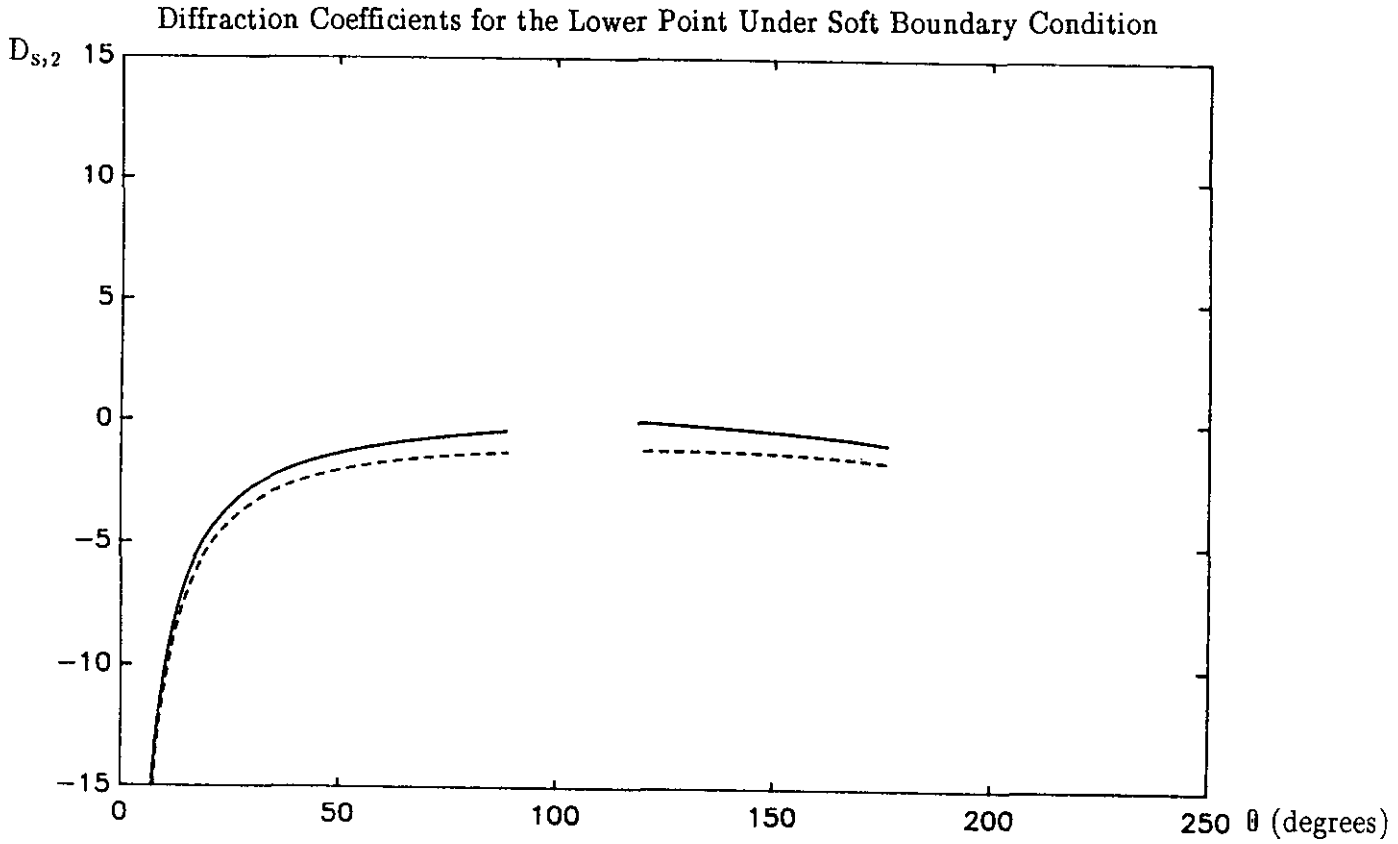

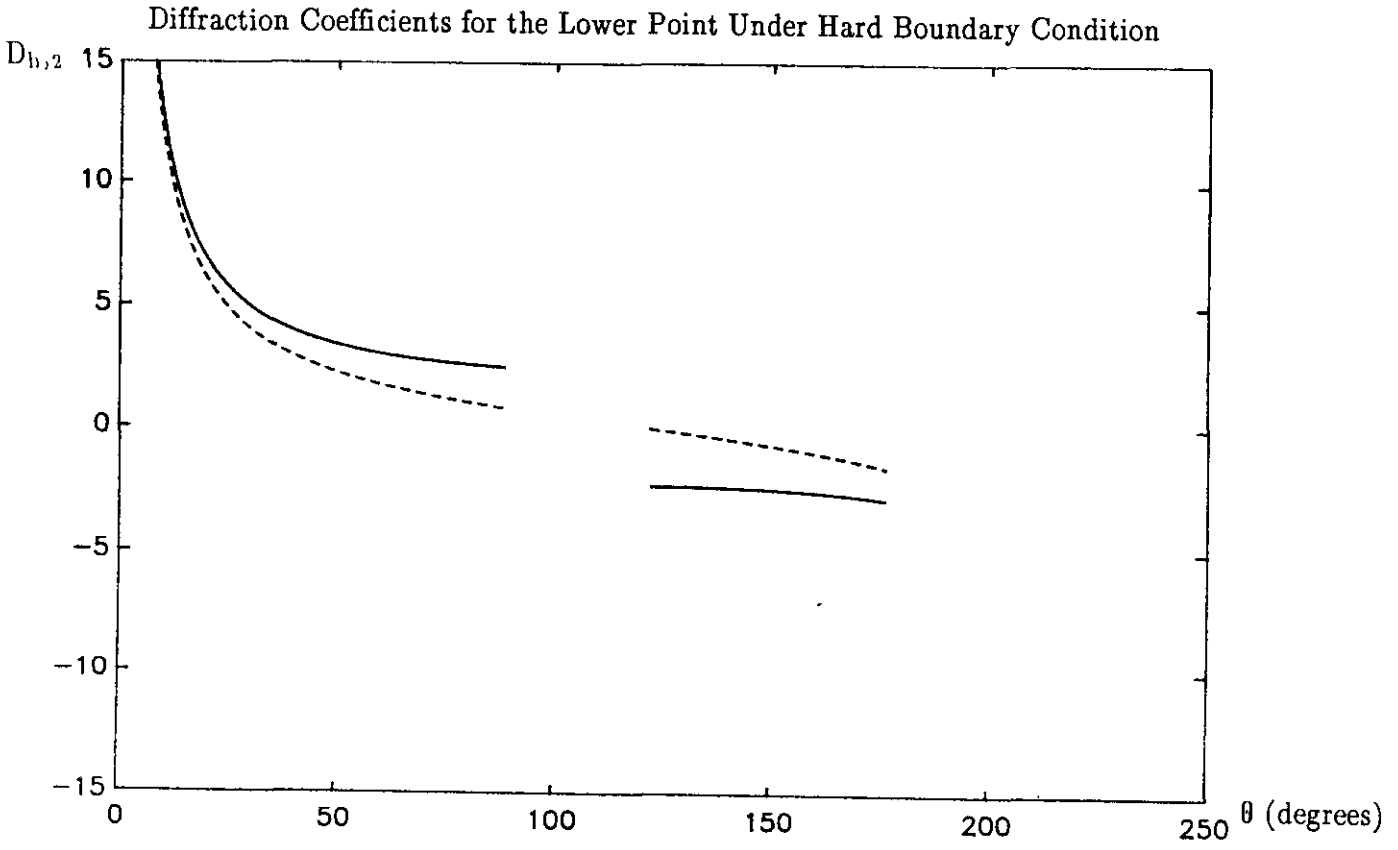

Fig. 7–2(b) Diffraction Coefficients of GTD and APO

F/D = 0.43 $D/\lambda = 15$

——— GTD results

– – – – APO results

Figs. 7–2(a) and 7–2(b) show that the diffraction coefficients of GTD and APO have the same trends and that there are discontinuities where $\theta=\alpha$ (at 120^0). In the figures, it can be seen that the differences between the diffraction coefficients become large in the shadow region.

7.3.2 Radiation Pattern Comparison of UTD and APO

Secondly, the radiation patterns with Kouyoumjian's UTD and Knop's APO were calculated. The results that were obtained from both methods are plotted in Figs. 7–3(a) and 7–3(b). It can be seen from Fig. 7–3 that, although the differences between the diffraction coefficients shown in Fig. 7–2 are called "second order" by Rusch [7], the difference between the resulting radiation patterns appears to be large.

7.3.3 Radiation Pattern Comparison of UTD and CAPO

From the study done by Knop and Ostertag [8], it was concluded that APO has to be replaced by CAPO. So, it is interesting to compare the results calculated by UTD with those from CAPO. As shown in Fig. 7–4, the diffraction coefficients of CAPO and GTD are numerically indistinguishable and consequently, the radiation patterns (see Fig.7–5(a) and Fig. 7–5(b)) are almost identical too. Since the CAPO results agree well with measurements [8], GTD (UTD) gives valid results too.

7.4 Transition Region Between EEC and GTD (UTD)

Because the GTD–method is invalid for the rear–axial region, EEC is used here. As mentioned in Chapter 6, the EEC–currents have been derived from the GTD diffraction coefficients. Although these currents are derived from GTD, the EEC method is able to provide correct fields in the rear–axial direction. This is due to the fact that EEC is not based on the contributions from two edge points, but on the integration of the contributions of the complete edge. The close relationship between EEC and GTD makes it very likely that a smooth transition between the two methods will be obtained. To see how close to the rear–axial direction the GTD results are still valid, the far–field in and near the rear–axial direction was calculated using both EEC and GTD. As an example Fig. 7–6 shows that the transition angle θ_{GE} between GTD and EEC results is about $\theta=5^0$ ($\vartheta=175^0$) for the E–plane pattern of an antenne system with a $D/\lambda=15$ and n=2.

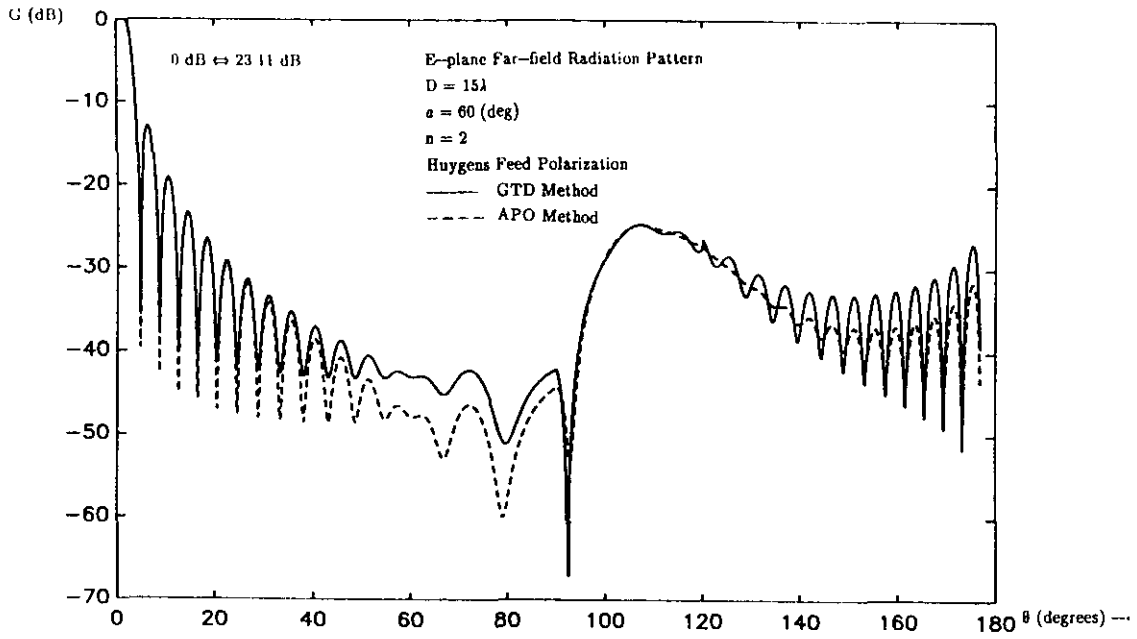

Fig. 7–3(a) E–plane Far–field Radiation Pattern of a Focus–fed Axially Symmetrical Paraboloid

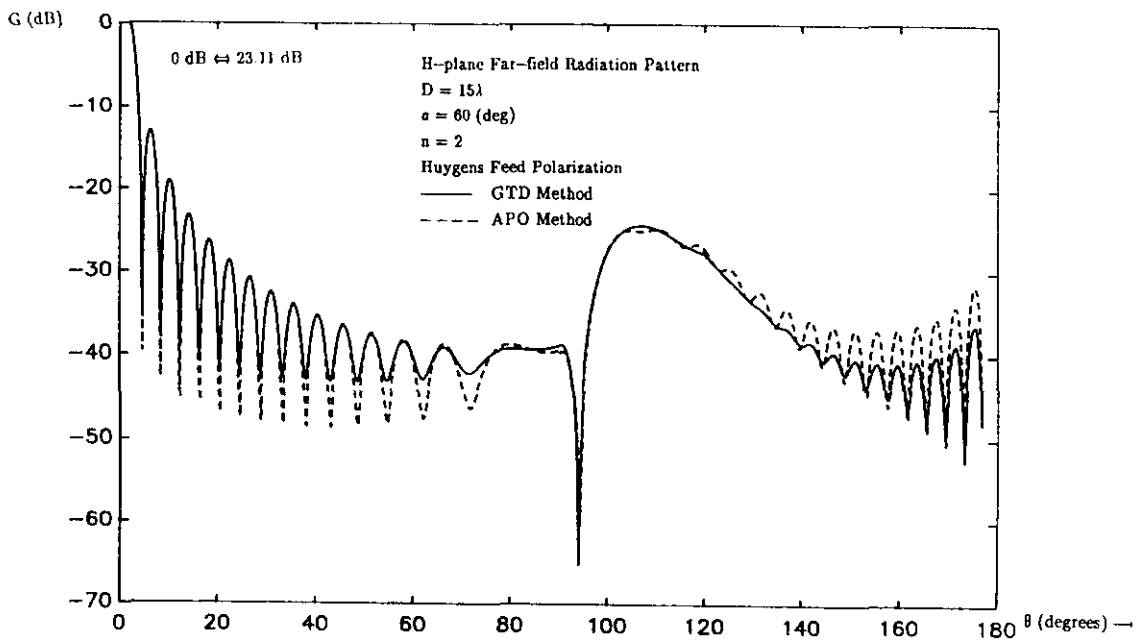

Fig. 7–3(b) H–plane Far–field Radiation Pattern of a Focus–fed Axially Symmetrical Paraboloid

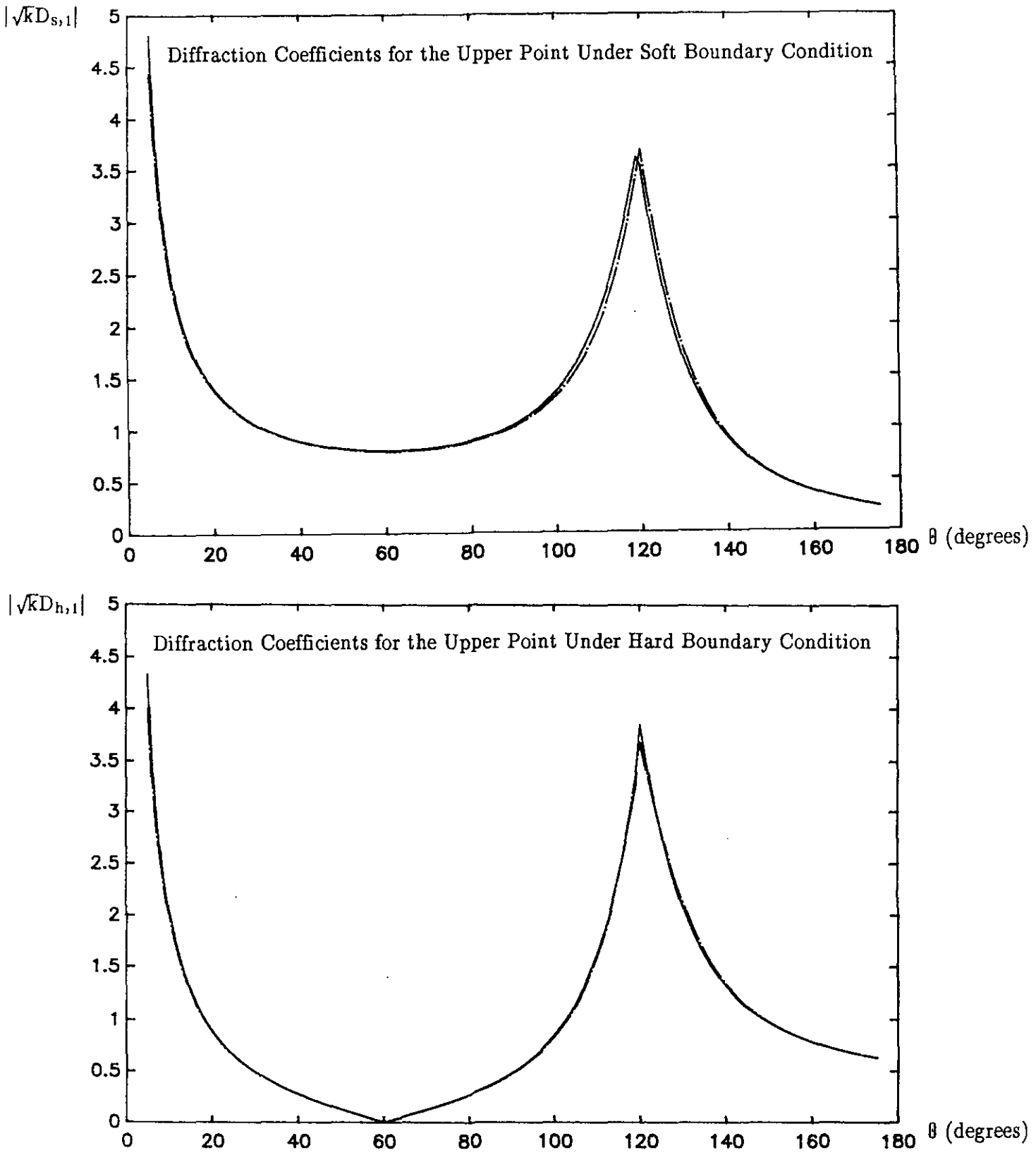

Fig. 7–4(a) Diffraction Coefficients of GTD and CAPO

F/D = 0.43 $D/\lambda = 15$

——— GTD results

–·–·– CAPO results

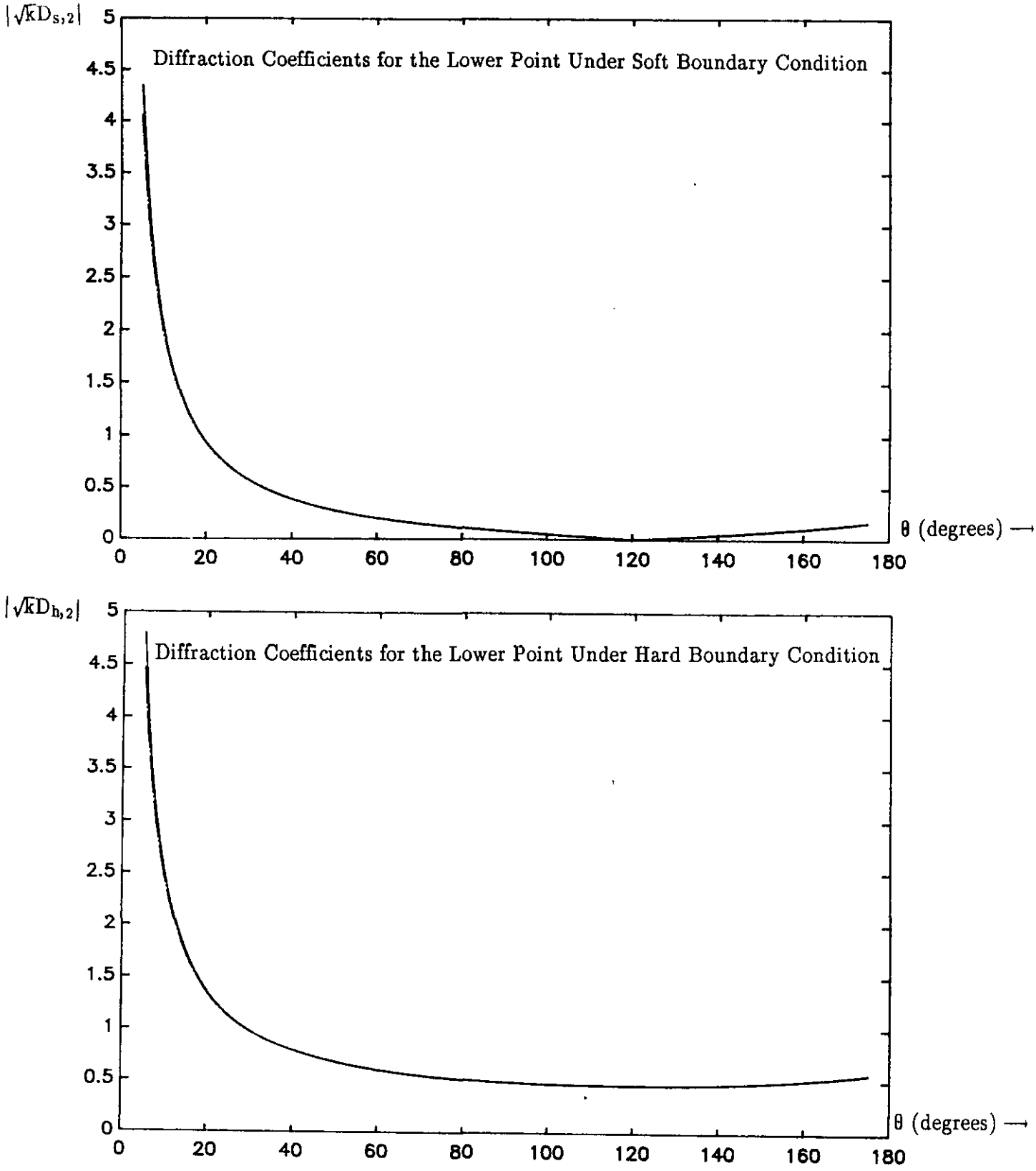

Fig. 7–4(b) Diffraction Coefficients of GTD and CAPO

$F/D = 0.43$ $D/\lambda = 15$

——— GTD results

—·—·— CAPO results

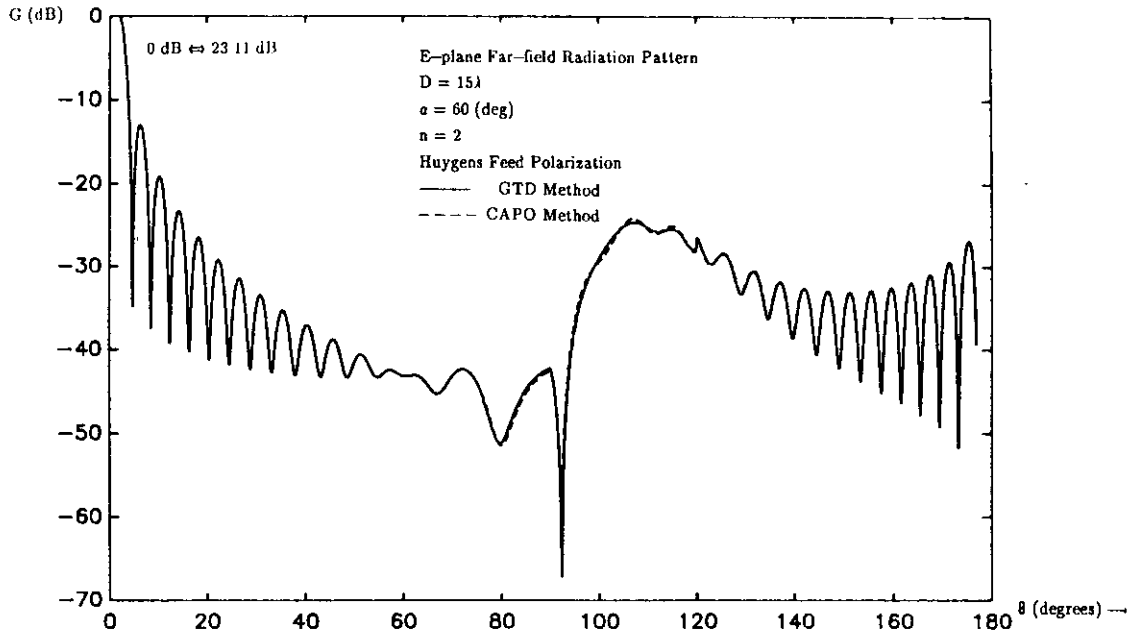

Fig. 7–5(a) E–plane Far–field Radiation Pattern of a Focus–fed Axially Symmetrical Paraboloid

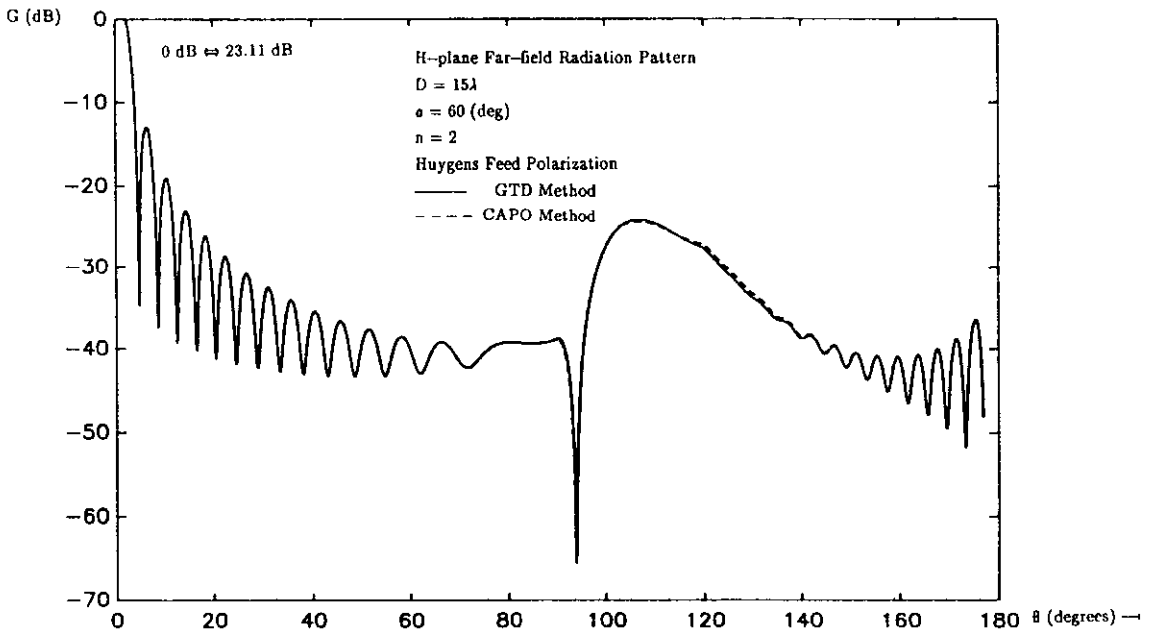

Fig. 7–5(b) H–plane Far–field Radiation Pattern of a Focus–fed Axially Symmetrical Paraboloid

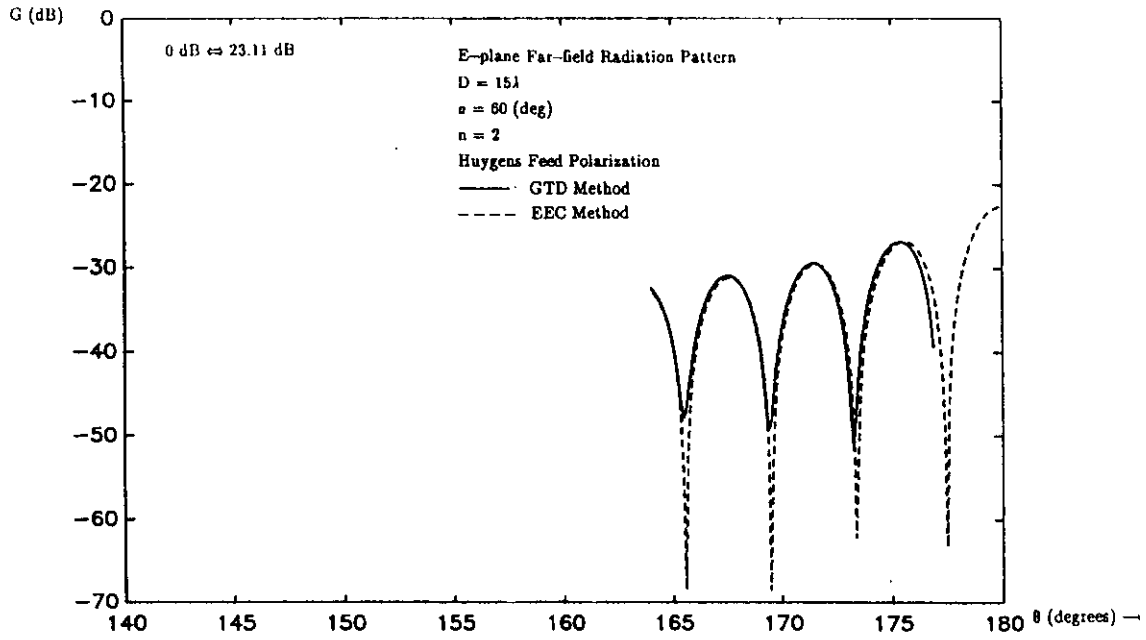

Fig. 7–6 E–plane Far–field Radiation Pattern in the Rear–axial Region of a Focus–fed Axially Symmetrical Paraboloid

The influence of the D/λ ratio on the transition angle θ_{GE} is shown in Fig. 7–7(a) and 7–7(b). As expected, the θ_{GE} is almost inversely proportional to D/λ. Fig. 7–8 shows that θ_{GE} does not depend on the value of n of the feed function. This is as expected because the GTD field (Eq.(4–42)) and the EEC field(Eq.(6–12)) have a common term $\sqrt{G_f(a)}$.

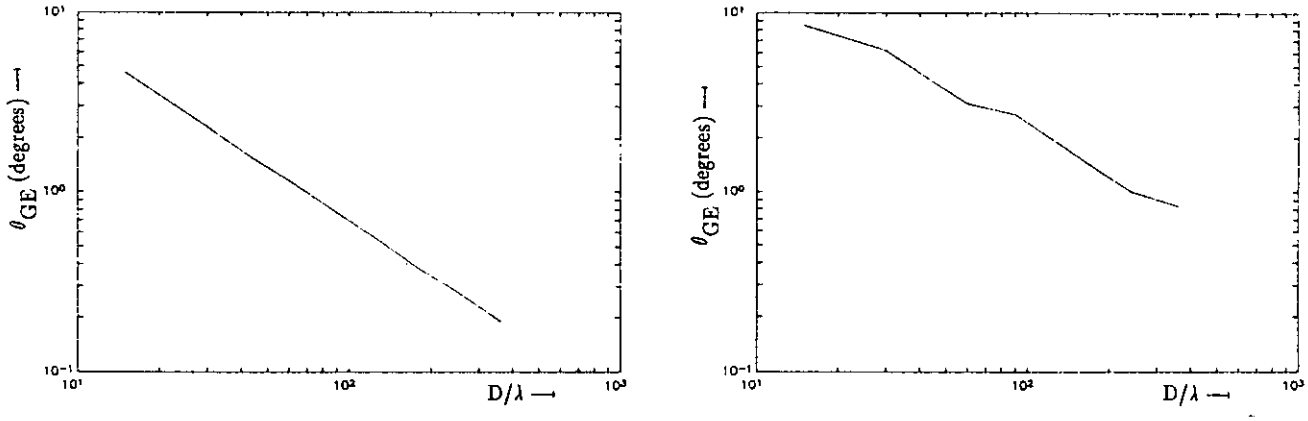

(a) (b)

Fig.7–7 The Transition angle θ_{GE} Between GTD and EEC as a Function of D/λ
(a) E–plane (b) H–plane

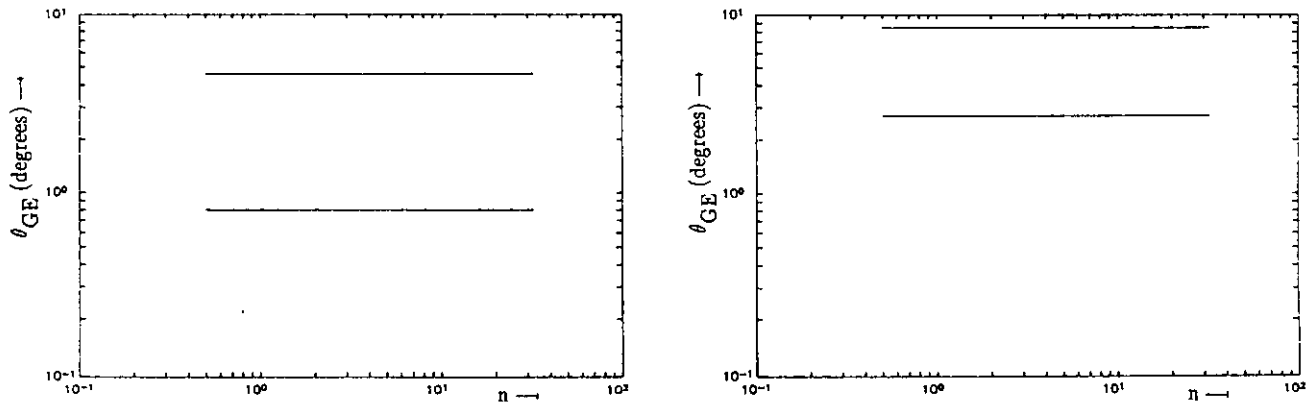

(a) (b)

Fig 7–8 The Transition angle θ_{GE} Between GTD and EEC as a Function of n
(a) E–plane (b) H–plane

7.5 Transition Region Between PO and GTD (UTD)

In the forward–axial region, GTD (UTD) is unsuitable because the forward–direction $\theta=\pi$ is another caustic of the paraboloidal reflector. However, PO is successfully used to determine the mainlobe and the first few side–lobes.

So, it is also interesting to compare the radiation patterns calculated with PO and GTD to see to which angle near to the forward–direction GTD method can still be used. As an example, Fig. 7–9 shows that the transition angle θ_{GP} is about $\vartheta=11^0$ ($\theta=169^0$) for the E–plane pattern of an antenna system with a $D/\lambda=15$ and $n=2$.

The influence of the D/λ ratio on the transition angle is shown in Fig. 7–10. As expected, the θ_{GP} is again inversely proportional to D/λ. The value of n of the feed function appeared to be neglectable.

Finally, by combining the modified GTD (UTD), the current–distribution method and the EEC method, a complete radiation pattern is obtained (see Fig. 7–11).

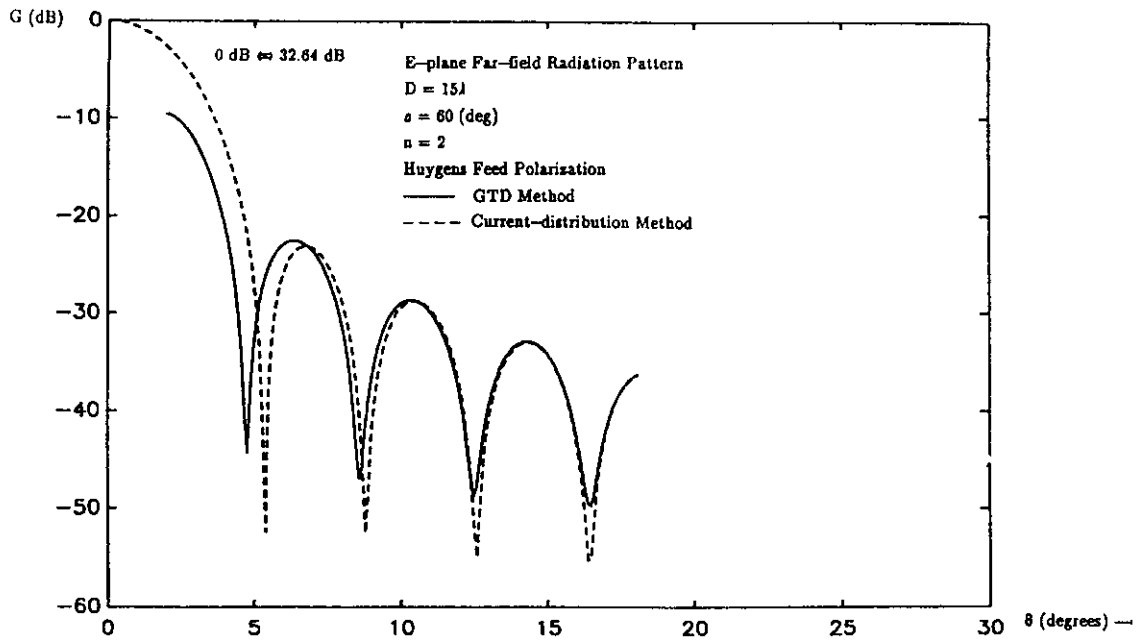

Fig. 7–9 Far–field Radiation Pattern in the Forward–Axial Region of a Focus–fed Axially Symmetrical Paraboloid

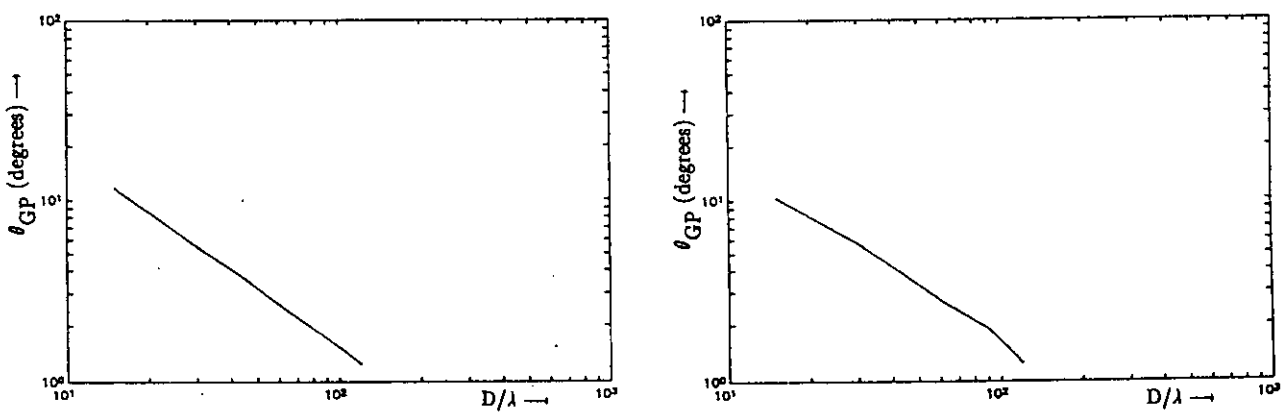

Fig. 7–10 The Transition angle θ_{GP} Between GTD and PO as a Function of D/λ (a) E–plane (b) H–plane

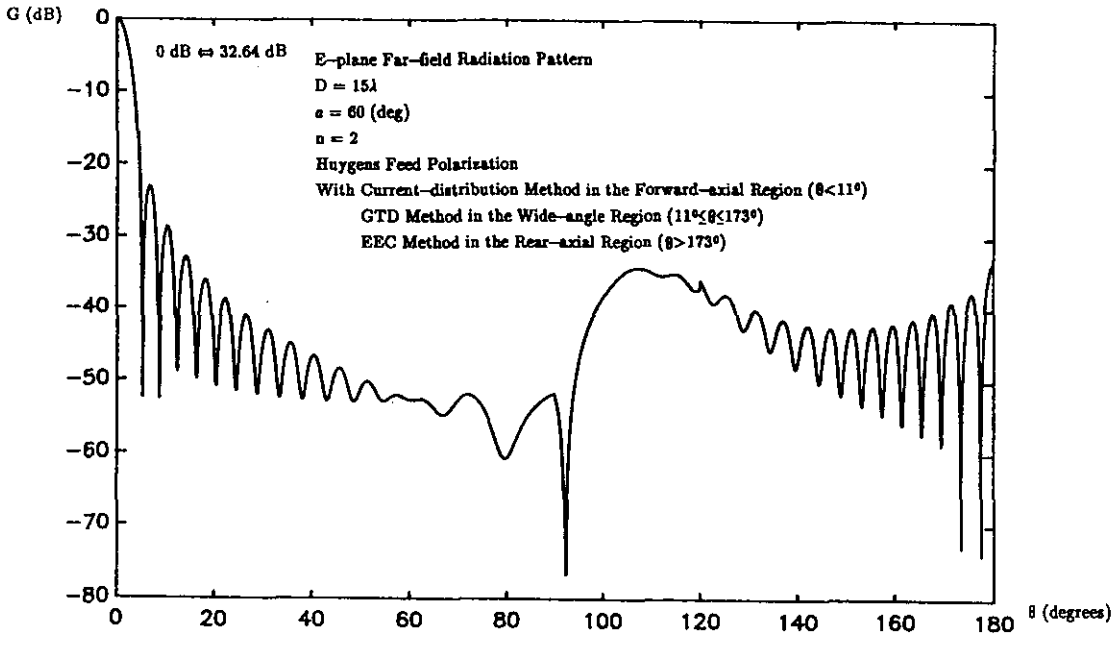

Fig. 7–11 Complete Far–field Radiation Pattern of a Focus–fed Axially Symmetrical Paraboloid

8. Offset Paraboloidal Reflector Antenna Configuration

8.1 Reflector Geometry

An offset parabolic reflector configuration is composed of a single–reflector and a feed at its focus, or two reflectors for which the main offset reflector is illuminated by the combination of a feed and a sub–reflector. In this report, an offset parabolic single reflector antenna is considered.

The geometry of the antenna is shown in Fig.8–1. The offset parabolic reflector is a portion of a paraboloid of revolution around the z–axis with a focal length of f.

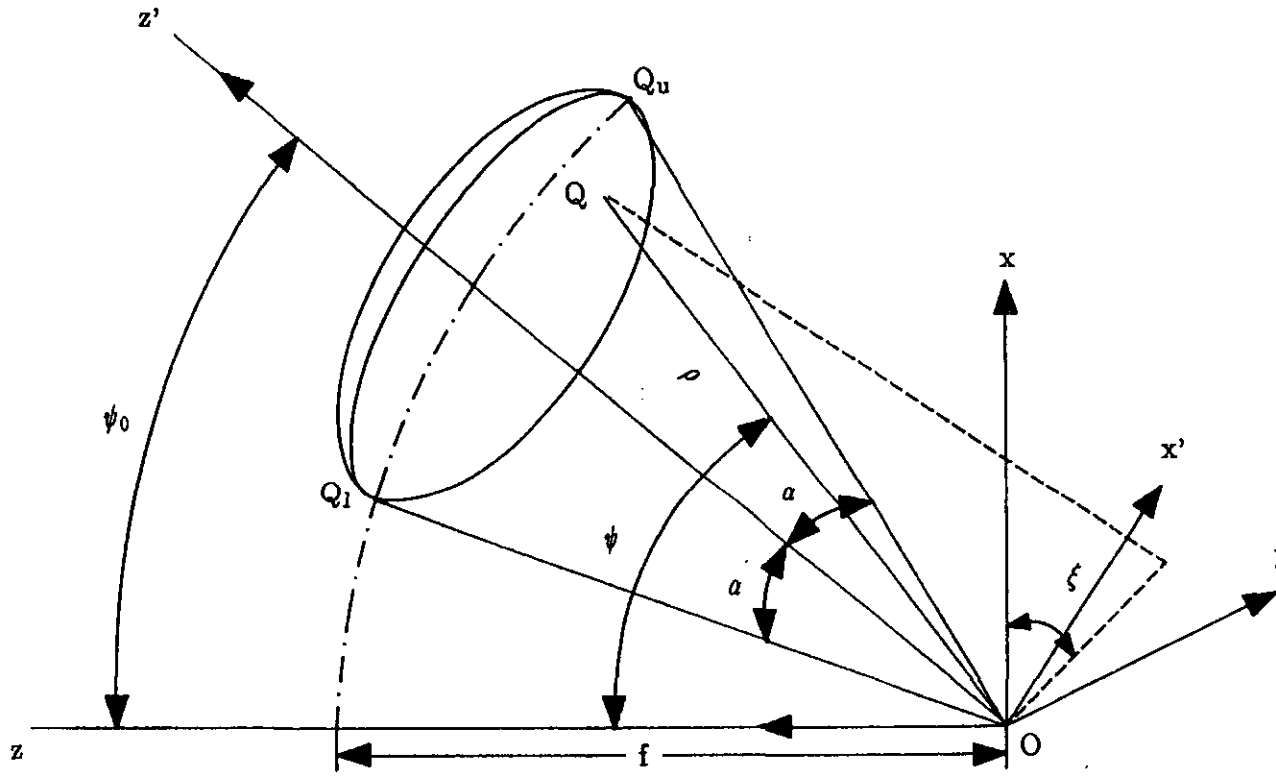

Fig. 8–1 The Geometry of an Offset Parabolic Single Reflector Antenna

The paraboloid is illuminated by a feed within a cone with half–subtended angle a measured from the z'–axis (the axis of the feed).

It can be shown that the projection of the edge of the reflector on the x–y plane (fig 8–2(a)) is a circle with diameter:

$$D = \frac{4f \sin\alpha}{(\cos\psi_0+\cos\alpha)} \qquad (8\text{–}1)$$

Furthermore it appears that the edge curve lies on a plane parallel to the y–axis, making an angle ψ_{p0} with the x–axis (fig. 8–2(b)):

$$\mathrm{tg}\psi_{p0} = \frac{\sin\psi_0}{\cos\alpha+\cos\psi_0}. \qquad (8\text{–}2)$$

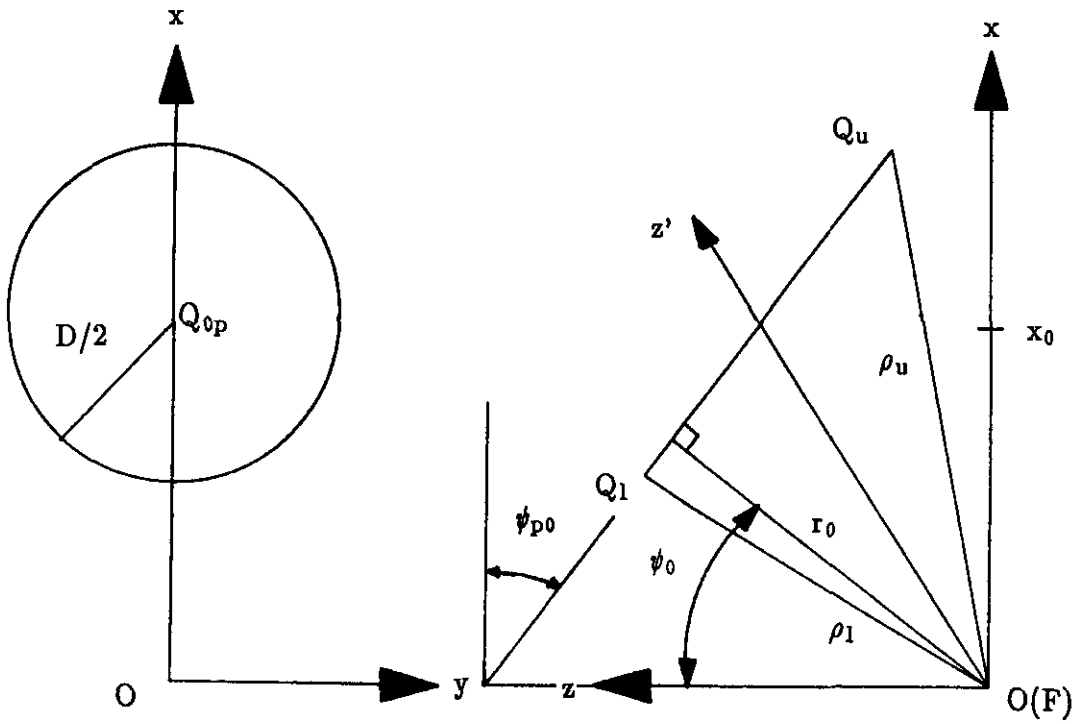

(a) The Projection on x–y Plane (b) The Projection on x–z Plane

Fig. 8–2 The Projection of the Edge Curve of the Offset Paraboloidal Reflector Aperture

8.2 Feed Radiation Properties

Since the feed axis differs from the symmetry axis of the paraboloid the prime (x',y',z') coordinate system has been introduced. The corresponding (ρ',ψ',ξ') sperical coordinate system is used to describe the vectorial radiation pattern of the feed. For the offset antenna, the same feed pattern will be used as for the symmetrical antenna previously.

Due to the asymmetric offset geometry, the radiation pattern of the complete antenna system for x'– and y'–polarization will be different. In the next chapters, most of the derivations are done for an x'–polarized feed. If y'–axis polarization is used, it will be stated.

9. Radiation Pattern Analysis by GTD (UTD) for an Offset Paraboloidal Reflector Antenna

9.1 Introduction

The angle region definition given in Chapter 3 for the symmetrical reflector antenna should be adapted according the offset reflector geometry shown in Fig. 8–1. This is trivial for the definition of the illuminated and shadow region. However, it will be shown that the caustic which is found for the symmetrical antenna in the rear–axial direction, now appears at another far–field observation angle. This will be dealt with in some detail in this second part of the report.

Another difference from the analysis of the symmetrical antenna is that the diffraction rays do not always hit the reflector edge perpendicular to its tangent. The oblique incidence makes an analysis much more complicated, this justifies the separate treatment of the application of GTD (UTD) to offset reflector antennas in this second part of the report.

9.2 GTD Diffraction Point Location for an Offset Configuration

It can be seen from the previous part of this report that GTD is based on the ray tracing technique. As shown in Eq.(4–2), the incident field at the point of diffraction (Q) must be known in order to obtain the diffracted field at the observation point (P). If the rays from a limited number of diffraction points contributing to the field at a certain point, or in a certain direction, are known the total field can be obtained by simply adding all the individual contributions together.

Therefore, the locations of the diffraction points have to be found. First, a coordinate transformation is introduced. The purpose of this transformation is to describe the field in a (x''',y''',z''') coordinate system, with its origin at a edge diffraction point and the x'''–axis being the tangent vector $(\vec{T})$ at the edge diffraction point. The advantage of using such a transformation is that the phenomena related to the diffraction can be described easily (e.g. the description of the diffraction cone).

9.2.1 Coordinate Transformation

Since the new coordinate system that has to be introduced is determined by the position of the diffraction point and the edge tangent of the reflector at the diffraction point, it is a diffraction–point–fixed coordinate system.

From the previous edge curve equation, the unit vector $\vec{T}$ tangent of the edge curve at any edge point was derived in [26] as:

$$\vec{T} = T_x \vec{x} + T_y \vec{y} + T_z \vec{z} \qquad (9\text{–}1)$$

with $$T_x = \frac{-\sin\xi'(\cos\psi_0+\cos\alpha)}{T_s} \qquad (9\text{–}1,a)$$

$$T_y = \frac{\cos\psi_0\cos\alpha\cos\xi'+\cos\xi'-\sin\psi_0\sin\alpha}{T_s} \qquad (9\text{–}1,b)$$

$$T_z = \frac{\sin\xi'\sin\psi_0}{T_s} \qquad (9\text{–}1,c)$$

$$T_s=\sqrt{[-\sin\xi'(\cos\psi_0+\cos\alpha)]^2+[\cos\psi_0\cos\alpha\cos\xi'+\cos\xi'-\sin\psi_0\sin\alpha]^2+[\sin\xi'\sin\psi_0]^2} \qquad (9\text{–}1,d)$$

This coordinate transformation is similar to the one presented in [24], although it involves a different angle rotation direction and angular rotation sequence (see Fig. 9–1). Since the displacement of the origin will not change the expressions for the unit vectors, the same (x,y,z) notation is used for the coordinates after moving the origin to the edge diffraction point.

Introducing of the new coordinate system starts by rotating the y–axis through an angle α' around the x–axis, which puts it in the new direction y_1, determined by the intersection of the plane normal to the edge tangent at the edge point with the y–z plane (see Fig. 9–1(a)):

$$\mathrm{tg}\alpha' = -\frac{T_Y}{T_z} = -\frac{\cos\psi_0\cos\alpha\cos\xi'+\cos\xi'-\sin\psi_0\sin\alpha}{\sin\xi'\sin\psi_0}, \qquad (9\text{–}2)$$

after the first rotation, the (x_t,y_t,z_t) coordinate system is obtained, it has the following relation with (x,y,z) coordinate system:

$$\begin{bmatrix} x \\ y \\ z \end{bmatrix} = \begin{bmatrix} 1 & 0 & 0 \\ 0 & \cos\alpha' & -\sin\alpha' \\ 0 & \sin\alpha' & \cos\alpha' \end{bmatrix} \begin{bmatrix} x_t \\ y_t \\ z_t \end{bmatrix}. \tag{9–3}$$

The subscript t has been used to emphasize the transformations used.

Then, the x_t–axis is rotated through an angle β around the y_t–axis, which puts it in the direction of $\vec{T}$. The angle β between the x–axis and $\vec{T}$ is then given by:

$$\cos\beta = \vec{T} \cdot \vec{x} = T_x = -\frac{\sin\xi'(\cos\psi_0+\cos\alpha)}{T_s} \tag{9–4}$$

After the second anglular rotation, the (x_t',y_t',z_t') coordinate system is obtained (see Fig.9–1(b)). The relation between the (x_t',y_t',z_t') and the (x_t,y_t,z_t) coordinate systems is:

$$\begin{bmatrix} x_t \\ y_t \\ z_t \end{bmatrix} = \begin{bmatrix} \cos\beta & 0 & \sin\beta \\ 0 & 1 & 0 \\ -\sin\beta & 0 & \cos\beta \end{bmatrix} \begin{bmatrix} x_t' \\ y_t' \\ z_t' \end{bmatrix}. \tag{9–5}$$

Finally, the y_t'–axis is rotated by an angle γ around the x_t'–axis, this puts it in the incident plane (containing $\vec{T}$ and $\vec{\rho}$). The angular rotation makes the x_t''–y_t'' plane into the incident plane which facilitates the field calculation later on.
The angle γ is given by:

$$\sin\gamma = \vec{N}_s \cdot \vec{y}_t' \tag{9–6}$$

where the $\vec{N}_s$ is the unit vector normal to the plane containing the $\vec{T}$ and $\vec{\rho}$ vectors, given by:

$$\vec{N}_s = \det\begin{bmatrix} T_y & T_z \\ \rho_y & \rho_z \end{bmatrix}\vec{x} + \det\begin{bmatrix} T_z & T_x \\ \rho_z & \rho_x \end{bmatrix}\vec{y} + \det\begin{bmatrix} T_x & T_y \\ \rho_x & \rho_y \end{bmatrix}\vec{z} \tag{9–7}$$

and

$$\vec{y}\ell' = \cos\alpha\,\vec{y} + \sin\alpha\,\vec{z}, \tag{9–8}$$

So, the new $(x\ell'',y\ell'',z\ell'')$ coordinate system is related to the former $(x\ell',y\ell',z\ell')$ coordinate system (see Fig. 9–1(c)) as given by:

$$\begin{bmatrix} x\ell' \\ y\ell' \\ z\ell' \end{bmatrix} = \begin{bmatrix} 1 & 0 & 0 \\ 0 & \cos\gamma & -\sin\gamma \\ 0 & \sin\gamma & \cos\gamma \end{bmatrix} \begin{bmatrix} x\ell'' \\ y\ell'' \\ z\ell'' \end{bmatrix}. \tag{9–9}$$

For the sake of convenience, the notation $[x''',y''',z''']^T$ is used instead of $[x\ell'',y\ell'',z\ell'']^T$ and the relation between the (x,y,z) and (x''',y''',z''') coordinate system can then be expressed by a transformation matrix M as:

$$\begin{bmatrix} x \\ y \\ z \end{bmatrix} = M \begin{bmatrix} x''' \\ y''' \\ z''' \end{bmatrix} \tag{9–10}$$

with

$$M = \begin{bmatrix} 1 & 0 & 0 \\ 0 & \cos\alpha & -\sin\alpha' \\ 0 & \sin\alpha & \cos\alpha' \end{bmatrix} \begin{bmatrix} \cos\beta & 0 & \sin\beta \\ 0 & 1 & 0 \\ -\sin\beta & 0 & \cos\beta \end{bmatrix} \begin{bmatrix} 1 & 0 & 0 \\ 0 & \cos\gamma & -\sin\gamma \\ 0 & \sin\gamma & \cos\gamma \end{bmatrix}$$

$$= \begin{bmatrix} \cos\beta & \sin\beta\sin\gamma & \sin\beta\cos\gamma \\ \sin\alpha'\sin\beta & \cos\alpha'\cos\gamma - \sin\alpha'\cos\beta\sin\gamma & -\cos\alpha'\sin\gamma - \sin\alpha'\cos\beta\cos\gamma \\ -\cos\alpha'\sin\beta & \sin\alpha'\cos\gamma + \cos\alpha'\cos\beta\sin\gamma & -\sin\alpha'\sin\gamma + \cos\alpha'\cos\beta\cos\gamma \end{bmatrix} \tag{9–11}$$

The matrix M has the orthogonality property:

$$M^{-1} = M^T \tag{9–12}$$

so,

$$\begin{bmatrix} x''' \\ y''' \\ z''' \end{bmatrix} = M^{-1} \begin{bmatrix} x \\ y \\ z \end{bmatrix} \tag{9–13}$$

and

$$M^{-1} = \begin{bmatrix} \cos\beta & \sin\alpha'\sin\beta & -\cos\alpha'\sin\beta \\ \sin\beta\sin\gamma & \cos\alpha'\cos\gamma - \sin\alpha'\cos\beta\sin\gamma & \sin\alpha'\cos\gamma + \cos\alpha'\cos\beta\sin\gamma \\ \sin\beta\cos\gamma & -\cos\alpha'\sin\gamma - \sin\alpha'\cos\beta\cos\gamma & -\sin\alpha'\sin\gamma + \cos\alpha'\cos\beta\cos\gamma \end{bmatrix} \tag{9–14}$$

With the new (x''',y''',z''') coordinate system, the edge diffraction cone can be described easily, as will be shown in the next paragraph.

9.2.2 Diffraction Cone Formed at the Edge Diffraction Points

The incident ray vector from the feed to the reflector edge can be expressed by the radius unit vector in feed coordinate system:

$$\vec{\rho}' = \sin\alpha\cos\xi'\,\vec{x}' + \sin\alpha\sin\xi'\,\vec{y}' + \cos\alpha\,\vec{z}' \tag{9–15,a}$$

or

$$\vec{\rho}' = \begin{bmatrix} \sin\alpha\cos\xi'\,\vec{x}' \\ \sin\alpha\sin\xi'\,\vec{y}' \\ \cos\alpha\quad\ \vec{z}' \end{bmatrix} = \begin{bmatrix} \rho_x,\,\vec{x}' \\ \rho_y,\,\vec{y}' \\ \rho_z,\,\vec{z}' \end{bmatrix} \tag{9–15,b}$$

then by using the transform matrix similar to Eq.(9–5) for the relation between the (x,y,z) and (x',y',z') coordinate system, the $\vec{\rho}'$ in Eq.(9–15) can be expressed in the (x,y,z) reflector coordinate system:

$$\vec{\rho} = \begin{bmatrix} \sin\alpha\cos\psi_0\cos\xi' + \cos\alpha\sin\psi_0\ \vec{x} \\ \sin\alpha\,\sin\xi'\qquad\qquad\ \vec{y} \\ \cos\alpha\cos\psi_0 - \sin\alpha\sin\psi_0\cos\xi'\ \vec{z} \end{bmatrix} = \begin{bmatrix} \rho_x\,\vec{x} \\ \rho_y\,\vec{y} \\ \rho_z\,\vec{z} \end{bmatrix} \tag{9–16}$$

The angle β_0 between the incident ray vector $\vec{\rho}$ and the edge tangent $\vec{T}$ can

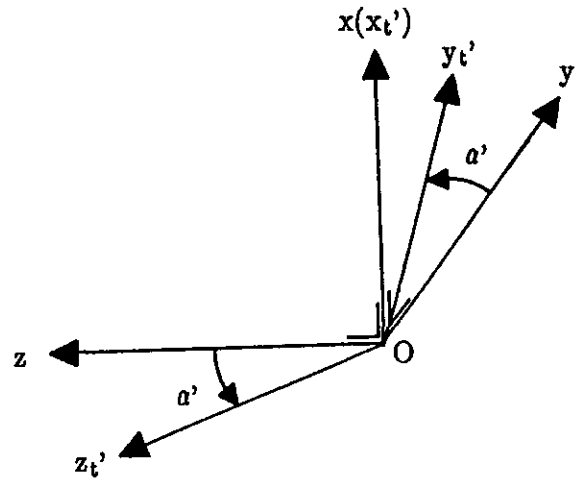

(a) First Rotation by an Angle a'

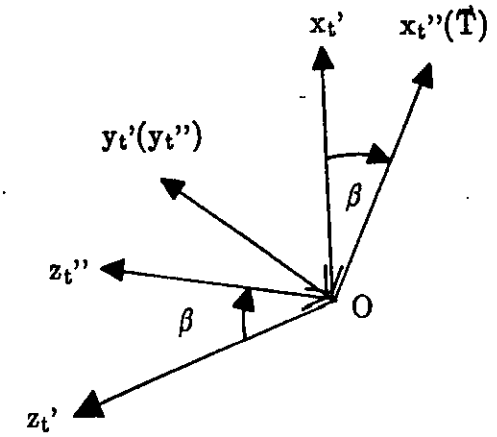

(b) Second Rotation by an Angle β

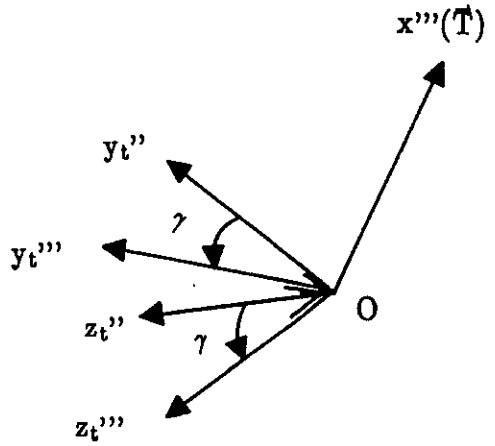

(c) Third Rotation by an Angle γ

Fig. 9–1 Coordinate Transformations

be derived from the dot product of the two unit vectors:

$$\cos\beta_0 = \vec{T}\cdot\vec{\rho} = -\frac{\sin\psi_0 \cdot \sin\xi'}{T_s} \qquad (9\text{–}17)$$

Now the diffraction cone, formed by diffracted rays from the diffraction point at the reflector edge having an half open angle β_0 around the tangent $\vec{T}$ (that is the x'''–axis), can simply be written in (x''',y''',z''') coordinates as:

$$(y''')^2 + (z''')^2 = tg^2\beta_0\,(x''')^2 \qquad (9\text{–}18)$$

The cone formed by the diffraction rays at the edge diffraction point is shown in Fig. 9–2.

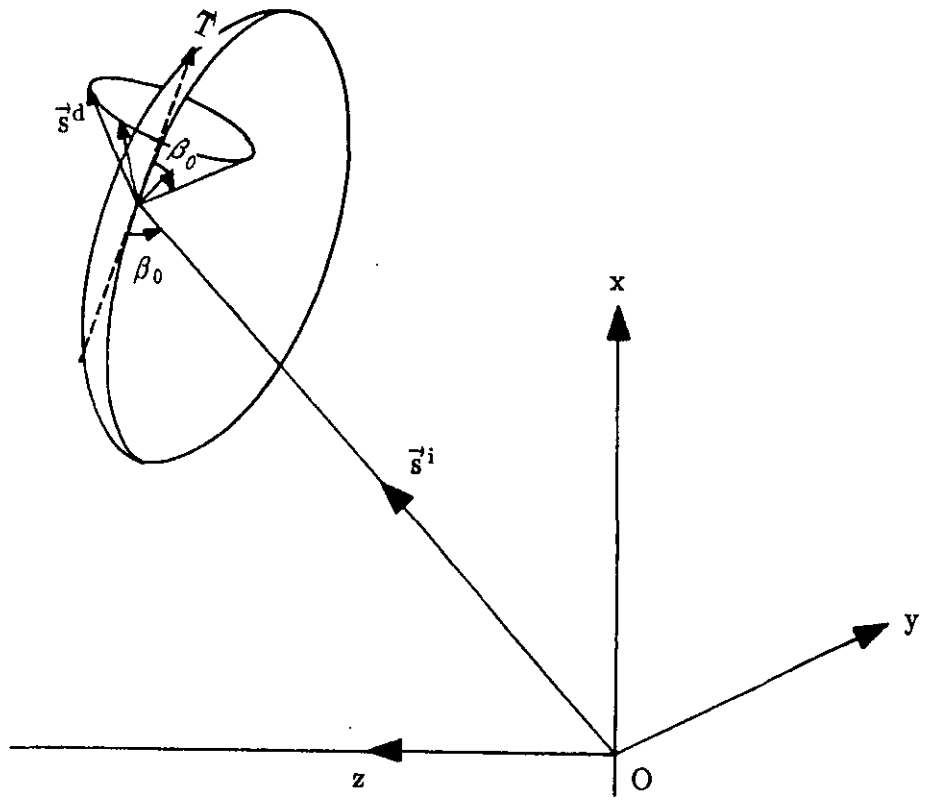

Fig. 9–2 The Diffracted Rays from the Edge Point of an Offset Reflector

So, by using the transformation matrix given in Eq.(9–14) and inserting it in Eq.(9–18), the radiation cone in the reflector (x,y,z) coordinates is obtained. This will be used in the next paragraph to find the diffraction points and rays contributing to the far–field of an offset reflector antenna.

9.2.3 Diffraction Point Location

In the following paragraphs, the location of the diffraction points, which contribute to the far–field, have been determined. The diffraction points for different radiation planes will be dealt with separately. As already mentioned in Chapter 8, x'– and y'–axis polarization are considered. These two polarizations will give different radiation patterns for the principal planes. Therefore it is sometimes more convenient to speak of the symmetry–plane (x'–z'–plane) and the asymmetry–plane (y'–z'–plane) for an offset configuration. In the following sections an x'–polarized feed is assumed. So, the symmetry plane is the E–plane and the H–plane is the asymmetry–plane. However, if an y'–polarized feed is considered this will be emphasized.

9.2.3.1 Diffraction Points for the E–plane Pattern Calculation

For the E–plane radiation pattern calculation, only the rays in a plane with y=constant must be taken into account. In the calculation of the diffraction point locations, y is taken to be equal to zero, because the origin is moved to the diffraction point. Taking the intersection of the diffraction cone (Eq. (9–18)) with the y=0 plane results in the following equation [26]:

$$(\cos^2\beta_0-\cos^2\beta)x^2+2\cos\beta\sin\beta\cos\alpha' xz=0 \qquad (9\text{–}19)$$

From Eq. (9–19) it is easy to see that the rays contributing to the E–plane have to satisfy:

$$\begin{cases} x=0 \\ y=0 \end{cases} \qquad (9\text{–}20,a)$$

or

$$\begin{cases} (\cos^2\beta_0-\cos^2\beta)x+2\cos\beta\sin\beta\cos\alpha' z=0 \\ y=0 \end{cases}, \qquad (9\text{–}20,b)$$

Inserting Eq.(9–2), Eq.(9–4) and Eq.(9–17) in Eq.(9–20,b) results in:

$$\begin{cases} \{[(\cos\psi_0+\cos\alpha)^2-\sin^2\psi_0]x-2(\cos\psi_0+\cos\alpha)\sin\psi_0 z\}\sin^2\xi'=0 \\ y=0 \end{cases}, \qquad (9\text{–}21)$$

where ξ' is defined at the x',y',z' coordinate system with the feed as origin. The solutions to this equation are:

$$\begin{cases} \sin^2\xi'=0 \\ y=0 \end{cases} \qquad (9\text{–}22,a)$$

or

$$\begin{cases} [(\cos\psi_0+\cos\alpha)^2-\sin^2\psi_0]x-2(\cos\psi_0+\cos\alpha)\sin\psi_0 z = 0 \\ y=0 \end{cases}. \qquad (9\text{–}22,b)$$

Because Eq.(9–20,a), Eq.(9–22,a) and Eq.(9–22,b) are mathematical solutions to the problem, it is still necessary to see which can be obtained in practice. Eq.(9–20,a) represents two directions, one in the +z–axis direction (θ=0) and the other in the antenna forward–direction ($\theta=\pi$). The reason that the direction θ = 0 is found mathematically is that a symmetrical image diffraction cone exists, due to the quadratic form of Eq.(9–18) (see Fig. 9–3).

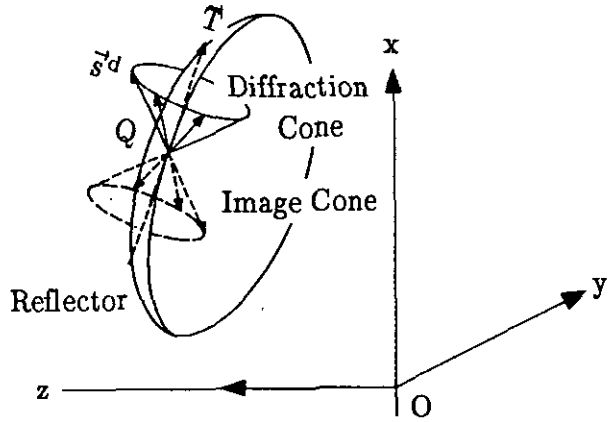

Fig. 9–3 The Existence of an Image Diffraction Cone.

The rays given by Eq.(9–22,a) contribute to all angles in the E–plane because of the θ–angle independency. Since $\xi'=0,\ \pi$ are the solutions to Eq.(9–22,a), the corresponding diffraction points at the edge of the reflector are the upper point Q_u and the lower point Q_l.

If $(\cos\psi_0+\cos\alpha)^2-\sin^2\psi_0\neq 0$ then, the rays given by Eq.(9–22,b) will contribute to a specific θ–angle direction with z–axis. This angle can be written as:

$$\mathrm{tg}\theta=\frac{x}{z}=\frac{2(\cos\alpha+\cos\psi_0)\sin\psi_0}{(\cos\psi_0+\cos\alpha)^2-\sin^2\psi_0} \tag{9–23}$$

which can be rewritten as:

$$\mathrm{tg}\theta=\frac{\dfrac{2\sin\psi_0}{\cos\alpha+\cos\psi_0}}{1-\dfrac{\sin^2\psi_0}{(\cos\psi_0+\cos\alpha)^2}}$$

$$=\frac{2\mathrm{tg}\psi_{p0}}{1-\mathrm{tg}^2\psi_{p0}} \tag{9–24}$$

with the solution:

$$\theta=\begin{cases}2\psi_{p0}\\ \pi+2\psi_{p0}\end{cases} \tag{9–25}$$

where $\theta=2\psi_{p0}$ is the only true solution, because $\theta=\pi+2\psi_{p0}$ originates from the unphysical image of the diffraction cone. The solution is ξ'–angle independent, so the whole edge will contribute in this specific θ–direction.

9.2.3.2 Diffraction Points for the H–plane Pattern Calculation

For the H–plane (x=0, for an x'–polarized feed), a similar equation is found:

$$(\cos^2\beta_0-\sin^2\beta\sin^2\alpha')y^2+2\sin^2\beta\sin\alpha'\cos\alpha'yz=0, \tag{9–26}$$

From this formula the following equations are found, to which the rays contributing to the H–plane pattern have to satisfy:

$$\begin{cases} x=0 \\ y=0 \end{cases} \qquad (9\text{–}27,a)$$

or

$$\begin{cases} (\cos^2\beta_0-\sin^2\beta\sin^2\alpha')y+2\sin^2\beta\sin\alpha'\cos\alpha'z=0 \\ x=0 \end{cases}, \qquad (9\text{–}27,b)$$

Inserting Eq.(9–2), Eq.(9–4) and Eq.(9–17) in Eq.(9–27,b) results in:

$$\begin{cases} [(\cos\psi_0\cos\alpha\cos\xi'+\cos\xi'-\sin\alpha\sin\psi_0)^2-\sin^2\xi'\sin^2\psi_0]y \\ \qquad +2(\cos\psi_0\cos\alpha\cos\xi'+\cos\xi'-\sin\alpha\sin\psi_0)\sin\xi'\sin\psi_0 z=0 \\ x=0 \end{cases}, \qquad (9\text{–}28)$$

If $(\cos\psi_0\cos\alpha\cos\xi'+\cos\xi'-\sin\psi_0\sin\alpha)^2-\sin^2\xi'\sin^2\psi_0\neq 0$, Eq. (9–28) determines the ray which is in the y–z plane having an angle θ with the z–axis:

$$\tan\theta = \frac{y}{z} = -\frac{2(\cos\psi_0\cos\alpha\cos\xi'+\cos\xi'-\sin\alpha\sin\psi_0)\cdot\sin\xi'\sin\psi_0}{(\cos\psi_0\cos\alpha\cos\xi'+\cos\xi'-\sin\alpha\sin\psi_0)^2-\sin^2\xi'\sin^2\psi_0} \qquad (9\text{–}29)$$

It is clear that Eq.(9–27,a) represents the direction $\theta=\pi$, and that Eq.(9–29) gives the diffracted rays which contribute to an angle direction θ.

Fig. (9–4,a) shows the relation between the far–field angle θ and the edge points of diffraction defined by the angle ξ' for the H–plane pattern calculation, as given by Eq.(9–29). Here, $\theta<180$ indicates the half plane where $\phi=\pi/2$ and $\theta>180$ indicates the other half plane where $\phi=3\pi/2$.

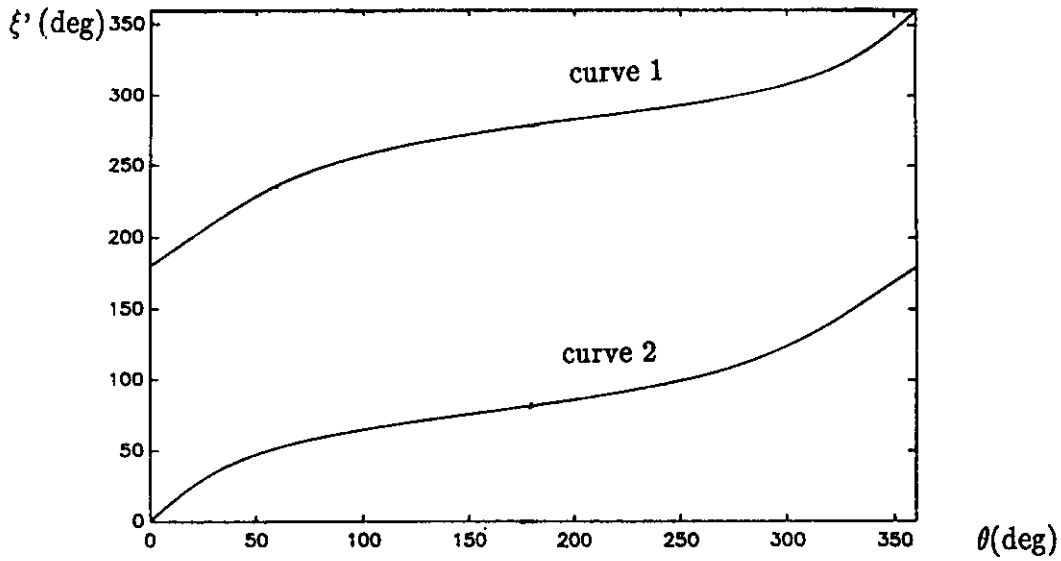

Fig. 9–4(a) The Edge Diffraction Point Angle ξ' as a Function of the Far–field Observation Angle θ for H–plane Pattern Calculation

9.2.3.3 Diffraction Points for an Arbitrary Plane

For the calculation of the radiation patterns in any plane other than the symmetry plane (E–plane for x'–axis polarization,ϕ=0) and the asymmetry plane (H–plane for x'–axis polarization, $\phi=\pi/2$), a similar procedure can be followed. The diffraction cones have to be cut by the corresponding ϕ–plane.

The same steps as for the E– and H–plane calculation can be followed so that the next equation is obtained:

$$\begin{cases} \theta=\pi \\ \\ \mathrm{tg}\,\theta= \end{cases}$$

$$-2\{[(\cos\psi_0\cos\alpha\cos\xi'+\cos\xi'-\sin\psi_0\sin\alpha]\sin\phi-[\sin\xi'(\cos\psi_0+\cos\alpha)]\cos\phi\}\sin\xi'\sin\psi_0$$
$$[(\cos\psi_0\cos\alpha\cos\xi'+\cos\xi'-\sin\psi_0\sin\alpha)\sin\phi-(\cos\psi_0+\cos\alpha)\sin\xi'\cos\phi]^2-\sin^2\psi_0\sin^2\xi'$$

(9–30)

For the radiation pattern in the plane $\phi=\pi/3$, the relation between the far–field observation point and the location of the edge diffraction points involved in the pattern calculation is shown in Fig. 9–4(b).

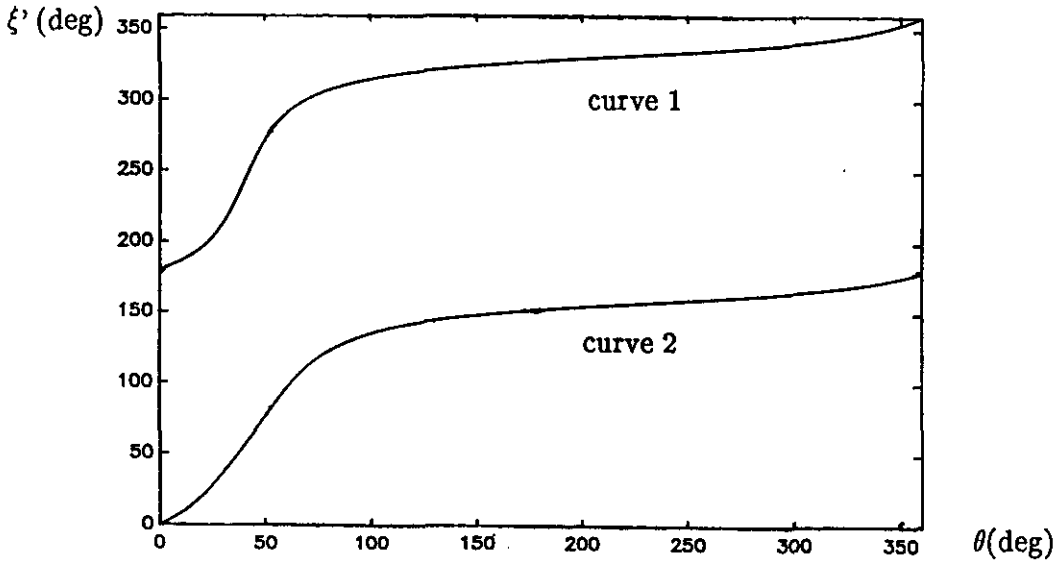

Fig. 9–4(b) The Edge Diffraction Point Angle ξ' as a Function of the Far–field Observation Angle θ for $\phi=\pi/3$

9.2.3.4 Stationary Phase Method (APO)

In [15], the radiation pattern of an offset antenna has been calculated from Asymptotic Physical Optics (APO). As shown in the first part of this report, the locations of the APO stationairy phase points coincide with those of the GTD diffraction points for the symmetrical antenna configuration. In order to check the results obtained in the previous section, it is interesting to compare the locations of the diffraction points with those for the stationairy phase points, in case of an offset configuration.

According to the stationary phase method, the stationary phase points of second kind [15] satisfy:

$$\frac{\partial \Phi}{\partial \xi'}\frac{\partial \Psi}{\partial \rho'} - \frac{\partial \Phi}{\partial \rho'}\frac{\partial \Psi}{\partial \xi'} = 0 \tag{9–31}$$

with

$$\Phi = k(\rho - \rho\vec{\rho}\cdot\vec{r}) = k\rho(1-\vec{\rho}\cdot\vec{r}) \tag{9–32,a}$$

$$\Psi = \rho(1+\cos\psi) - 2f \tag{9–32,b}$$

where Φ and Ψ are the phase function and the reflector edge equation, respectively, $\vec{\rho}$ is the unit vector in the direction from the feed to the edge of the reflector and $\vec{r}$ is the unit vector in the direction from the feed to the far–field observation point.

For the configuration described previously, the unit vector $\vec{r}$ can be expressed as:

$$\vec{r} = \begin{Bmatrix} \sin\theta\cos\phi\ \vec{x} \\ \sin\theta\sin\phi\ \vec{y} \\ \cos\theta\ \vec{z} \end{Bmatrix} \tag{9–33}$$

Since the objective is to find the location of the stationary phase points, it is convenient to use the feed coordinate system. In such a system, the edge of the reflector can shown easily.

The unit vector $\vec{\rho}$ can be written as:

$$\vec{\rho} = \begin{Bmatrix} \sin\psi'\cos\psi_0\cos\xi' + \cos\psi'\sin\psi_0\ \vec{x} \\ \sin\psi'\sin\xi'\ \vec{y} \\ \cos\psi'\cos\psi_0 - \sin\psi'\sin\psi_0\cos\xi'\ \vec{z} \end{Bmatrix}. \tag{9–34}$$

The edge is simply found by replacing the ψ' in Eq.(9–34) by a, which gives:

$$\vec{\rho}=\begin{Bmatrix} \sin\alpha\cos\psi_0\cos\xi'+\cos\alpha\sin\psi_0 & \vec{x} \\ \sin\alpha\sin\xi' & \vec{y} \\ \cos\alpha\cos\psi_0-\sin\alpha\sin\psi_0\cos\xi' & \vec{z} \end{Bmatrix} \tag{9-35}$$

Expressing the Φ and Ψ in the feed coordinate system results in ($\rho=\rho'$):

$$\begin{aligned}\Phi &= k\rho(1-\vec{\rho}\cdot\vec{r}) \\ &=k\rho'\{1-[\sin\theta\cos\phi(\sin\alpha\cos\psi_0\cos\xi'+\cos\alpha\sin\psi_0) \\ &\quad +\sin\theta\sin\phi\sin\alpha\sin\xi' \\ &\quad +\cos\theta(\cos\alpha\cos\psi_0-\sin\alpha\sin\psi_0\cos\xi')]\}\end{aligned} \tag{9-36}$$

and

$$\Psi = \rho'(1+\cos\alpha\cos\psi_0-\sin\alpha\sin\psi_0\cos\xi')-2f \tag{9-37}$$

The partial derivatives of Φ and Ψ to $\xi'$and ρ' are:

$$\frac{\partial\Phi}{\partial\xi'}=k\rho'(\sin\theta\cos\phi\sin\alpha\cos\psi_0\sin\xi'-\sin\theta\sin\phi\sin\alpha\cos\xi'-\cos\theta\sin\alpha\sin\psi_0\sin\xi') \tag{9-38}$$

$$\begin{aligned}\frac{\partial\Phi}{\partial\rho'}=k\{1-[&\sin\theta\cos\phi(\sin\alpha\cos\psi_0\cos\xi'+\cos\alpha\sin\psi_0)+\sin\theta\sin\phi\sin\alpha\sin\xi' \\ &+\cos\theta(\cos\alpha\cos\psi_0-\sin\alpha\sin\psi_0\cos\xi')]\}\end{aligned} \tag{9-39}$$

and

$$\frac{\partial\Psi}{\partial\xi'}=\rho'\sin\alpha\sin\psi_0\sin\xi' \tag{9-40}$$

$$\frac{\partial\Psi}{\partial\rho'}=1+\cos\alpha\cos\psi_0-\sin\alpha\sin\psi_0\cos\xi' \tag{9-41}$$

Applying the stationary phase point requirement:

$$\frac{\partial\Phi}{\partial\xi'}\frac{\partial\Psi}{\partial\rho'}-\frac{\partial\Phi}{\partial\rho'}\frac{\partial\Psi}{\partial\xi'}=0 \tag{9-42,a}$$

yields:

$$k\rho'(\sin\theta\cos\phi\sin\alpha\cos\psi_0\sin\xi'-\sin\theta\sin\phi\sin\alpha\cos\xi'-\cos\theta\sin\alpha\sin\psi_0\sin\xi')$$
$$\cdot(1+\cos\alpha\cos\psi_0-\sin\alpha\sin\psi_0\cos\xi')$$
$$-k\{1-[\sin\theta\cos\phi(\sin\alpha\cos\psi_0\cos\xi'+\cos\alpha\sin\psi_0)+\sin\theta\sin\phi\sin\alpha\sin\xi'$$
$$+\cos\theta(\cos\alpha\cos\psi_0-\sin\alpha\sin\psi_0\cos\xi')]\}\cdot\rho'\sin\alpha\sin\psi_0\sin\xi'=0 \qquad (9\text{–}42,b)$$

Factorizing the common terms and rearranging Eq.(9–42), we obtain the following equation which the stationary phase points must satisfy:

$$\sin\theta\cos\phi\sin\alpha\cos\psi_0\sin\xi'-\sin\theta\sin\phi\sin\alpha\cos\xi'-\cos\theta\sin\alpha\sin\psi_0\sin\xi'$$
$$+\sin\theta\cos\phi\sin\alpha\sin\xi'\cos\alpha-\sin\theta\sin\phi\sin\alpha\cos\xi'\cos\psi_0\cos\alpha$$
$$+\sin\theta\sin\phi\sin^2\alpha\sin\psi_0-\sin\psi_0\sin\alpha\sin\xi'=0 \qquad (9\text{–}43)$$

In accordance with Ierley and Zucker [23], the projection of the offset parabolic reflector on the x–y plane is considered to be the radiating aperture, so $\cos\theta\approx 0$ in Eq.(9–36) and, consequently, the terms containing $\cos\theta$ in Eq.(9–43) as well as the term $\sin\psi_0\sin\alpha\sin\xi'$ will disappear. So, in the case of $\sin\theta\neq 0$, Eq.(9–43) can be written as:

$$\cos\phi\sin\alpha\cos\psi_0\sin\xi'-\sin\phi\sin\alpha\cos\xi'+\cos\phi\sin\alpha\sin\xi'\cos\alpha$$
$$-\sin\phi\sin\alpha\cos\xi'\cos\psi_0\cos\alpha+\sin\phi\sin^2\alpha\sin\psi_0=0 \qquad (9\text{–}44)$$

Since $\sin\alpha$ is generally not equal to zero and is the common multiplication factor, the terms of the above equation, Eq.(9–44) reduces to:

$$-\sin\phi[(1+\cos\psi_0\cos\alpha)\cos\xi'-\sin\alpha\sin\psi_0]+\cos\phi(\cos\alpha+\cos\psi_0)\sin\xi'=0 \qquad (9\text{–}45)$$

which agrees with the results given by Ierley and Zucker [23].

When the approximation, $\cos\theta\approx 0$, is not made in Eq.(9–36), we find for the E–plane radiation pattern calculation ($\phi=0$), that Eq.(9–43) becomes:

$$\sin\alpha\sin\xi'[\sin\theta(\cos\psi_0+\cos\alpha)-\cos\theta\sin\psi_0-\sin\psi_0]=0 \qquad (9\text{–}46)$$

Some mathematical manipulations and rearranging the terms of Eq.(9–46) gives the following equations:

$$\mathrm{tg}\theta=0 \tag{9–47,a}$$

or

$$\mathrm{tg}\theta=\frac{2\sin\psi_0(\cos\psi_0+\cos\alpha)}{(\cos\psi_0+\cos\alpha)^2-\sin^2\psi_0} \tag{9–47,b}$$

which results agree with those given by Eq.(9–20,a) and Eq.(9–23).

For the H–plane radiation pattern calculation ($\phi=\frac{\pi}{2}$), Eq.(9–43) is given by:

$$-\sin\theta\sin\alpha(\cos\xi'+\cos\xi'\cos\psi_0\cos\alpha-\sin\alpha\sin\psi_0)-\cos\theta\sin\alpha\sin\psi_0\sin\xi'-\sin\psi_0\sin\alpha\sin\xi'=0 \tag{9–48}$$

yielding:

$$\mathrm{tg}\theta=0 \tag{9–49,a}$$

and

$$\mathrm{tg}\theta=-\frac{2\sin\psi_0\sin\xi'[\cos\psi_0\cos\alpha\cos\xi'+\cos\xi'-\sin\psi_0\sin\alpha]}{[\cos\psi_0\cos\alpha\cos\xi'+\cos\xi'-\sin\psi_0\sin\alpha]^2-\sin^2\psi_0\sin^2\xi'} \tag{9–49,b}$$

which gives the same results as Eq.(9–27,a) and Eq.(9–29).

To check the position in an arbitrary ϕ–plane, Eq.(9–43) is again used. Rearranging the terms in Eq.(9–43) in the following way:

$$\sin\theta[\cos\phi\sin\alpha\sin\xi'(\cos\psi_0+\cos\alpha)-\sin\phi\sin\alpha(\cos\psi_0\cos\alpha\cos\xi'+\cos\xi'-\sin\psi_0\sin\alpha)]$$
$$-\cos\theta\sin\alpha\sin\psi_0\sin\xi'-\sin\psi_0\sin\alpha\sin\xi'=0 \tag{9–50}$$

and by using the relation of $\cos^2\theta+\sin^2\theta=1$, the $\sin\theta$ and $\cos\theta$ can be derived separately as:

$$\begin{cases} \sin\theta=0 \\ \\ \sin\theta= \end{cases}$$

$$\frac{-2\{[(\cos\psi_0\cos\alpha+1)\cos\xi'-\sin\psi_0\sin\alpha]\sin\phi-[(\cos\psi_0+\cos\alpha)\cos\phi\sin\xi']\}\sin\xi'\sin\psi_0}{[(\cos\psi_0\cos\alpha\cos\xi'+\cos\xi'-\sin\psi_0\sin\alpha)\sin\phi-(\cos\psi_0+\cos\alpha)\sin\xi'\cos\phi]^2+\sin^2\psi_0\sin^2\xi'} \qquad (9\text{–}50,a)$$

and

$$\begin{cases} \cos\theta=-1 \\ \\ \cos\theta= \end{cases}$$

$$\frac{[(\cos\psi_0\cos\alpha\cos\xi'+\cos\xi'-\sin\psi_0\sin\alpha)\sin\phi-(\cos\psi_0+\cos\alpha)\sin\xi'\cos\phi]^2-\sin^2\psi_0\sin^2\xi'}{[(\cos\psi_0\cos\alpha\cos\xi'+\cos\xi'-\sin\psi_0\sin\alpha)\sin\phi-(\cos\psi_0+\cos\alpha)\sin\xi'\cos\phi]^2+\sin^2\psi_0\sin^2\xi'} \qquad (9\text{–}50,b)$$

Combining the above two equations results in:

$$\begin{cases} \theta=\pi \\ \\ \mathrm{tg}\theta= \end{cases}$$

$$\frac{-2\{[(\cos\psi_0\cos\alpha+1)\cos\xi'-\sin\psi_0\sin\alpha]\sin\phi-[(\cos\psi_0+\cos\alpha)\cos\phi\sin\xi']\}\sin\xi'\sin\psi_0}{[(\cos\psi_0\cos\alpha\cos\xi'+\cos\xi'-\sin\psi_0\sin\alpha)\sin\phi-(\cos\psi_0+\cos\alpha)\sin\xi'\cos\phi]^2-\sin^2\psi_0\sin^2\xi'} \qquad (9\text{–}50,c)$$

Which is exactly the same formula as Eq. (9–30) found for the GTD diffraction points.

From the above derivations it can be concluded that, also for an offset antenna configuration, the positions of the stationary phase points coincide with those of the diffraction points.

9.2.3.5 Caustics in the Symmetry–Plane

Eq.(9–20,a) represents the antenna forward–direction ($\theta=\pi$) which is a far–field caustic. For a symmetrical paraboloidal antenna, there is also a caustic in the antenna backward–direction ($\theta=0$), but due to the asymmetry this is not a caustic for an

offset configuration. However, a second caustic for an offset configuration appears at a specific θ–angle, which is completely determined by the offset geometry (ψ_0 and a). The equation for this second caustic is given by Eq.(9–23) because this formula is ξ'–angle independent. The diffracted rays from the whole edge of the reflector have in phase contributions in the far–field angle direction $\theta=2\psi_{p0}$ in the symmetry–plane. The mathematical proof of the existence of a caustic at this specific angle is given in [26] and was also given in equation form in [27]. This proof is based on the calculation of the distance from the feed to a far field–point measured along a point on the edge. It is proved that all these distances are the same. However, the existence of the second caustic can be demonstrated in a different way. As shown before, the projection of the edge–curve on the x–z plane is a line given by Eq.(8–2). This means that the complete edge is in a plane perpendicular to the x–z–plane. If all the rays from the edge to the far–field obeservation point in the forward–direction are mirrored at this plane, a second caustic is obtained (see Fig. 9–5). This is due to the fact that this mirroring has no effect on the length of the rays.

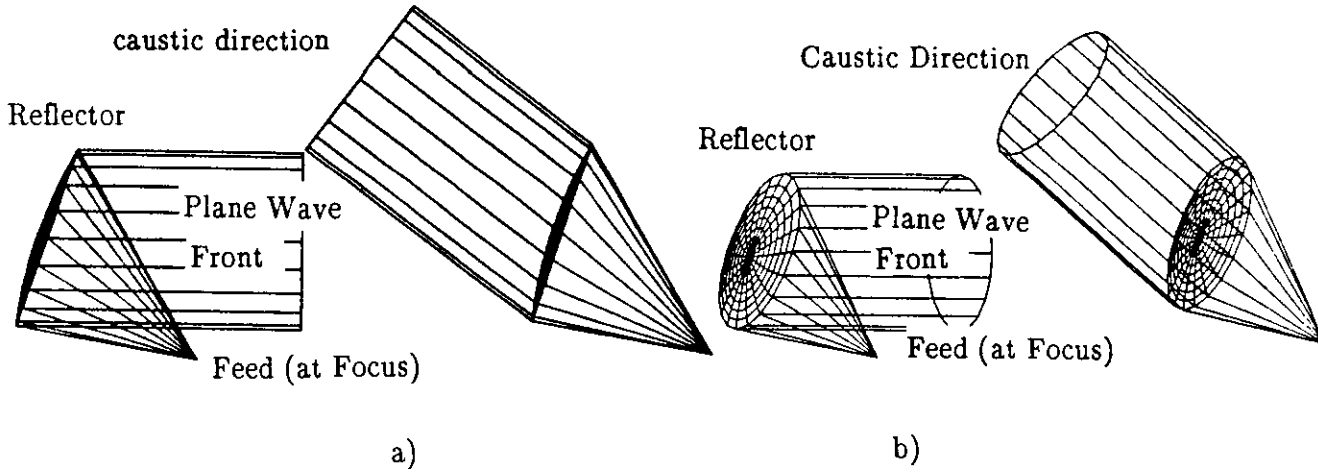

Fig.9–5 The Second Far–field Caustic: a) Side View; b) Back–side View

So, it can be concluded that there is a second caustic in the symmetry–plane in which the diffracted rays from all the edge points of the reflector give in–phase contributions and, consequently, it is necessary to use EEC instead of GTD in order to determine the far–field (see chapter 10)

9.2.3.6 Conclusion of the E– and H–plane Diffraction Point Analysis

The GTD diffraction points for an offset configuration which contribute to a far–field observation point have been found and they coincide with the positions of the points found when using the stationary phase method. This agrees with the results for the symmetrical parabolic configuration found in the first part of this report .

For the symmetry–plane pattern calculation, it can be seen that there are two caustics. One in the forward–direction, $\theta=\pi$ (given by Eq.(9–20,a)), which is due to the focusing properties of the parabolic reflector. However, there is a second far–field caustic (given by Eq.(9–23)), which is not in the backward–direction $\theta=0$ as is the case of the symmetrical antenna, but it appears at an observation angle $\theta=2\psi_{p0}$. This angle is shown to be completely determined by the offset configuration parameters ψ_0 and a.

Except for these two caustic directions, the E–plane ($\phi=0$) radiation pattern can be calculated from the contributions of the diffracted rays originating from two edge–points,viz. the upper point Q_u ($\xi'=0$) and the lower point Q_l ($\xi'=\pi$), which is analogous to the symmetrical case (normal incidence, $\beta_0=\pi/2$). Because the diffracted rays hit the edge of the reflector normal to its tangent ($\beta_0=\pi/2$), the two–dimensional model, as used for the symmetrical antenna configuration, is valid for the E–plane pattern calculation. This implies that the diffraction model for the E–plane pattern calculation can be a two–dimensional model.

For the H–plane and the other ϕ–planes, $\beta_0=\pi/2$ does not hold, so the two–dimensional model is not valid here and a three–dimensional model has to be used.

Further, it is shown that for a certain observation angle θ, the location of the diffraction points can be found from Eqs.(9–29) and (9–30) for the H–plane and arbitrary ϕ–plane, respectively.

9.3 Radiation Pattern Calculation

In the following sections, expressions have been derived for the caustic divergence factor and diffraction coefficient, they are needed for the GTD(UTD) radiation pattern calculation.

In the following sections, the E–plane pattern calculation will be dealt with separately from the pattern in an arbitrary ϕ–plane because, for the first analysis mentioned, the two–dimensional diffraction model is valid; while for the other analysis, the more complicated three–dimensional diffraction model should be used.

9.3.1 E–plane Pattern Calculation

As found in the previous section, only two points (upper point Q_u and lower point Q_l) contribute to the E–plane pattern for all θ angles except for the two caustic directions $\theta=2\psi_{p0}$ and $\theta=\pi$, where all the points on the edge have an in–phase contribution (see Chapter 10). Therefore, these two directions will be excluded for the E–plane pattern calculation and a two point method will be used for the remaining directions. The way of dealing with them, is analogous to that followed for the symmetrical antenna configuration in the first part of the report. Firstly, the caustic divergence factors for both points are determined, followed by a derivation of the corresponding dyadic diffraction coefficients.

9.3.1.1 Caustic Divergence Factor Calculation

As given in paragraph 4.2, the caustic divergence factor for a spherical wavefront is:

$$A(\rho_c,s^d)=\sqrt{\frac{\rho_c}{s^d(\rho_c+s^d)}} \qquad (9\text{–}51)$$

To derive the caustic divergence factors for the upper and lower diffraction point, the enlarged geometry for these two points is illustrated in Fig.9–6(a) and Fig. 9–6(b).

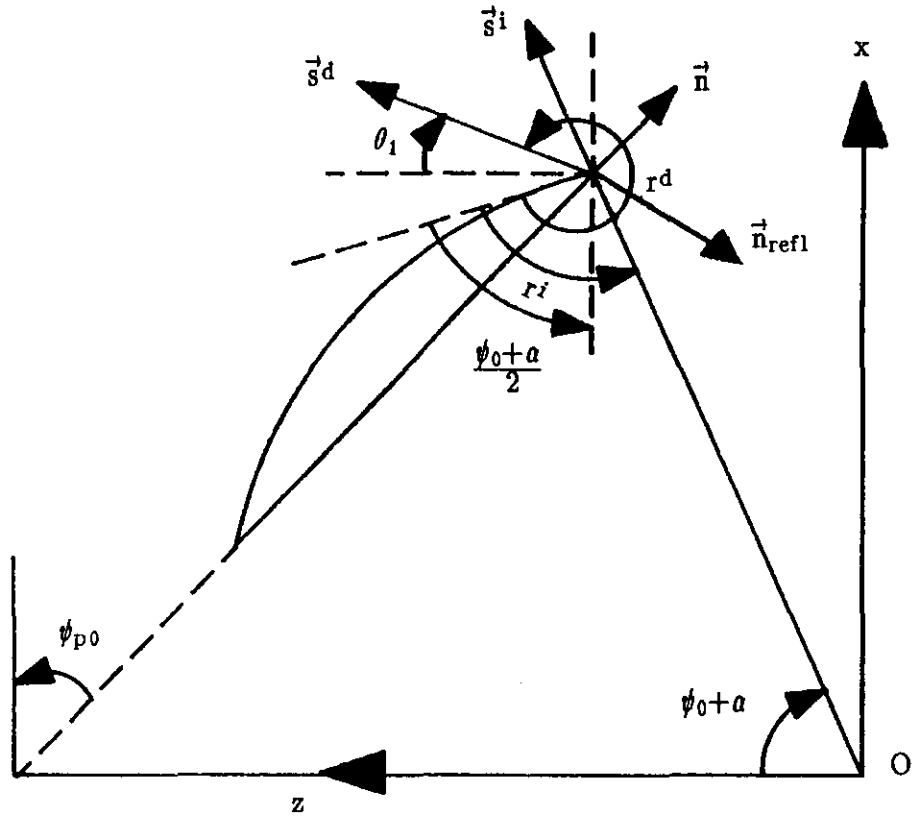

Fig. 9–6(a) Edge Diffraction at Upper Diffraction Point

9.3.1.1.1 Caustic Divergence Factor for the Upper Point

For the upper point, shown in Fig. 9–6(a), the following parameters can be derived:

$$\rho_e{}^i = \rho_1 = \frac{2f}{1+\cos(\psi_0+a)} \qquad (9\text{–}52,a)$$

$$\rho_g = \frac{2f\sin a}{\cos\psi_0+\cos a}\cos\psi_{p0} \qquad (9\text{–}52,b)$$

$$\beta_0 = \frac{\pi}{2} \tag{9–52,c}$$

$$\vec{n}\cdot\vec{s}_1^{\,i} = \sin(\psi_0+\alpha-\psi_{p0}) \tag{9–52,d}$$

$$\vec{n}\cdot\vec{s}_1^{\,d} = \sin(\theta_1-\psi_{p0}) \tag{9–52,e}$$

Inserting Eq.(9–52) in Eq.(9–51) results in:

$$\frac{1}{\rho_{c1}} = \frac{1+\cos(\psi_0+\alpha)}{2f} - \frac{[\sin(\psi_0+\alpha-\psi_{p0})-\sin(\theta_1-\psi_{p0})](\cos\psi_0+\cos\alpha)}{2f\sin\alpha\cos\psi_{p0}} \tag{9–53}$$

which can be reduced to (see [26]):

$$\frac{1}{\rho_{c1}} = \frac{\sin(\frac{\pi-\theta_1}{2})\sin(\frac{\theta_1-2\psi_{p0}}{2})(\cos\psi_0+\cos\alpha)}{f\sin\alpha\cos\psi_{p0}} \tag{9–54}$$

So, the caustic divergence factor for the field diffracted at the upper point is:

$$A(\rho_{c1},s_1^{\,d}) = \frac{1}{s_1^{\,d}}\sqrt{\frac{f\sin\alpha\cos\psi_{p0}}{\sin(\frac{\pi-\theta_1}{2})\sin(\frac{\theta_1-2\psi_{p0}}{2})(\cos\psi_0+\cos\alpha)}} \quad (s_1^{\,d}\gg\rho_{c1}) \tag{9–55}$$

It is clear that there are discontinuities for $\theta_1=2\psi_{p0}$ and $\theta_1=\pi$, and this corresponds to the two caustics derived previously.

9.3.1.1.2 Caustic Divergence Factor for the Lower Point

Following a similar procedure for the lower point, shown in Fig. 9–6(b), we can write:

$$\rho_e{}^i = \rho_2 = \frac{2f}{1+\cos(\psi_0-a)} \qquad (9\text{–}56,a)$$

$$\rho_g = \frac{2fs\,i\,n a}{\cos\psi_0+\cos a}\cos\psi_{p0} \qquad (9\text{–}56,b)$$

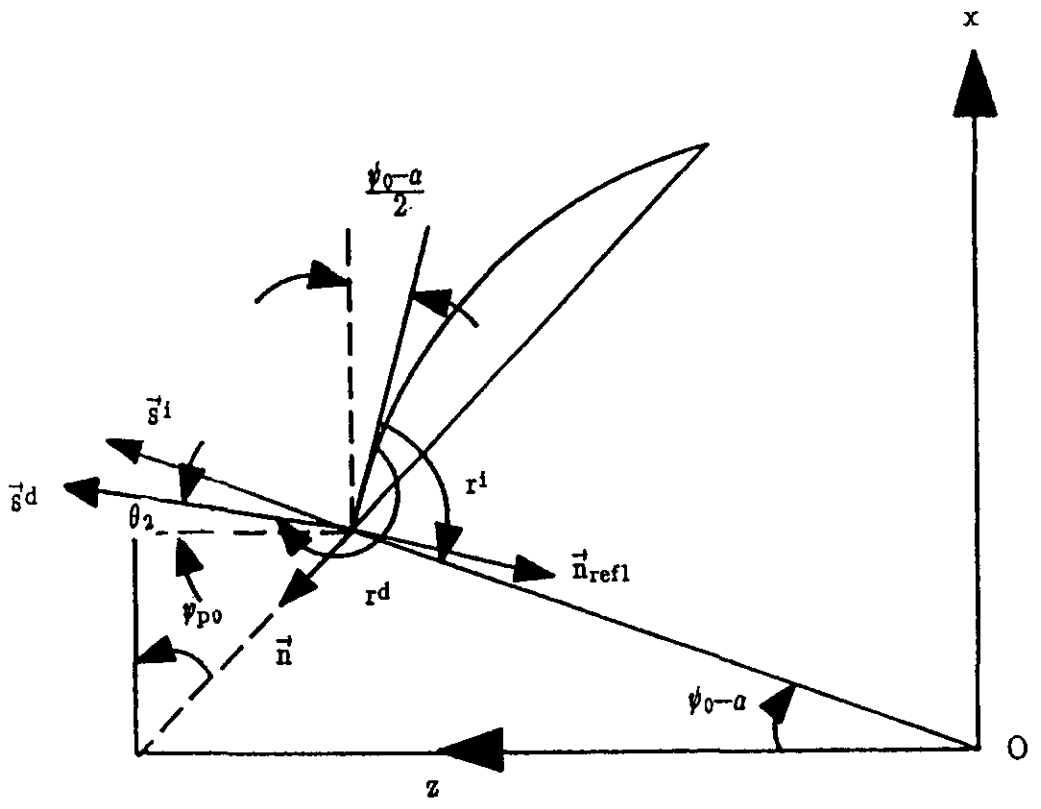

Fig. 9–6(b) Edge Diffraction at Lower Diffraction Point

$$\beta_0 = \frac{\pi}{2} \tag{9–56,c}$$

$$\vec{n}\cdot\vec{s}_2^{\,i} = \sin(\psi_{p0}+a-\psi_0) \tag{9–56,d}$$

$$\vec{n}\cdot\vec{s}_2^{\,d} = \sin(\psi_{p0}-\theta_2) \tag{9–56,e}$$

Inserting Eq.(9–56) in Eq.(9–51) results in:

$$\frac{1}{\rho_{c2}} = \frac{1+\cos(\psi_0-a)}{2f} - \frac{[\sin(\psi_{p0}+a-\psi_0)-\sin(\psi_{p0}-\theta_2)](\cos\psi_0+\cos a)}{2f\sin a\cos\psi_{p0}} \tag{9–57}$$

which can be reduced to (see [26]):

$$\frac{1}{\rho_{c2}} = -\frac{\sin(\frac{\pi-\theta_2}{2})\sin(\frac{\theta_2-2\psi_{p0}}{2})(\cos\psi_0+\cos a)}{f\sin a\cos\psi_{p0}} \tag{9–58}$$

So, the caustic divergence factor for the field diffracted at the lower point is:

$$A(\rho_{c2},s_2^{\,d}) = \frac{1}{s_2^{\,d}}\sqrt{\frac{f\sin a\cos\psi_{p0}}{\sin(\frac{\pi-\theta_2}{2})\sin(\frac{\theta_2-2\psi_{p0}}{2})(\cos\psi_0+\cos a)}}\, e^{j(\pi/2)} \quad (s_2^{\,d}\gg\rho_{c2}) \tag{9–59}$$

Again, $\theta_2=2\psi_{p0}$ and $\theta_2=\pi$ correspond to the two caustics derived before.

9.3.1.2 Diffraction Coefficient Calculation

The general formulas for the diffraction coefficients were given previously as:

$$D_{\substack{s\\h}} = -\frac{e^{-j(\pi/4)}}{2\sqrt{2\pi k}\sin\beta_0}\left\{\frac{F[kL^r a(r^d-r^i)]}{\cos\frac{r^d-r^i}{2}} \mp \frac{F[kL^d a(r^d+r^i)]}{\cos\frac{r^d+r^i}{2}}\right\} \tag{9–60}$$

Since the diffraction coefficients for the upper and lower point differ from those found for the the symmetrical antenna configuration, their derivation is repeated here.

9.3.1.2.1 Diffraction Coefficients for the Upper Point

From Fig. 9–6(a), which shows the angle definition of the incident and diffracted rays, it is possible to obtain:

$$r^i = \frac{\pi}{2} - \frac{\psi_0+\alpha}{2} \tag{9–61,a}$$

$$r^d = \begin{cases} \frac{3\pi}{2} + \frac{\psi_0+\alpha}{2} - \theta_1 & (0 \le \theta_1 < \frac{3\pi}{2} + \frac{\psi_0+\alpha}{2}) \\ 2\pi - (\theta_1 - \frac{3\pi+\psi_0+\alpha}{2}) & (\frac{3\pi}{2} + \frac{\psi_0+\alpha}{2} < \theta_1 < 2\pi) \end{cases} \tag{9–61,b}$$

$$\cos(\frac{r^d - r^i}{2}) = \begin{cases} -\sin(\frac{\psi_0+\alpha-\theta_1}{2}) & (0 \le \theta_1 < \frac{3\pi}{2} + \frac{\psi_0+\alpha}{2}) \\ \sin(\frac{\psi_0+\alpha-\theta_1}{2}) & (\frac{3\pi}{2} + \frac{\psi_0+\alpha}{2} < \theta_1 < 2\pi) \end{cases} \tag{9–62,a}$$

$$\cos(\frac{r^d + r^i}{2}) = \begin{cases} -\cos\frac{\theta_1}{2} & (0 \le \theta_1 < \frac{3\pi}{2} + \frac{\psi_0+\alpha}{2}) \\ \cos\frac{\theta_1}{2} & (\frac{3\pi}{2} + \frac{\psi_0+\alpha}{2} < \theta_1 < 2\pi) \end{cases} \tag{9–62,b}$$

and

$$L_1^i = \rho_u \tag{9–63,a}$$

$$L_1^r \to \infty \tag{9–63,b}$$

So,

$$D_h^s = \frac{\epsilon_{01} e^{-j(\pi/4)}}{2\sqrt{2\pi k}} \left\{ \frac{F[2k\rho_u \sin^2(\frac{\psi_0+\alpha-\theta_1}{2})]}{\sin(\frac{\psi_0+\alpha-\theta_1}{2})} \mp \frac{F[2kL_1^r \cos^2\frac{\theta_1}{2}]}{\cos\frac{\theta_1}{2}} \right\} \tag{9–64}$$

where

$$\epsilon_{01} = \begin{cases} 1 & (0 \le \theta_1 < \frac{3\pi}{2} + \psi_{p0}) \\ 0 & (\frac{3\pi}{2} + \psi_{p0} < \theta_1 < \frac{3\pi}{2} + \frac{\psi_0 + a}{2}) \\ -1 & (\frac{3\pi}{2} + \frac{\psi_0 + a}{2} < \theta_1 < 2\pi) \end{cases} \qquad (9\text{–}65)$$

The ϵ_{01} is introduced in order to account for the blocking effect that the reflector has on the diffracted rays from the edge of the reflector, also, to account for the sign change when the observation point moves from the angle region $\theta_1 \le \frac{3\pi}{2} + \psi_{p0}$ to the angle region $\theta_1 > \frac{3\pi + \psi_0 + a}{2}$.

If the direction $\theta_1 = \pi$, which is one of the caustics, is excluded from the calculation, Eq.(9–64) becomes:

$$D_h^s = \frac{\epsilon_{01} e^{-j(\pi/4)}}{2\sqrt{2\pi k}} \left\{ \frac{F[2k\rho_u \sin^2(\frac{\psi_0 + a - \theta_1}{2})]}{\sin(\frac{\psi_0 + a - \theta_1}{2})} \mp \frac{1}{\cos\frac{\theta_1}{2}} \right\} \qquad (9\text{–}66)$$

9.3.1.2.2 Diffraction Coefficients for the Lower Point

Following a similar procedure for the lower diffraction point, which is shown in Fig. 9–6(b), it is possible to write:

$$r^i = \frac{\pi}{2} + \frac{\psi_0 - a}{2} \qquad (9\text{–}67,a)$$

$$r^d = \begin{cases} \frac{3\pi}{2} - \frac{\psi_0 - a}{2} + \theta_2 & (0 \le \theta_2 < \frac{\pi}{2} + \frac{\psi_0 - a}{2}) \\ \theta_2 - (\frac{\pi + \psi_0 - a}{2}) & (\frac{\pi}{2} + \frac{\psi_0 - a}{2} < \theta_2 < 2\pi) \end{cases} \qquad (9\text{–}67,b)$$

$$\cos(\frac{r^d - r^i}{2}) = \begin{cases} -\sin(\frac{\theta_2 - \psi_0 + a}{2}) & (0 \le \theta_2 < \frac{\pi}{2} + \frac{\psi_0 - a}{2}) \\ \sin(\frac{\theta_2 - \psi_0 + a}{2}) & (\frac{\pi}{2} + \frac{\psi_0 - a}{2} < \theta_2 < 2\pi) \end{cases} \qquad (9\text{–}68,a)$$

$$\cos\left(\frac{r^d+r^i}{2}\right)=\begin{cases}-\cos\frac{\theta_2}{2} & \left(0\le\theta_2<\frac{\pi}{2}+\frac{\psi_0-a}{2}\right)\\ \cos\frac{\theta_2}{2} & \left(\frac{\pi}{2}+\frac{\psi_0-a}{2}<\theta_2<2\pi\right)\end{cases} \qquad (9\text{–}68,b)$$

and

$$L_2{}^i=\rho_1 \qquad (9\text{–}69,a)$$

$$L_2{}^r\to\infty \qquad (9\text{–}69,b)$$

So,

$$D_{fi}^{s}=\frac{\epsilon_{02}e^{-j(\pi/4\ )}}{2\sqrt{2\pi k}}\left\{\frac{F[2k\rho_1\sin^2(\frac{\theta_2-\psi_0+a}{2})]}{\sin(\frac{\theta_2-\psi_0+a}{2})}\mp\frac{F[2kL_2{}^r\cos^2\frac{\theta_2}{2}]}{\cos\frac{\theta_2}{2}}\right\} \qquad (9\text{–}70)$$

where

$$\epsilon_{02}=\begin{cases}1 & \left(0\le\theta_2<\frac{\pi}{2}+\frac{\psi_0-a}{2}\right)\\ 0 & \left(\frac{\pi}{2}+\frac{\psi_0-a}{2}<\theta_2<\frac{\pi}{2}+\psi_{p0}\right)\\ -1 & \left(\frac{3\pi}{2}+\frac{\psi_0-a}{2}<\theta_2<2\pi\right)\end{cases} \qquad (9\text{–}71)$$

The reason for the introduction of ϵ_{02} is the same as before.

If the direction $\theta_2=\pi$, which is one of the caustics is excluded from the calculation, Eq. (9–70) becomes:

$$D_{fi}^{s}=\frac{\epsilon_{02}e^{-j(\pi/4\ )}}{2\sqrt{2\pi k}}\left\{\frac{F[2k\rho_1\sin^2(\frac{\theta_2-\psi_0+a}{2})]}{\sin(\frac{\theta_2-\psi_0+a}{2})}\mp\frac{1}{\cos\frac{\theta_2}{2}}\right\} \qquad (9\text{–}72)$$

9.3.1.3 Incident Field at the Edge of the Reflector

According to the chapter 2, the field incident to the reflector from a x'–polarized feed is:

$$\vec{E}_f(\rho',\psi',\xi')=A_0\frac{e^{-jk\rho'}}{\rho'}\sqrt{G_f(\psi')}(U_{\psi'}\cos\xi'\vec{\psi}'+\sin\xi'\vec{\zeta}') \qquad (9\text{–}73)$$

or

$$\vec{E}_f(\rho',\psi',\xi')=A_0\frac{e^{-jk\rho'}}{\rho'}\sqrt{G_f(\psi')}\begin{bmatrix} U_\psi,\cos\xi' & \vec{\psi}' \\ \sin\xi' & \vec{\xi}' \end{bmatrix} \tag{9–74}$$

and for the edge point, Eq.(9–73) and Eq.(9–74) becomes:

$$\vec{E}_f(\rho',a,\xi')=A_0\frac{e^{-jk\rho'}}{\rho'}\sqrt{G_f(a)}(U_a\cos\xi'\vec{\psi}'+\sin\xi'\vec{\xi}') \tag{9–75}$$

or

$$\vec{E}_f(\rho',a,\xi')=A_0\frac{e^{-jk\rho'}}{\rho'}\sqrt{G_f(a)}\begin{bmatrix} U_a\cos\xi' & \vec{\psi}' \\ \sin\xi' & \vec{\xi}' \end{bmatrix} \tag{9–76}$$

For the upper diffraction point $Q_u(\rho_u',a,0)$, the incident field from the feed is given by:

$$\vec{E}_f(\rho_u,a,0)=A_0\frac{e^{-jk\rho_u}}{\rho_u}\sqrt{G_f(a)}\begin{bmatrix} U_a & \vec{\psi}' \\ 0 & \vec{\xi}' \end{bmatrix} \tag{9–77}$$

Insertion of A_0 and U_ψ, as defined in chapter 2, in Eq.(9–77) results in:

$$\vec{E}_f(\rho_u,a,0)=(\eta\frac{P_t}{2\pi})^{\frac{1}{2}}\frac{e^{-jk\rho_u}}{\rho_u}\sqrt{G_f(a)}\begin{bmatrix} 1 & \vec{\psi}' \\ 0 & \vec{\xi}' \end{bmatrix} \tag{9–78}$$

for Huygens feed polarization.

By using a transformation, the $\vec{E}(\rho_u,a,0)$ can be expressed by $\vec{E}(\rho_u,\psi_0+a,0)$ in the reflector coordinate system, yielding:

$$\vec{E}_f(\rho_u,\psi_0+a,0)=(\eta\frac{P_t}{2\pi})^{\frac{1}{2}}\frac{e^{-jk\rho_u}}{\rho_u}\sqrt{G_f(a)}\begin{bmatrix} 1 & \vec{\psi} \\ 0 & \vec{\xi} \end{bmatrix} \tag{9–79}$$

So, the incident field at $Q_u(\rho_u,\psi_0+a,0)$ in the (ρ,ψ,ξ) reflector coordinate system is:

$$\vec{E}_f(\rho_u,\psi_0+a,0)=(\eta\frac{P_t}{2\pi})^{\frac{1}{2}}\frac{e^{-jk\rho_u}}{\rho_u}\sqrt{G_f(a)}\ \vec{\psi} \tag{9–80}$$

similarly, the incident field at $Q_1(\rho_1,\psi_0-a,0)$ is:

$$\vec{E}_f(\rho_1,\psi_0-a,0)=(\eta\frac{P_t}{2\pi})^{\frac{1}{2}}\frac{e^{-jk\rho_1}}{\rho_1}\sqrt{G_f(a)}\ \vec{\psi} \qquad (9\text{–}81)$$

9.3.1.4 Far–field Pattern Calculation

9.3.1.4.1. Contribution of the Upper Point to the Far–field

Since the dyadic diffraction coefficient, which relates the diffracted field to the incident field, is defined in the edge–fixed coordinate system (shown in Fig. 9–1), the diffracted and incident fields have to be transformed to this coordinate system. In Fig. 9–7, the field vectors are defined and their components are related as follows:

$$E^i_{\phi_{01}} = E^i_{f\psi_1} \qquad (9\text{–}82,a)$$

$$E^i_{\beta_{01}} = E^i_{f\xi_1} \qquad (9\text{–}82,b)$$

$$E^d_{\theta_1} = -E^d_{\phi_{01}} \qquad (9\text{–}83,a)$$

$$E^d_{\phi_1} = -E^d_{\beta_{01}} \qquad (9\text{–}83,b)$$

So:

$$\begin{bmatrix} E^d_{\theta_1} \\ E^d_{\phi_1} \end{bmatrix} = -\begin{bmatrix} E^d_{\phi_{01}} \\ E^d_{\beta_{01}} \end{bmatrix}$$

$$= -\begin{bmatrix} -D_h & 0 \\ 0 & -D_s \end{bmatrix}\begin{bmatrix} E^i_{\phi_{01}} \\ E^i_{\beta_{01}} \end{bmatrix}\sqrt{\frac{\rho_{c1}}{s^d_1(\rho_{c1}+s^d_1)}}\,e^{-jks^d_1}$$

$$= -\begin{bmatrix} -D_h & 0 \\ 0 & -D_s \end{bmatrix}\begin{bmatrix} E^i_{f\psi_1} \\ E^i_{f\xi_1} \end{bmatrix}\sqrt{\frac{\rho_{c1}}{s^d_1(\rho_{c1}+s^d_1)}}\,e^{-jks^d_1}$$

$$= (\eta \frac{P_t}{2\pi})^{\frac{1}{2}} \frac{e^{-jk\rho_u}}{\rho_u} \sqrt{G_f(a)\rho_{c1}} \frac{e^{-jks_1^d}}{s_1^d} \begin{bmatrix} D_h & 0 \\ 0 & D_s \end{bmatrix} \begin{bmatrix} 1 & \vec{\psi} \\ 0 & \vec{\zeta} \end{bmatrix} \qquad (9\text{–}84)$$

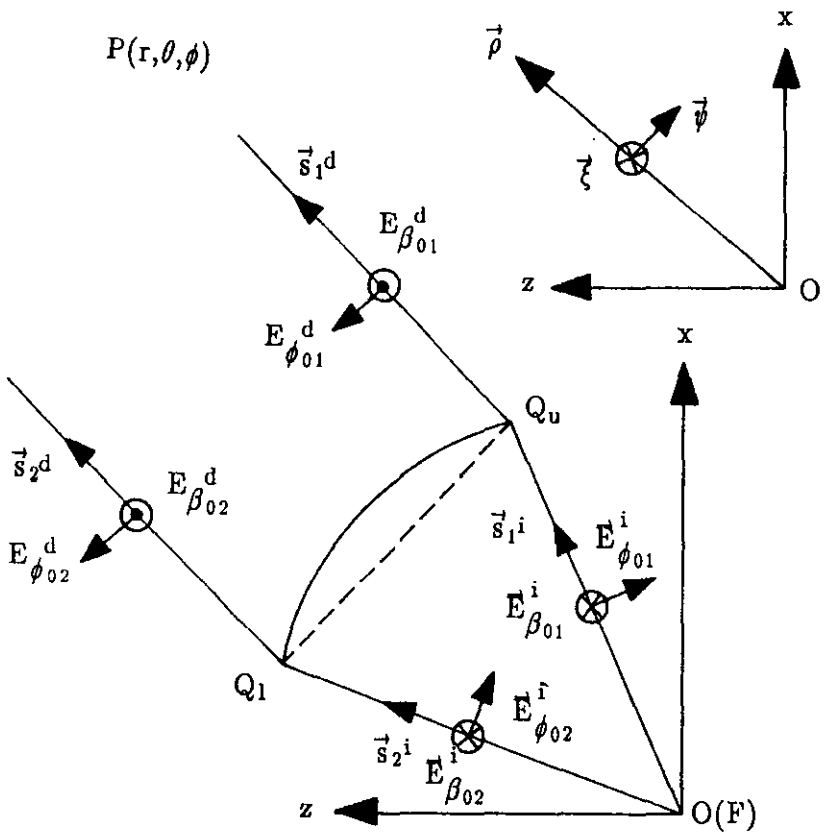

Fig. 9–7 Two–dimensional Illustration of the Field Vector Relation for Edge Diffraction at the Upper and Lower Point

using the far–field approximation:

$$s_1^d = r \qquad \text{for amplitude} \qquad (9\text{–}85,a)$$

$$s_1^d = r - \rho_u \cos(\psi_0 + a - \theta_1) \qquad \text{for phase} \qquad (9\text{–}85,b)$$

gives:

$$\begin{bmatrix} E_{\theta_1}^d \\ E_{\phi_1}^d \end{bmatrix} = (\eta \frac{P_t}{2\pi})^{\frac{1}{2}} \frac{e^{-jkr}}{r} \sqrt{\frac{G_f(a)\rho_{c1}}{\rho_u^2\, 8\pi k}} \epsilon_{01} \left\{ \frac{F[2k\rho_u \sin^2(\frac{\psi_0 + a - \theta_1}{2})]}{\sin(\frac{\psi_0 + a - \theta_1}{2})} \pm \frac{1}{\cos\frac{\theta_1}{2}} \right\}$$

$$\cdot e^{-j\{k\rho_u[1-\cos(\psi_0 + a - \theta_1)] + \frac{\pi}{4}\}} \begin{bmatrix} 1 & \vec{\psi} \\ 0 & \vec{\zeta} \end{bmatrix}$$

$$= (\eta \frac{P_t}{2\pi})^{\frac{1}{2}} \frac{e^{-jkr}}{r} \sqrt{\frac{G_f(a) f \sin a \cos\psi_{p0}}{8\rho_u^2 \pi k \sin(\frac{\pi - \theta_1}{2}) \sin(\frac{\theta_1 - 2\psi_{p0}}{2})(\cos\psi_0 + \cos a)}}$$

$$\cdot \epsilon_{01} \left\{ \frac{F[2k\rho_u \sin^2(\frac{\psi_0 + a - \theta_1}{2})]}{\sin(\frac{\psi_0 + a - \theta_1}{2})} \pm \frac{1}{\cos\frac{\theta_1}{2}} \right\}$$

$$\cdot e^{-j\{k\rho_u[1-\cos(\psi_0 + a - \theta_1)] + \frac{\pi}{4}\}} \begin{bmatrix} 1 & \vec{\psi} \\ 0 & \vec{\zeta} \end{bmatrix} \qquad (9\text{–}86)$$

9.3.1.4.2. Contribution of the Lower Point to the Far–field

Similarly, the relation between the field components at Q_1 are:

$$E_{\phi_{02}}^i = E_{f\psi_2}^i \qquad (9\text{–}87,a)$$

$$E_{\beta_{02}}^i = E_{f\xi_2}^i \qquad (9\text{–}87,b)$$

$$E_{\theta_2}^d = -E_{\phi_{02}}^d \qquad (9\text{–}88,a)$$

$$E_{\phi_2}^{d} = -E_{\beta_{02}}^{d} \tag{9–88,b}$$

So:

$$\begin{bmatrix} E_{\theta_2}^{d} \\ E_{\phi_2}^{d} \end{bmatrix} = -\begin{bmatrix} E_{\phi_{02}}^{d} \\ E_{\beta_{02}}^{d} \end{bmatrix}$$

$$= -\begin{bmatrix} -D_h & 0 \\ 0 & -D_s \end{bmatrix} \begin{bmatrix} E_{\phi_{02}}^{i} \\ E_{\beta_{02}}^{i} \end{bmatrix} \sqrt{\frac{\rho_{c2}}{s_2^d(\rho_{c2}+s_2^d)}}\, e^{-jks_2^d}$$

$$= -\begin{bmatrix} -D_h & 0 \\ 0 & -D_s \end{bmatrix} \begin{bmatrix} E_{f\psi_2}^{i} \\ E_{f\xi_2}^{i} \end{bmatrix} \sqrt{\frac{\rho_{c2}}{s_2^d(\rho_{c2}+s_2^d)}}\, e^{-jks_2^d}$$

$$= (\eta\frac{P_t}{2\pi})^{\frac{1}{2}} \frac{e^{-jk\rho_1}}{\rho_1} \sqrt{G_f(a)\rho_{c2}} \frac{e^{-jks_2^d}}{s_2^d} \begin{bmatrix} D_h & 0 \\ 0 & D_s \end{bmatrix} \begin{bmatrix} 1 & \vec{\psi} \\ 0 & \vec{\xi} \end{bmatrix} \tag{9–89}$$

using the far–field approximation:

$s_2^d = r$ for amplitude (9–90,a)

$s_2^d = r - \rho_1 \cos(\psi_0 - a - \theta_2)$ for phase (9–90,b)

gives:

$$\begin{bmatrix} E_{\theta_2}^{d} \\ E_{\phi_2}^{d} \end{bmatrix} = (\eta\frac{P_t}{2\pi})^{\frac{1}{2}} \frac{e^{-jkr}}{r} \sqrt{\frac{G_f(a)\rho_{c2}}{\rho_1^2\ 8\pi k}} \epsilon_{02} \left\{ \frac{F[2k\rho_1 \sin^2(\frac{\theta_2-\psi_0+a}{2})]}{\sin(\frac{\theta_2-\psi_0+a}{2})} \pm \frac{1}{\cos\frac{\theta_2}{2}} \right\}$$

$$\cdot e^{-j\{k\rho_1[1-\cos(\theta_2-\psi_0+a)]-\frac{\pi}{4}\}} \begin{bmatrix} 1 & \vec{\psi} \\ 0 & \vec{\xi} \end{bmatrix}$$

$$= (\eta\frac{P_t}{2\pi})^{\frac{1}{2}} \frac{e^{-jkr}}{r} \sqrt{\frac{G_f(a) f \sin a \cos\psi_{p0}}{8\rho_1^2 \pi k \sin(\frac{\pi-\theta_2}{2}) \sin(\frac{\theta_2-2\psi_{p0}}{2})(\cos\psi_0+\cos a)}}$$

$$\cdot \epsilon_{01} \left\{ \frac{F[2k\rho_1 \sin^2(\frac{\theta_2-\psi_0+a}{2})]}{\sin(\frac{\theta_2-\psi_0+a}{2})} \pm \frac{1}{\cos\frac{\theta_2}{2}} \right\}$$

$$\cdot e^{-j\{k\rho_1[1-\cos(\theta_2-\psi_0+a)]-\frac{\pi}{4}\}} \begin{bmatrix} 1 & \vec{\psi} \\ 0 & \vec{\xi} \end{bmatrix} \tag{9–91}$$

9.3.1.4.3. Total Radiation Pattern in E–plane

The total field can now simply be obtained by summing the direct field from the feed and the diffracted fields from the diffraction points:

$$\begin{bmatrix} E^d_\theta \\ E^d_\phi \end{bmatrix} = \begin{bmatrix} E^i_{f\theta} \\ E^i_{f\phi} \end{bmatrix} + \begin{bmatrix} E^d_{\theta_1} \\ E^d_{\phi_1} \end{bmatrix} + \begin{bmatrix} E^d_{\theta_2} \\ E^d_{\phi_2} \end{bmatrix} \tag{9–92}$$

where the direct field is:

$$\begin{bmatrix} E^i_{f\theta} \\ E^i_{f\phi} \end{bmatrix} = (\eta \frac{P_t}{2\pi})^{\frac{1}{2}} \frac{e^{-jkr}}{r} \sqrt{G_f(|\theta - \psi_0|)} \begin{bmatrix} 1\vec{\psi} \\ 0\vec{\zeta} \end{bmatrix} \tag{9–93}$$

9.3.2 Arbitrary ϕ–plane Pattern Calculation

The radiation pattern calculation in an arbitrary ϕ–plane differs from the E–plane pattern calculation because generally the incident rays are not normal to the tangent at the diffraction point. Therefore, the calculation is more complex than the calculation for the E–plane, and a three–dimensional diffraction model is needed.

A similar procedure as for the E–plane is followed, starting with calculating of the caustic divergence factors and the diffraction coefficients. But firstly, the edge of an offset reflector is shown in Fig. 9–8 in order to illustrate its geometry in the reflector coordinate system.

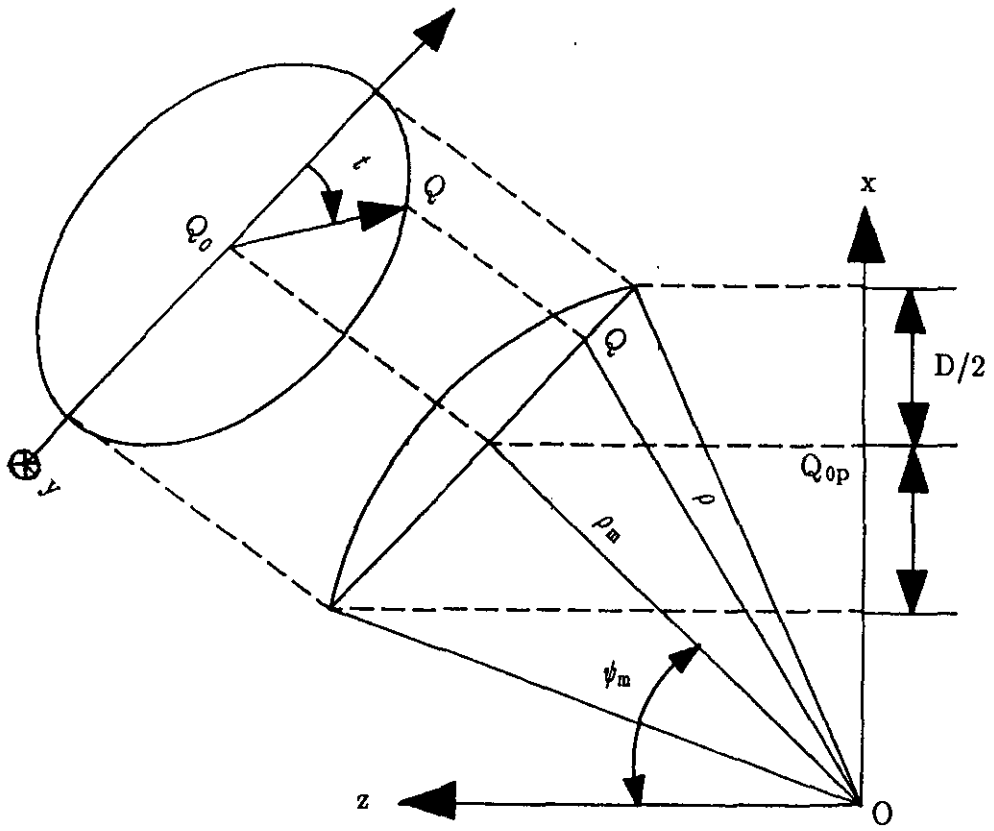

Fig. 9–8 Three–dimensional Model of Edge Diffraction for an Offset Configuration

9.3.2.1 Caustic Divergence Factor Calculation

Eqs.(4–3) and (4–4) show that for the calculation of the caustic divergence factor expressions are needed for $\vec{n}$, $\vec{s}_i$, $\vec{s}_d$, ρ_g, ρ_c and β_0. The unit vector $\vec{n}$ is parallel to the intersection line between the plane perpendicular to the unit vector $\vec{T}$ and the plane formed by the edge of the reflector, and is given by:

$$\vec{n} = \det\begin{bmatrix} T_y & T_z \\ 0 & \cos\psi_{p0} \end{bmatrix}\vec{x} + \det\begin{bmatrix} T_z & T_x \\ \cos\psi_{p0} & \sin\psi_{p0} \end{bmatrix}\vec{y} + \det\begin{bmatrix} T_x & T_y \\ \sin\psi_{p0} & 0 \end{bmatrix}\vec{z} \qquad (9\text{–}94)$$

Further, $\vec{s}^i$ is the unit vector in the direction of the incident ray, which

for this case coincides with $\vec{\rho}$:

$$\vec{s}^{i}=\vec{\rho} \tag{9–95}$$

with

$$\vec{\rho}=\begin{bmatrix} \sin\psi_0\cos\alpha+\cos\xi'\cos\psi_0\sin\alpha & \vec{x} \\ \sin\alpha\sin\xi' & \vec{y} \\ \cos\psi_0\cos\alpha-\cos\xi'\sin\psi_0\sin\alpha & \vec{z} \end{bmatrix} = \begin{bmatrix} \rho_x & \vec{x} \\ \rho_y & \vec{y} \\ \rho_z & \vec{z} \end{bmatrix}, \tag{9–96}$$

$\vec{s}^{d}$ can be considered as being parallel to the unit vector $\vec{r}$ to the far–field observation point, so:

$$\vec{s}^{d}\approx\vec{r}=\begin{bmatrix} \sin\theta\cos\phi & \vec{x} \\ \sin\theta\sin\phi & \vec{y} \\ \cos\theta & \vec{z} \end{bmatrix} = \begin{bmatrix} r_x & \vec{x} \\ r_y & \vec{y} \\ r_z & \vec{z} \end{bmatrix} \tag{9–97}$$

As shown in Fig. 9–8, the center of the reflector aperture is at Q_0 (x_0,y_0,z_0), with its coordinates in the reflector coordinate system (see [26]) given by:

$$x_0=\frac{2f\sin\psi_0}{\cos\psi_0+\cos\alpha} \tag{9–98}$$

$$y_0=0 \tag{9–99}$$

$$z_0=x_0/\mathrm{tg}\psi_m \tag{9–100}$$

where

$$\mathrm{tg}\psi_m=\frac{\sin\psi_0(\cos\psi_0+\cos\alpha)}{\cos\alpha(\cos\psi_0+\cos\alpha)-\sin^2\psi_0} \tag{9–101}$$

The vector radius $\rho_m\vec{\rho}_m$ pointing from the feed (F) to Q_0 is:

$$\rho_m\vec{\rho}_m=\frac{x_0}{\sin\psi_m}(\sin\psi_m\,\vec{x}+\cos\psi_m\,\vec{z}) \tag{9–102}$$

with

$$\sin\psi_m = \frac{\sin\psi_0(\cos\psi_0+\cos\alpha)}{\sin^2\psi_0\sin^2\alpha+\cos^2\alpha(\cos\psi_0+\cos\alpha)^2}, \tag{9–103,a}$$

$$\cos\psi_m = \frac{\cos\alpha(\cos\psi_0+\cos\alpha)-\sin^2\psi_0}{\sin^2\psi_0\sin^2\alpha+\cos^2\alpha(\cos\psi_0+\cos\alpha)^2}, \tag{9–103,b}$$

The vector from the feed to any diffraction point at the edge of reflector is:

$$\rho\vec{\rho} = \rho\begin{bmatrix} \sin\psi_0\cos\alpha+\cos\xi'\cos\psi_0\sin\alpha & \vec{x} \\ \sin\alpha\sin\xi' & \vec{y} \\ \cos\psi_0\cos\alpha-\cos\xi'\sin\psi_0\sin\alpha & \vec{z} \end{bmatrix} = \rho\begin{bmatrix} \rho_x & \vec{x} \\ \rho_y & \vec{y} \\ \rho_z & \vec{z} \end{bmatrix} \tag{9–104}$$

with

$$\rho = \frac{2f}{1+\cos\psi_0\cos\alpha-\cos\xi'\sin\psi_0\sin\alpha} \tag{9–105}$$

Knowledge of the $\rho\vec{\rho}$ and $\rho_m\vec{\rho}_m$ is necessary to find the unit vector $\vec{n}_0$ in the direction from the center Q_0 of the edge curve to the edge of the offset reflector:

$$\vec{n}_0 = \frac{\rho\vec{\rho}-\rho_m\vec{\rho}_m}{|\rho\vec{\rho}-\rho_m\vec{\rho}_m|} \tag{9–106}$$

where

$$\rho\vec{\rho}-\rho_m\vec{\rho}_m = \begin{bmatrix} \rho\rho_x-x_0 & \vec{x} \\ \rho\rho_y & \vec{y} \\ \rho\rho_z-x_0/\mathrm{tg}\psi_m & \vec{z} \end{bmatrix} \tag{9–107}$$

$$|\rho\vec{\rho}-\rho_m\vec{\rho}_m| = \sqrt{(\rho\rho_x-x_0)^2+(\rho\rho_y)^2+(\rho\rho_z-x_0/\mathrm{tg}\psi_m)^2} \tag{9–108}$$

Because the edge curve is elliptical, the curvature radius of the edge at any point is given by:

$$\rho_g = \left| \frac{[a^2\sin^2 t + b^2\cos^2 t]^{\frac{3}{2}}}{ab(\sin^2 t - \cos^2 t)} \right| \qquad (9\text{–}109)$$

slith t, being the angle between $\vec{n}_0$ and the projection of $\vec{x}$ on the edge plane, given by114 $\sin(t) = \vec{n}_0 \cdot \vec{y}$ (9–110)

and

$$a = \frac{2f\sin\alpha}{(\cos\psi_0 + \cos\alpha)\cos\psi_{p0}} \qquad (9\text{–}111,a)$$

$$b = \frac{2f\sin\alpha}{\cos\psi_0 + \cos\alpha} \qquad (9\text{–}111,b)$$

with

$$\cos\psi_{p0} = \frac{(\cos\psi_0 + \cos\alpha)}{\sqrt{[(\cos\psi_0 + \cos\alpha)^2 + \sin^2\psi_0]}} \qquad (9\text{–}111,c)$$

Since $\rho_e{}^i = \rho$ and β_0 can be deriv from Eq.(9–17), ρ_c can be obtained by inserting $\vec{n}$, $\vec{s}^i$, $\vec{s}^d$, ρ_g in Eq.(4–4). Which allows the caustic divergence factor to be derived using Eq.(4–3).

9.3.2.2 Diffraction Coefficient Calculation

The general expression for the dyadic diffraction coefficient given in section 4.3 (Eq.(4–12)) shows that, r^i and r^d are needed for the calculation. r^i in the equation, is the angle between the incident plane and the reflector tangent plane at the diffraction point, while r^d is the angle between the diffraction plane and the reflector tangent plane at the point of diffraction.

The incident plane is the plane containing the vectors $\vec{\rho}$ and $\vec{T}$, where the unit normal vector $\vec{N}_s$ is given by:

$$\vec{N}_s = \det\begin{bmatrix} T_y & T_z \\ \rho_y & \rho_z \end{bmatrix}\vec{x}+\det\begin{bmatrix} T_z & T_x \\ \rho_z & \rho_x \end{bmatrix}\vec{y}+\det\begin{bmatrix} T_x & T_y \\ \rho_x & \rho_y \end{bmatrix}\vec{z} \qquad (9\text{–}112)$$

and the unit normal vector $\vec{n}_{refl}$ of the plane tangent to the reflector at the diffraction point is:

$$\vec{n}_{refl} = -\cos\frac{\psi}{2}\vec{\rho} + \sin\frac{\psi}{2}\vec{\psi}$$

$$= \begin{bmatrix} -\cos\xi\sin\frac{\psi}{2}\vec{x} \\ -\sin\xi\sin\frac{\psi}{2}\vec{y} \\ -\cos\frac{\psi}{2}\qquad\vec{z} \end{bmatrix} \qquad (9\text{–}113)$$

So, the angle r^i can be calculated by taking the dot product of the vectors $\vec{N}_s$ and $\vec{n}_{refl}$:

$$\cos(r^i)=\vec{N}_s\cdot\vec{n}_{refl}. \qquad (9\text{–}114)$$

The diffraction plane is the plane containing the unit vector $\vec{s}^d$ and $\vec{T}$. In the far–field, the $\vec{s}^d$ is approximately parallel to the unit vector $\vec{r}$ as given Eq.(9–97):

$$\vec{s}^d \approx \vec{r} = r_x\vec{x} + r_y\vec{y} + r_z\vec{z} \qquad (9\text{–}115)$$

so, the unit normal vector $\vec{N}_d$ of the diffraction plane is:

$$\vec{N}_d = \det\begin{bmatrix} T_y & T_z \\ r_y & r_z \end{bmatrix}\vec{x}+\det\begin{bmatrix} T_z & T_x \\ r_z & r_x \end{bmatrix}\vec{y}+\det\begin{bmatrix} T_x & T_y \\ r_x & r_y \end{bmatrix}\vec{z} \qquad (9\text{–}116)$$

Similarly, the the angle r^d can be calculated by taking the dot product of the vectors $\vec{N}_d$ and $\vec{n}_{refl}$:

$$\cos(r^d)= \vec{N}_d\cdot\vec{n}_{refl}. \qquad (9\text{–}117)$$

For a paraboloidal reflector and a spherical incident wave, it was shown previously that:

$$L^{i}=\rho \tag{9–118,a}$$

$$L^{r\to\infty} \tag{9–118,b}$$

By knowing the r^d, r^i and β_0, the $D_{\substack{s\\h}}$ can be obtained from:

$$D_{\substack{s\\h}} = -\frac{\epsilon_0 e^{-j(\pi/4)}}{2\sqrt{2\pi k}\sin\beta_0}\left[\frac{F[k\rho a(r^d-r^i)]}{\cos\frac{r^d-r^i}{2}} \mp \frac{1}{\cos\frac{r^d+r^i}{2}}\right]. \tag{9–119}$$

where ϵ_0 is introduced as before to account for the blockage effect of the reflector.

9.3.2.3 Incident Field at the Edge of the Reflector

Now, expressions for the caustic divergence factors and the diffraction coefficients have been derived. But, the diffraction coefficients, which relate the diffracted field vector to the incident field vector, can be defined in the edge–fixed coordinate system; therefore, it is necessary to express the incident and diffracted fields in the (x''',y''',z''') coordinate system, which is a diffraction–point–fixed coordinate system.

In Chapter 2, the incident field at the edge in (ρ',ψ',ζ') spherical feed coordinate system is given as:

$$\vec{E}_f(\rho',a,\zeta')=A_0\frac{e^{-jk\rho'}}{\rho'}\sqrt{G_f(a)}(U_a\cos\zeta'\vec{\psi}'+\sin\zeta'\vec{\zeta}') \tag{9–120}$$

or in the (x',y',z') rectangular feed coordinate system as:

$$\vec{E}_f(x',y',z') = \begin{bmatrix} E_{fx}^{i},\ \vec{x}' \\ E_{fy}^{i},\ \vec{y}' \\ E_{fz}^{i},\ \vec{z}' \end{bmatrix} \tag{9–121}$$

where

$$\begin{bmatrix} E_{fx'}^{i} \\ E_{fy'}^{i} \\ E_{fz'}^{i} \end{bmatrix} =$$

$$= A_0 \frac{e^{-jk\rho'}}{\rho'} \sqrt{G_f(a)} \begin{bmatrix} \cos^2\xi'(\cos a U_a + 1) - 1 \\ \cos\xi' \sin\xi' (\cos a U_a + 1) \\ -U_a \sin a \cos\xi' \end{bmatrix} \qquad (9\text{–}122)$$

After transformation to the (x,y,z) reflector coordinate system, the incident field becomes:

$$\begin{bmatrix} E_{fx}^{i} \\ E_{fy}^{i} \\ E_{fz}^{i} \end{bmatrix} =$$

$$= A_0 \frac{e^{-jk\rho'}}{\rho'} \sqrt{G_f(a)} \begin{bmatrix} \cos\psi_0[\cos^2\xi'(\cos a\ U_a + 1) - 1] - U_a \sin a \cos\xi' \sin\psi_0 \\ \cos\xi' \sin\xi' (\cos a U_a + 1) \\ -\sin\psi_0[\cos^2\xi'(\cos a U_a + 1) - 1] - U_a \cos\psi_0 \sin a \cos\xi' \end{bmatrix} \qquad (9\text{–}123)$$

Finally, by using the transformation matrix M^T, the expression of the incident field in (x''',y''',z''') system is obtained as:

$$\begin{bmatrix} E_{fx,,,}^{i} \\ E_{fy,,,}^{i} \\ E_{fz,,,}^{i} \end{bmatrix} = M^T \begin{bmatrix} E_{fx}^{i} \\ E_{fy}^{i} \\ E_{fz}^{i} \end{bmatrix}. \qquad (9\text{–}124)$$

Fig. 9–9 shows the vectors in the (x''',y''',z''') coordinate system, the (ρ^t,θ^t,ϕ^t) coordinate system is used in the figure for relating the spherical and the rectangular field components. The incident and diffracted field vector can be written as [26]:

$$\begin{bmatrix} E_{\rho^t}^{i} \\ E_{\theta^t}^{i} \\ E_{\phi^t}^{i} \end{bmatrix} = A_{rs}^{t} B\text{–}t \begin{bmatrix} E_{x,,,}^{i} \\ E_{y,,,}^{i} \\ E_{z,,,}^{i} \end{bmatrix} \qquad (9\text{–}125,a)$$

and

$$\begin{bmatrix} E_{\rho t}^{d} \\ E_{\theta t}^{d} \\ E_{\phi t}^{d} \end{bmatrix} = A_{rs} \begin{bmatrix} E_{xt}^{d} \\ E_{yt}^{d} \\ E_{zt}^{d} \end{bmatrix}$$

$$= A_{rs}\, B_{-t} \begin{bmatrix} E_{x}^{d,''' } \\ E_{y}^{d,''' } \\ E_{z}^{d,''' } \end{bmatrix} \qquad (9\text{–}125,b)$$

where A_{rs} is a rectangular to sherical coordinate transformation matrix and B_{-t} is a matrix given by:

$$B_{-t} = \begin{bmatrix} 0 & 1 & 0 \\ 0 & 0 & 1 \\ 1 & 0 & 0 \end{bmatrix}.$$

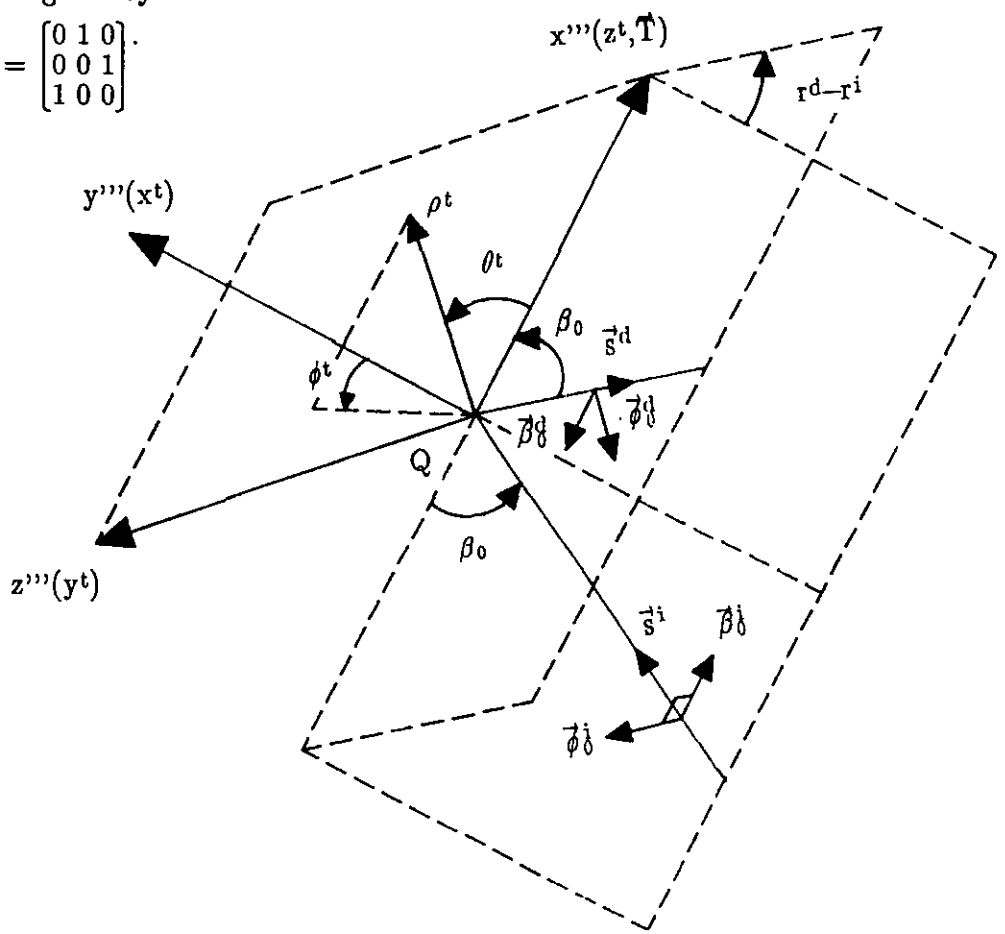

Fig. 9–9 The Incident and Diffracted Field Vectors in (x''',y''',z''') Coordinate System

9.3.2.4. Diffracted Field from the Diffraction Point

The relation between the vector components shown in Fig. 9–9 are:

$$E_{\phi_0}^{i} = -E_{\phi t}^{i} \tag{9–126,a}$$

$$E_{\beta_0}^{i} = -E_{\theta t}^{i} \tag{9–126,b}$$

and

$$E_{\phi t}^{d} = -E_{\phi_0}^{d} \tag{9–127,a}$$

$$E_{\theta t}^{d} = E_{\beta_0}^{d} \tag{9–127,b}$$

Similarly, by using the transformation matrices A_{sr}, A_{sr}^{t} (spherical to rectangular transformation):

$$\begin{bmatrix} E_{\rho}^{d} \\ E_{\theta}^{d} \\ E_{\phi}^{d} \end{bmatrix} = A_{rs} \begin{bmatrix} E_x^{d} \\ E_y^{d} \\ E_z^{d} \end{bmatrix}$$

$$= A_{rs}\, M \begin{bmatrix} E_{x}^{d,,} \\ E_{y}^{d,,} \\ E_{z}^{d,,} \end{bmatrix}$$

$$= A_{rs}\, M\, B^{t} \begin{bmatrix} E_{xt}^{d} \\ E_{yt}^{d} \\ E_{zt}^{d} \end{bmatrix}$$

$$= A_{rs}\, M\, B^{t}\, A_{sr}^{t} \begin{bmatrix} E_{\rho t}^{d} \\ E_{\theta t}^{d} \\ E_{\phi t}^{d} \end{bmatrix} \tag{9–128}$$

Since $E_{\rho_t}^d$ and $E_{\rho_t}^i$ are zero, it is possible to write (using Eq.(9–126) and Eq.(9–127)):

$$\begin{bmatrix} E_{\theta_t}^d \\ E_{\phi_t}^d \end{bmatrix} = \begin{bmatrix} E_{\beta_0}^d \\ -E_{\phi_0}^d \end{bmatrix} \tag{9–129,a}$$

and

$$\begin{bmatrix} E_{\beta_0}^i \\ E_{\phi_0}^i \end{bmatrix} = \begin{bmatrix} -E_{\theta_t}^i \\ -E_{\phi_t}^i \end{bmatrix} \tag{9–129,b}$$

so:

$$\begin{bmatrix} E_{\theta_t}^d \\ -E_{\phi_t}^d \end{bmatrix} = \begin{bmatrix} E_{\beta_0}^d \\ E_{\phi_0}^d \end{bmatrix}$$

$$= -\begin{bmatrix} D_s & 0 \\ 0 & D_h \end{bmatrix} \begin{bmatrix} E_{\beta_0}{}^i \\ E_{\phi_0}{}^i \end{bmatrix} \sqrt{\frac{\rho_c}{s^d(\rho_c+s^d)}}\, e^{-jks^d}$$

$$= -\begin{bmatrix} D_s & 0 \\ 0 & D_h \end{bmatrix} \begin{bmatrix} -E_{\theta_t}^i \\ -E_{\phi_t}^i \end{bmatrix} \sqrt{\frac{\rho_c}{s^d(\rho_c+s^d)}}\, e^{-jks^d} \tag{9–130}$$

Inserting Eq. (9–129) in Eq.(9–130), and the result in Eq.(9–128), the diffracted field can be obtained.

9.3.2.5. Total Radiation Pattern in an Arbitrary ϕ–plane

The total field in any observation angle θ is the sum of the direct field from the feed and the diffracted fields from the two diffraction points. In this way, the radiation pattern of an offset paraboloidal reflector antenna can be obtained in an arbitrary ϕ–plane.

10. The EEC Method for the Far–field Caustic in the Symmetry Plane

In Chapter 9, it is found that for an offset reflector configuration there is a far–field caustic in the symmetry plane at the angle $\theta=2\psi_{p0}$. Since the GTD (UTD) fails at caustics, the equivalent edge current method (EEC), described in Chapter 6, is employed to determine the field at and around this caustic.

In contrast to a symmetrical configuration, the equivalent edge current for a offset configuration is not flowing in the ξ–direction. In the next section expressions are derived for this edge current and the far–field induced by this current.

10.1 EEC for an Offset Configuration

According to the GTD (UTD), the diffracted field in a ray–fixed coordinate system consists of two components, $E_{\beta_0}^d$ and $E_{\phi_0}^d$ (see Fig. 9–7). Only the field components $E_{\beta_0}^d\sin\beta_0$ and $H_{\beta_0}^d\sin\beta_0$ will give a contribution in the T–direction (see Fig.10–1).So:

$$E_T^d=E_{\beta_0}^d\sin\beta_0 \qquad (10\text{–}1,a)$$

$$H_T^d=H_{\beta_0}^d\sin\beta_0$$

$$=\frac{1}{\eta}E_{\phi_0}^d\sin\beta_0 \qquad (10\text{–}1,b)$$

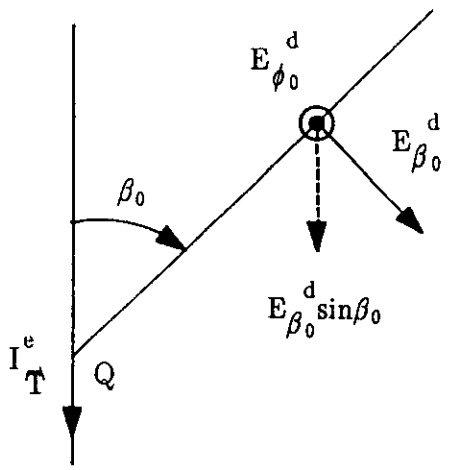

Fig.10–1 Equivalent Edge Current

Using Eq.(6–3) and Eq.(6–5) for the fields at the edge of the reflector results in:

$$I_T^e = -\frac{2\sqrt{2\pi k}}{\eta k} e^{-j\pi/4} E_{\beta_0}^d \sin\beta_0 \qquad (10\text{–}2,a)$$

$$I_T^m = -\frac{2\sqrt{2\pi k}}{k} e^{-j\pi/4} E_{\phi_0}^d \sin\beta_0 \qquad (10\text{–}2,b)$$

The far–field induced by these edge currents is obtained by using the formulas given by Silver [1]:

$$\vec{E}^e(r,\theta,\phi) = -j\frac{k\eta}{4\pi r} e^{-jkr} \int_l [\vec{I}^e - (\vec{I}^e \cdot \vec{r})\vec{r}] e^{jk\rho\vec{\rho}\cdot\vec{r}}\, dl \qquad (10\text{–}3,a)$$

$$\vec{H}^m(r,\theta,\phi) = -j\frac{k/\eta}{4\pi r} e^{-jkr} \int_l [\vec{I}^m - (\vec{I}^m \cdot \vec{r})\vec{r}] e^{jk\rho\vec{\rho}\cdot\vec{r}}\, dl \qquad (10\text{–}3,b)$$

Inserting Eq.(10–2) in Eq.(10–3) gives:

$$\begin{bmatrix} E_\theta^e \\ E_\phi^e \end{bmatrix} = -j\frac{k\eta}{4\pi r} e^{-jkr} \int_l \begin{bmatrix} I_{T\theta}^e \\ I_{T\phi}^e \end{bmatrix} e^{jk\rho\vec{\rho}\cdot\vec{r}}\, dl \qquad (10\text{–}4,a)$$

$$\begin{bmatrix} H_\theta^m \\ H_\phi^m \end{bmatrix} = -j\frac{k/\eta}{4\pi r} e^{-jkr} \int_l \begin{bmatrix} I_{T\theta}^m \\ I_{T\phi}^m \end{bmatrix} e^{jk\rho\vec{\rho}\cdot\vec{r}}\, dl \qquad (10\text{–}4,b)$$

where

$$\vec{E}^e(r,\theta,\phi) = \begin{bmatrix} 0\ \vec{r} \\ E_\theta^e\ \vec{\theta} \\ E_\phi^e\ \vec{\phi} \end{bmatrix} \qquad (10\text{–}5,a)$$

$$\vec{H}^m(r,\theta,\phi)=\begin{bmatrix} 0\ \vec{r} \\ H_\theta^m\ \vec{\theta} \\ H_\phi^m\ \vec{\phi} \end{bmatrix} \tag{10–5,b}$$

and

$$\vec{I}_T^e=\begin{bmatrix} I_{Tr}^e\ \vec{r} \\ I_{T\theta}^e\ \vec{\theta} \\ I_{T\phi}^e\ \vec{\phi} \end{bmatrix} \quad \vec{I}_T^m=\begin{bmatrix} I_{Tr}^m\ \vec{r} \\ I_{T\theta}^m\ \vec{\theta} \\ I_{T\phi}^m\ \vec{\phi} \end{bmatrix} \tag{10–6}$$

From Eq. (10–4), it is possible to obtain:

$$\begin{bmatrix} E_\theta^e \\ E_\phi^e \end{bmatrix} = -j\frac{k\eta}{4\pi r} e^{-jkr} \int_l \begin{bmatrix} I_{T\theta}^e \\ I_{T\phi}^e \end{bmatrix} e^{jk\rho\vec{\rho}\cdot\vec{r}}\, dl \tag{10–7,a}$$

$$\begin{bmatrix} E_\theta^m \\ E_\phi^m \end{bmatrix} = \eta \begin{bmatrix} H_\phi^m \\ -H_\theta^m \end{bmatrix}$$

$$= -j\frac{k}{4\pi r} e^{-jkr} \int_l \begin{bmatrix} I_{T\phi}^m \\ -I_{T\theta}^m \end{bmatrix} e^{jk\rho\vec{\rho}\cdot\vec{r}}\, dl \tag{10–7,b}$$

The total field will be the sum of the field induced by the equivalent edge current and the direct incident field from the feed in case no blockage occurs:

$$\begin{bmatrix} E_\theta \\ E_\phi \end{bmatrix} = \begin{bmatrix} E_\theta^e \\ E_\phi^e \end{bmatrix} + \begin{bmatrix} E_\theta^m \\ E_\phi^m \end{bmatrix} + \begin{bmatrix} E_{f\theta}^i \\ E_{f\phi}^i \end{bmatrix}$$

$$= -j\frac{k\eta}{4\pi r} e^{-jkr} \int_l \begin{bmatrix} I_{T\theta}^e + I_{T\phi}^m/\eta \\ I_{T\phi}^e - I_{T\theta}^m/\eta \end{bmatrix} e^{jk\rho\vec{\rho}\cdot\vec{r}}\, dl + \begin{bmatrix} E_{f\theta}^i \\ E_{f\phi}^i \end{bmatrix} \tag{10–8}$$

11. Numerical Results and Discussions

11.1 Offset Configuration

The calculation methods described in the previous chapters have been applied to the offset configuration shown in Fig. 11–1.

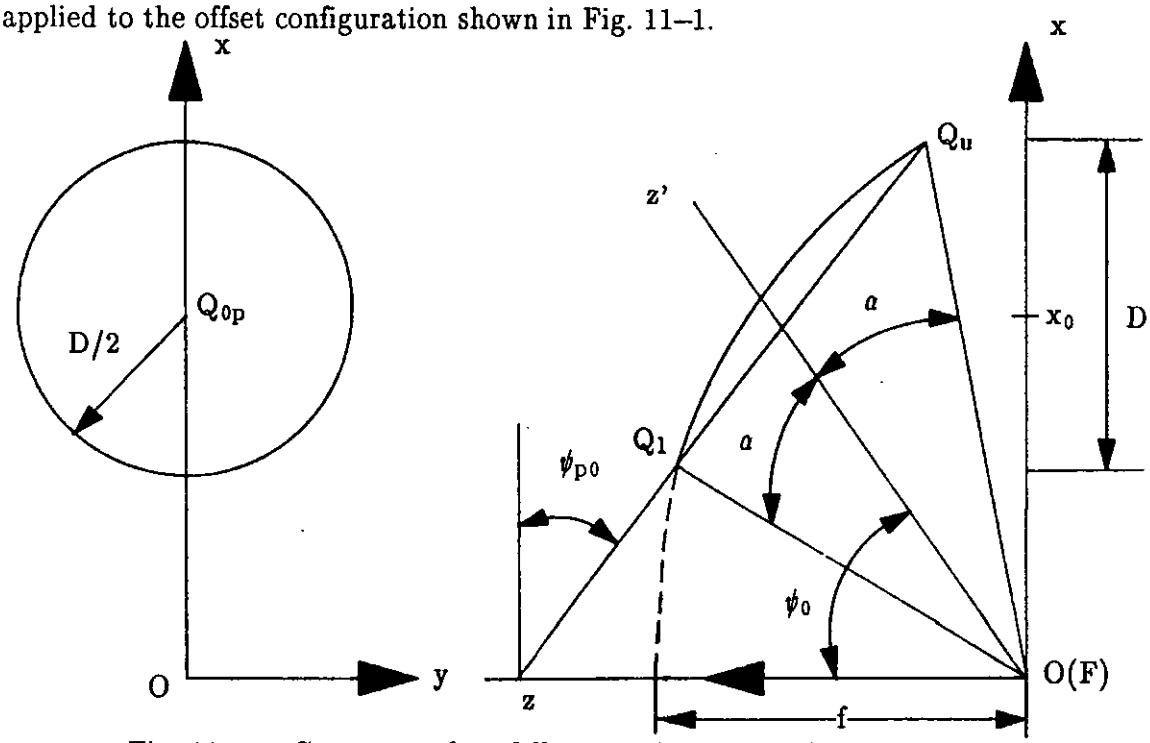

Fig. 11–1 Geometry of an Offset Paraboloidal Reflector Antenna

The system parameters used being $\psi_0=45^0$ and $a=30^0$ which results in $\psi_{p0}=24.2^0$ and f/D=0.79. The feed has a power radiation function of the form given by Eq.(2–4) with n=2, and the polarization properties of a Huygens source with x'– or y'–axis polarization.

11.2. Numerical Results

Using GTD (UTD) as described in the previous chapters, the power radiation pattern in the symmetry and asymmetry planes, were calculated for x'–axis polarization. They are shown in Fig. 11–2(a) and Fig. 11–2(b), respectively.

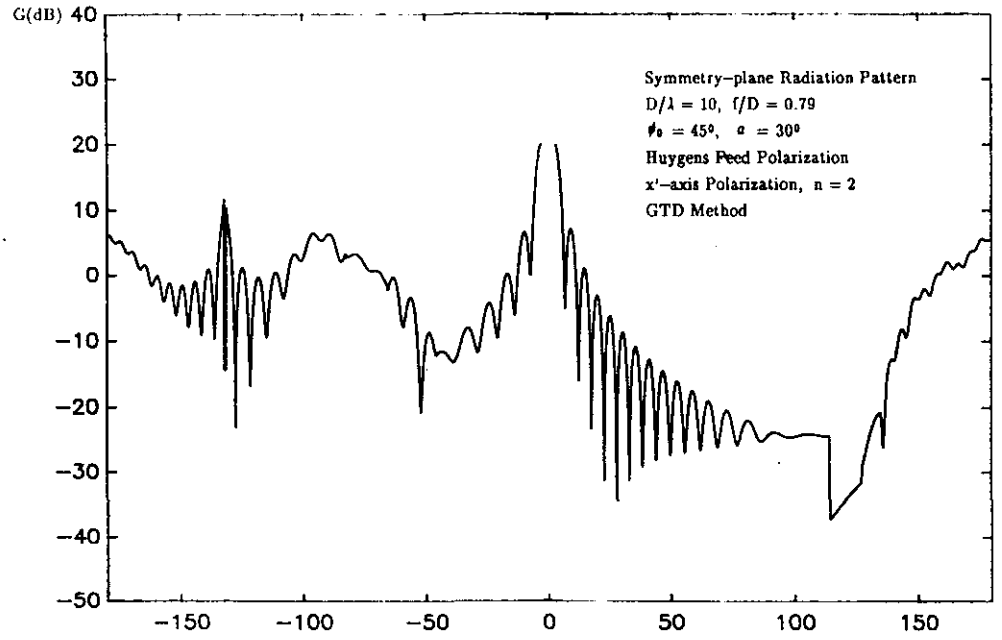

Fig 11–2(a) Symmetry Plane Far–field Radiation Pattern of an Offset Paraboloidal Reflector Antenna

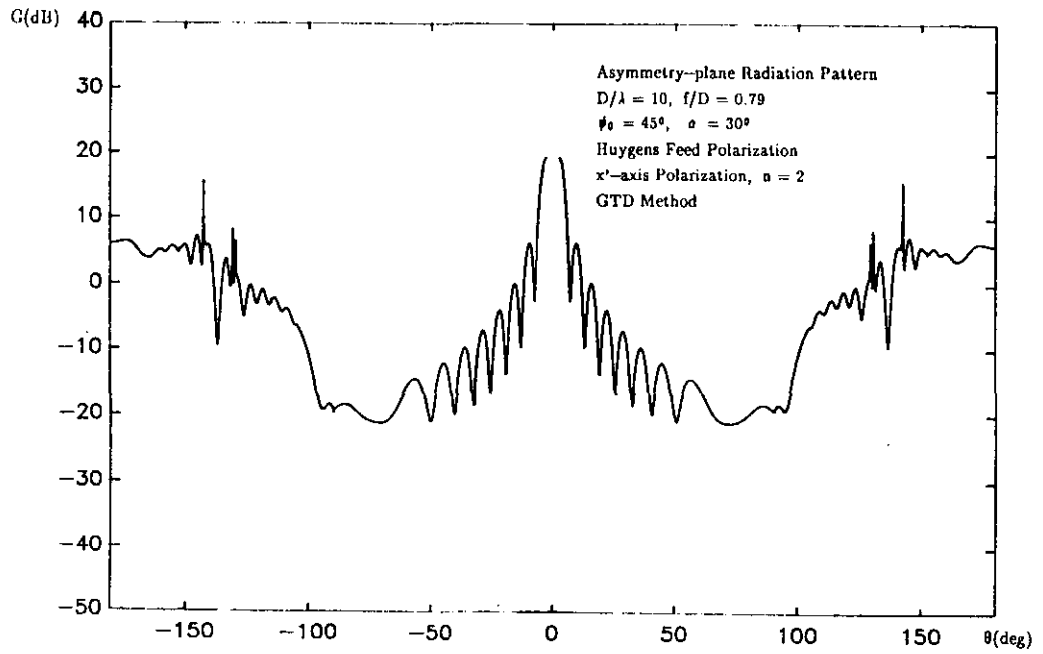

Fig. 11–2(b) Asymmetry Plane Far–field Radiation Pattern of an Offset Paraboloidal Reflector Antenna

The horizontal axis is the far–field observation angle measured from the forward–direction of the reflector antenna. The notation $\theta<0$ indicates the half plane where $\phi=0$ for the symmetry plane or $\phi=\pi/2$ for the asymetry plane; $\theta>0$ indicates the half plane where $\phi=\pi$ for the symmetry plane or $\phi=3\pi/2$ for the asymmetry plane. The vertical axis is the gain function in dB.

From the patterns shown in Fig. 11–2, it can be observed that there are some discontinuities, especially for the E–plane radiation pattern in the angle region $110^0<\theta<130^0$ and at $\theta\approx-132^0(2\theta_{p0}-180^0)$. The discontinuities in the H–plane are discussed seperately in the next section.

The discontinuities in the region $110^0<\theta<130^0$ are caused by the blocking effects of the reflector on one of the edge diffracted rays. Taking the surface diffracted rays into consideration, a smoother pattern will be obtained (see Fig. 11–3).

The discontinuity at the angle $\theta=2\psi_{p0}-180^0$ is in the direction of one of the caustics. Since the GTD (UTD) method fails at caustics, the EEC method is used in the caustic region. As an example the radiation patterns calculated by GTD (UTD) and EEC are compared in the near–caustic angle region in Fig. 11–4 for a antenna system with $D/\lambda=10$ and $n=2$. The transition angle θ_{GE} between the GTD and EEC for this caustic region is shown in Fig. 11–5 as a function of D/λ. Again, this angle is almost inversly proportional to D/λ. The transition angle is independent of the n of the feed function for the same reason as with the symmetrical antenna. The complete E–plane radiation pattern, including the EEC results for the caustic is plotted in Fig. 11–6.

Due to the focussing properties of the parabolic antenna, the forward–direction, $\theta=0$, is also a far–field caustic. Here, the PO is used to calculate the radiation pattern. The results in this region calculated by the GTD (UTD) and the PO are given in Fig. 11–7. The calculation shows that PO removes the singularity in the forward–direction and the PO and GTD patterns agree well away from this caustic direction. The D/λ dependence of the transition angle θ_{GP} is shown in Fig. 11–8. Again the dependence of the feed function n is neglectable.

Using the modified GTD (UTD) for the wide–angle region pattern calculation, and the EEC and PO in or near the caustic directions, the complete radiation pattern shown in Fig.11–9 for an offset reflector antenna with x'–axis feed polarization is obtained finally. Fig.11–10 shows similar patterns for y'–axis polarization. Finally, Fig. 11–11 shows the patterns for an antenna with the same geometry but a large D/λ (=72).

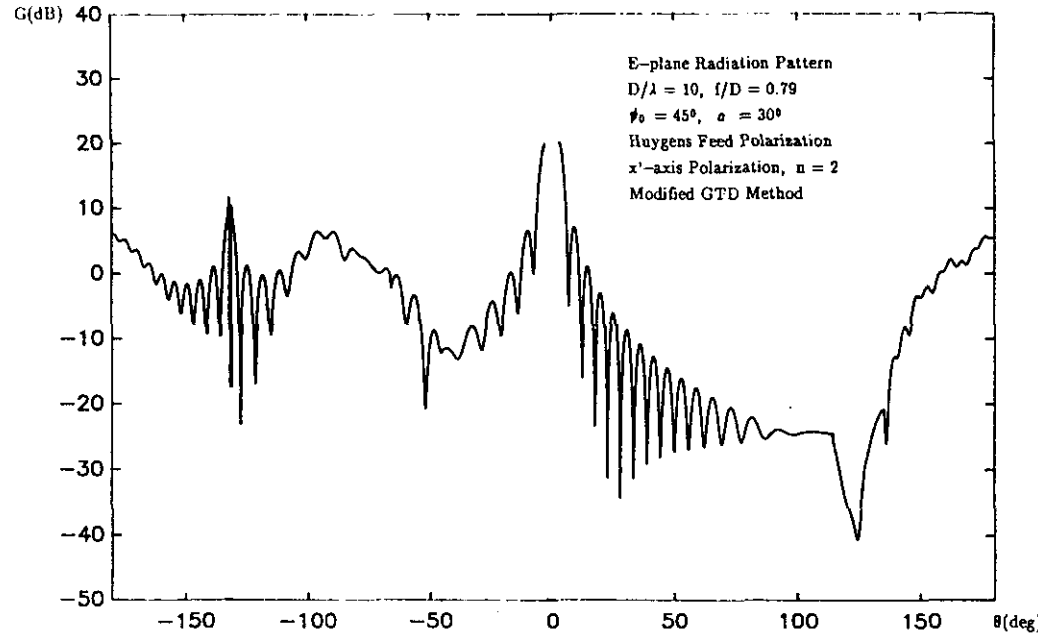

Fig. 11–3(a) Symmetry Plane Far–field Radiation Pattern of an Offset Paraboloidal Reflector Antenna

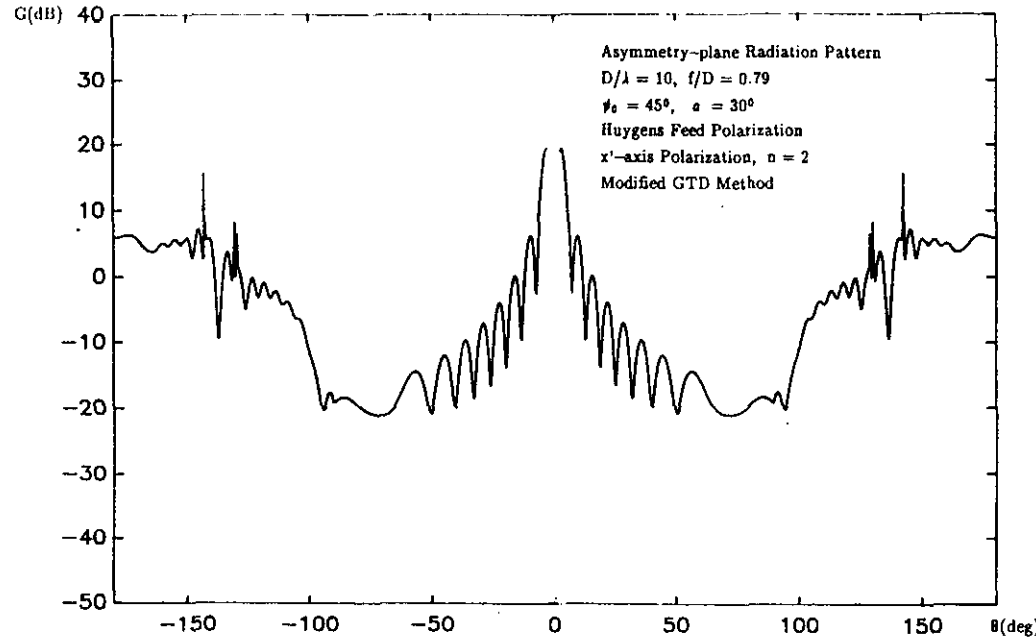

Fig. 11–3(b) Asymmetry Plane Far–field Radiation Pattern of an Offset Paraboloidal Reflector Antenna

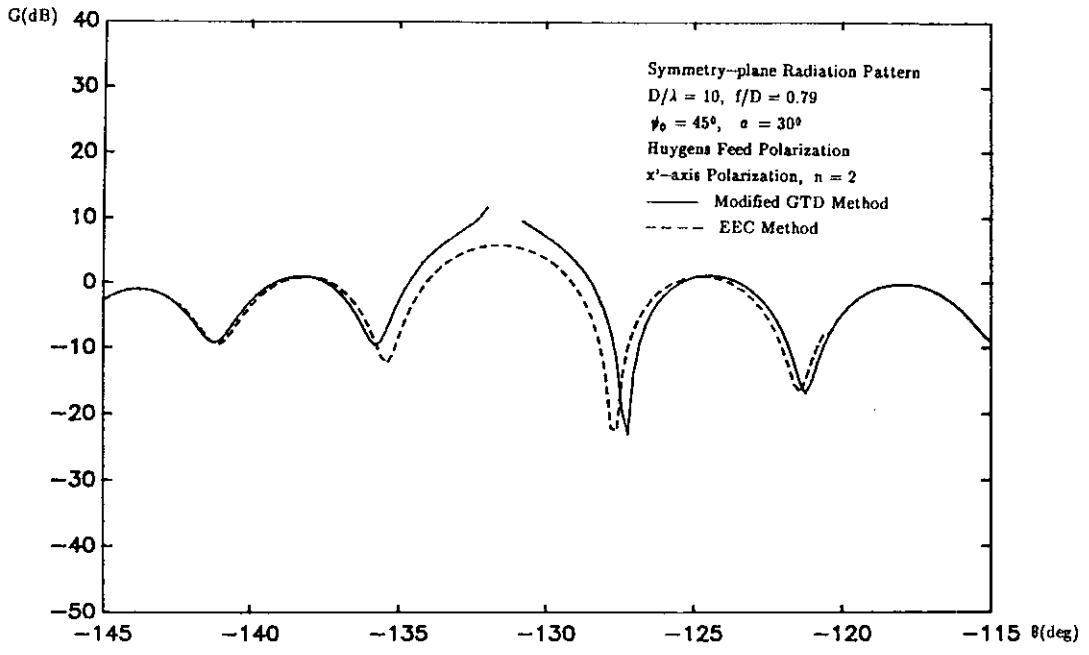

Fig. 11–4 Comparison of the Symmetry Plane Far–field Radiation Pattern of an Offset Paraboloidal Reflector Antenna in the Caustic Region using GTD or EEC

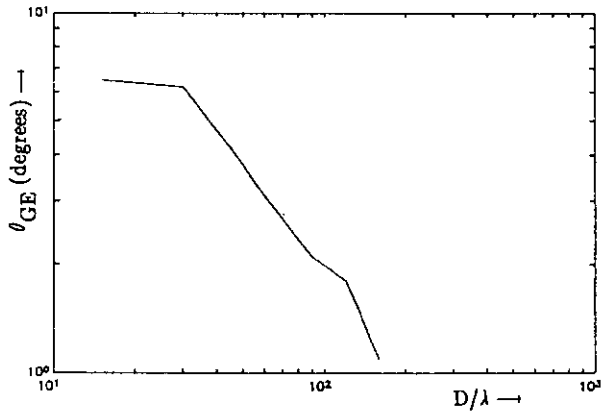

Fig 11–5 The Transition angle θ_{GE} as a Function of D/λ (n=2).

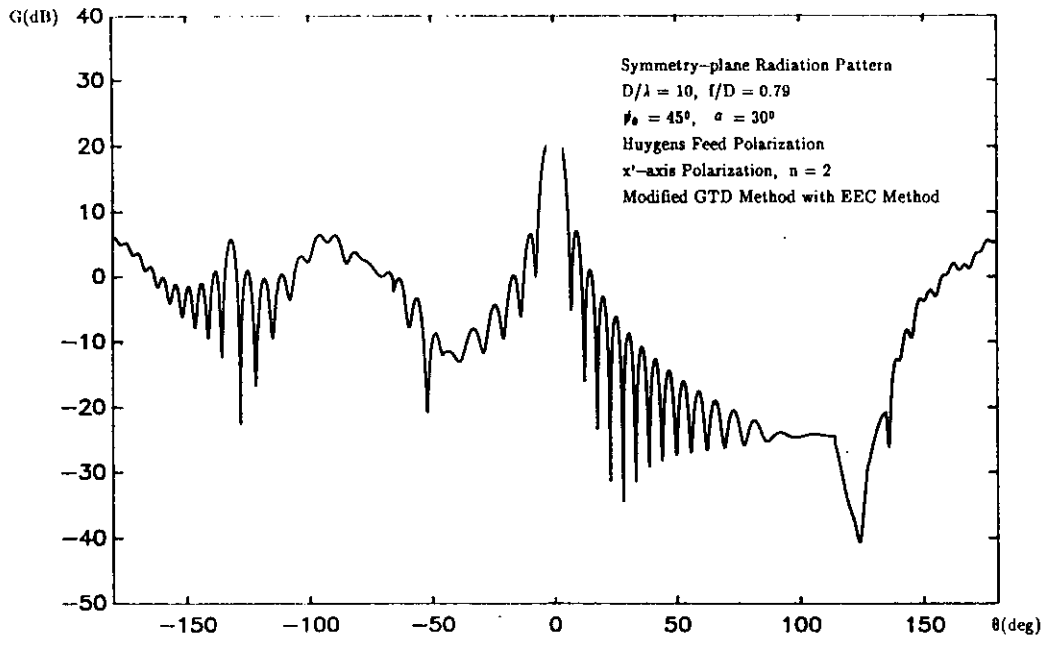

Fig. 11–6 Symmetry Plane Far–field Radiation Pattern of an Offset Paraboloidal Reflector Antenna Including the EEC Method

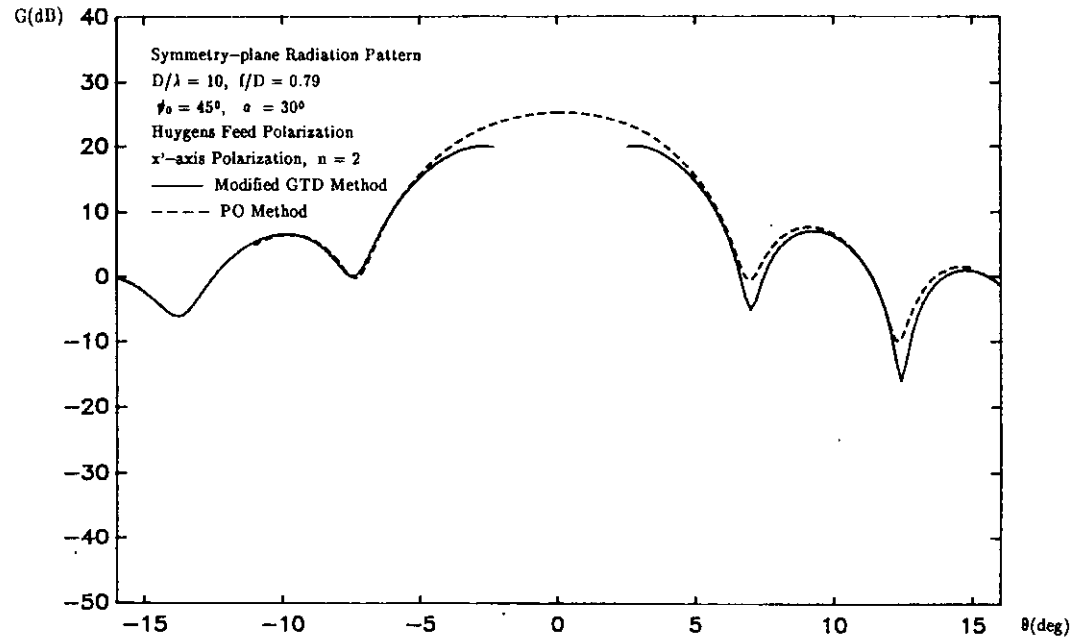

Fig. 11–7(a) Comparison of the Symmetry Plane Far–field Radiation Pattern of an Offset Paraboloidal Reflector Antenna in the Antenna Forward Direction using GTD or PO

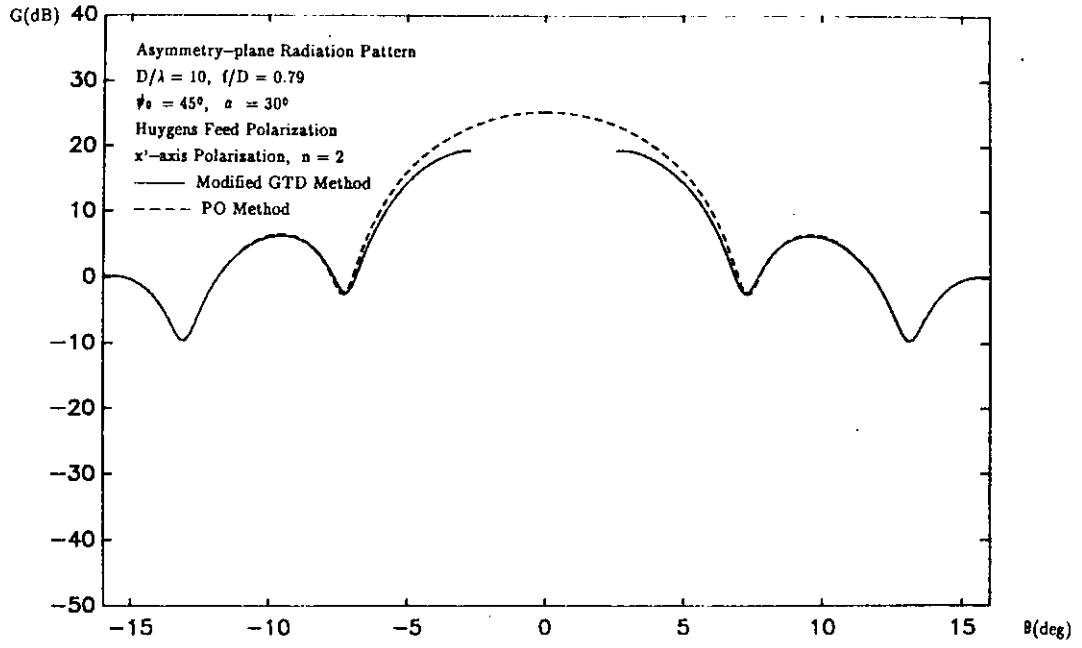

Fig. 11–7(b) Comparison of the Asymmetry Plane Far–field Radiation Pattern of an Offset Paraboloidal Reflector Antenna in the Antenna Forward Direction using GTD or PO

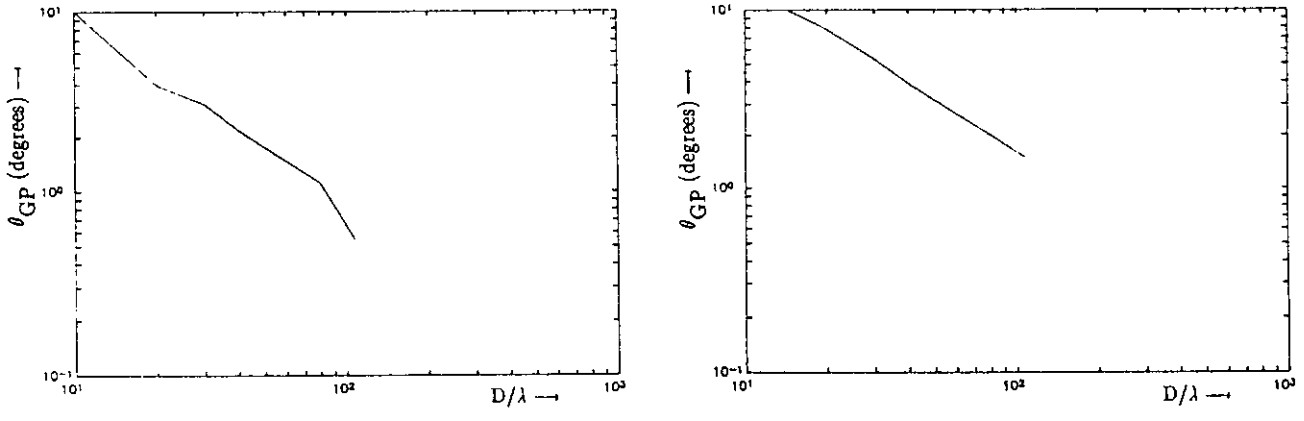

(a) (b)

Fig.11–8 The Transition Angle θ_{GP} as a Function of D/λ (n=2).
(a): E–plane (b): H–plane

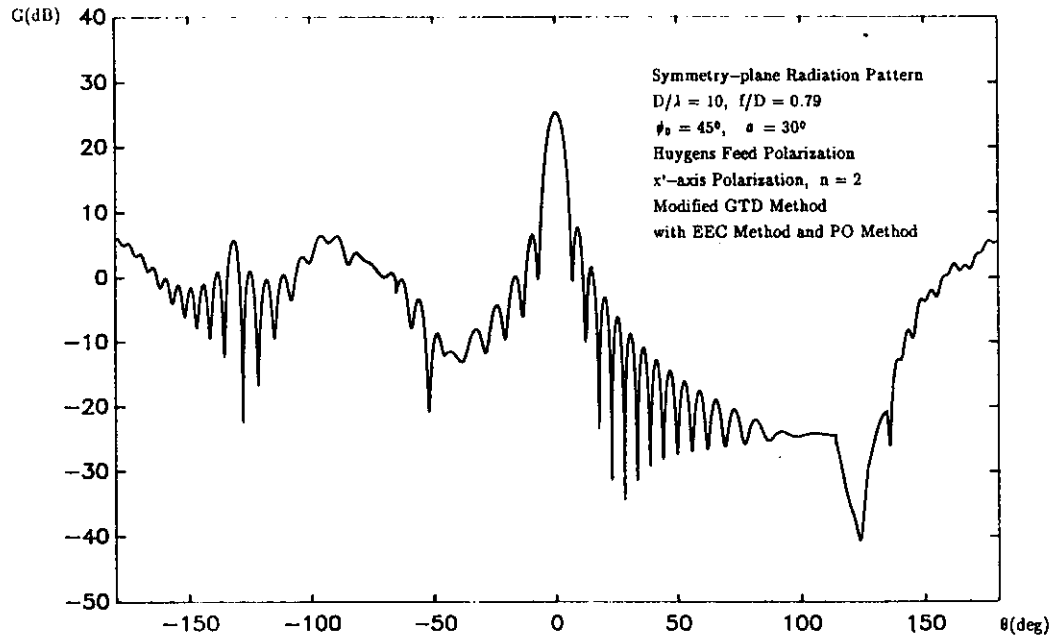

Fig. 11–9(a) Complete Far–field Radiation Pattern in the Symmetry Plane of an Offset Paraboloidal Reflector Antenna

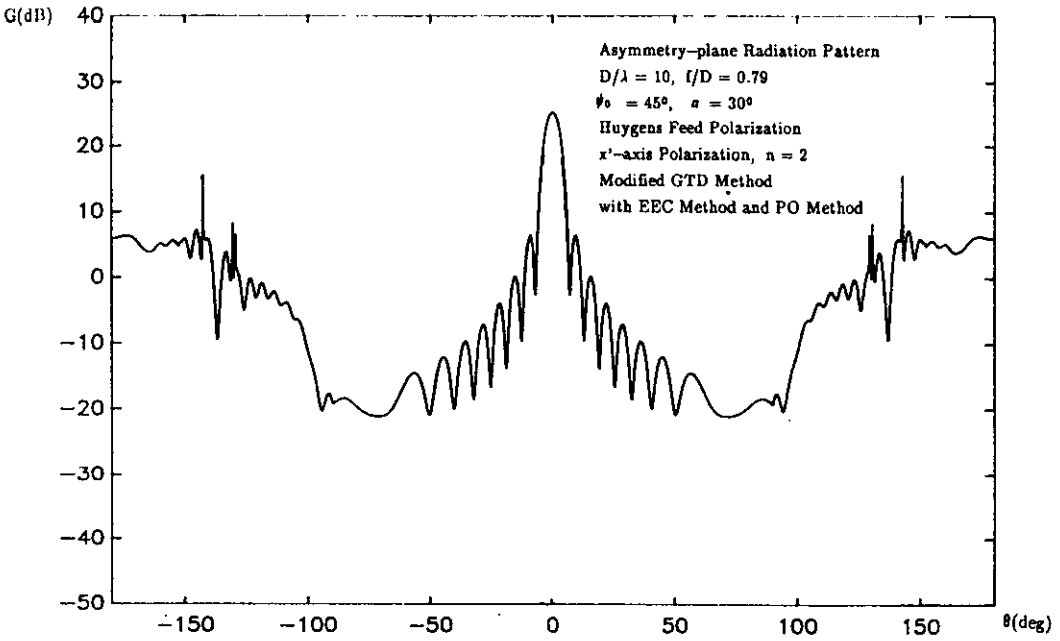

Fig. 11–9(b) Complete Far–field Radiation Pattern in the Asymmetry Plane of an Offset Paraboloidal Reflector Antenna

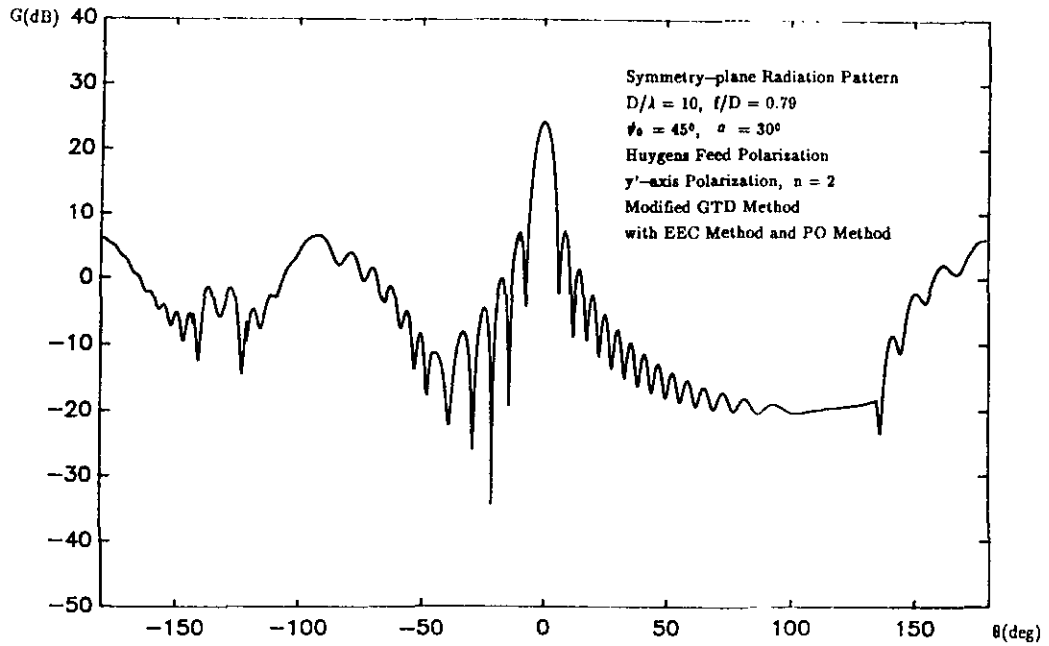

Fig. 11–10(a) Complete Far–field Radiation Pattern in the Symmetry Plane of an Offset Paraboloidal Reflector Antenna (y'–axis polarization)

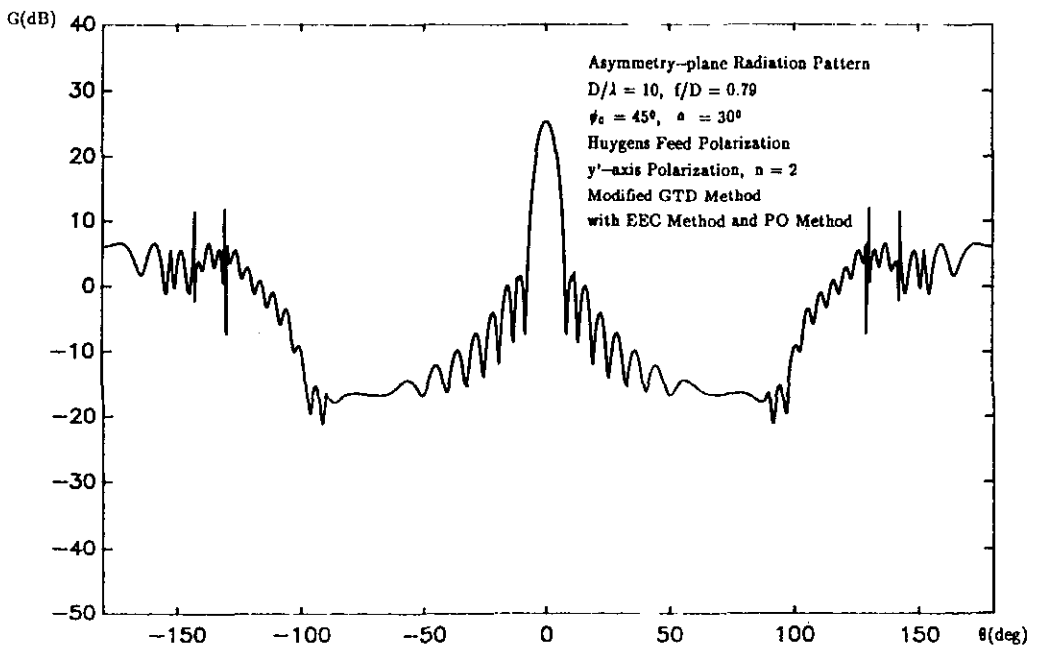

Fig. 11–10(b) Complete Far–field Radiation Pattern in the Asymmetry Plane of an Offset Paraboloidal Reflector Antenna (y'–axis polarization)

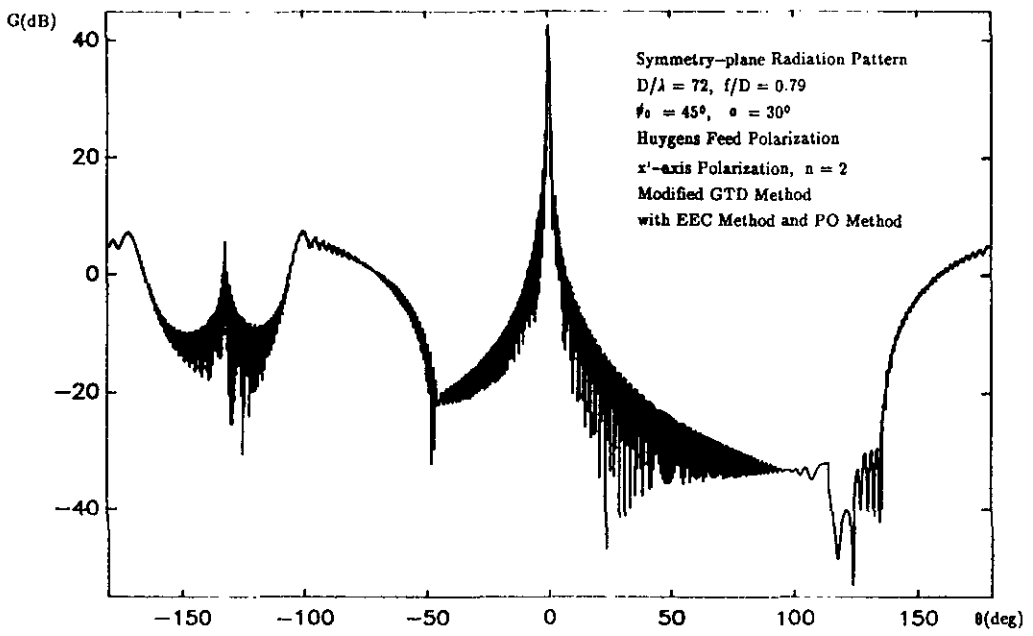

Fig. 11–11(a) Complete Far–field Radiation Pattern in the Symmetry Plane of an Offset Paraboloidal Reflector Antenna ($D/\lambda = 72$)

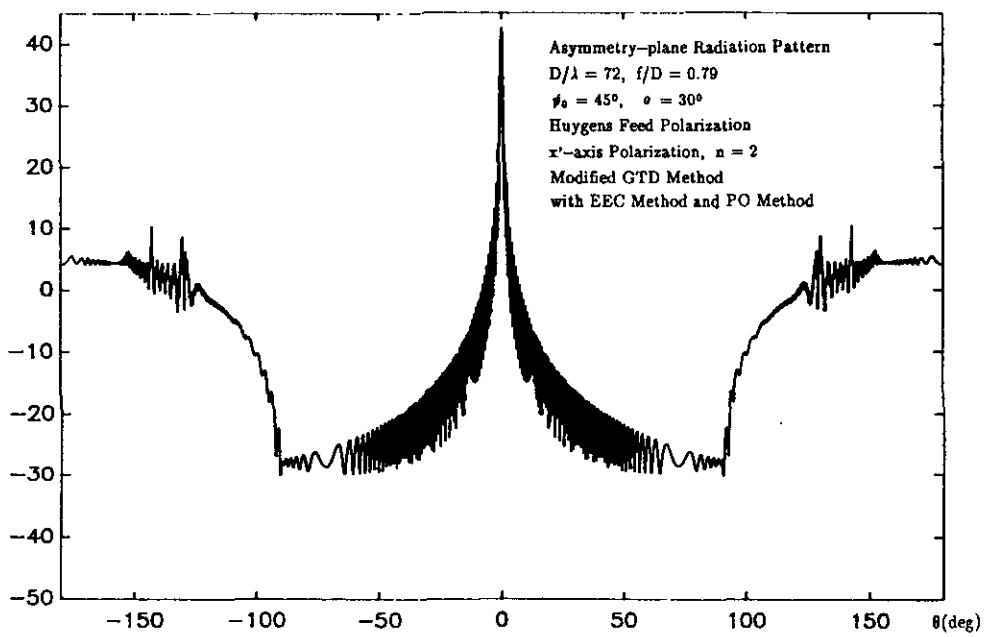

Fig. 11–11(b) Complete Far–field Radiation Pattern in the Asymmetry Plane of an Offset Paraboloidal Reflector Antenna ($D/\lambda = 72$)

11.3 Pattern Discontinuities

As can be seen from the radiation patterns presented in the previous section discontinuities appear in the asymmetry plane ($\phi=\pi/2$) at some specific far–field observation angles. The same is observed in Fig. 11–13, where the radiation pattern for the plane $\phi=\pi/3$ is shown. The discontinuity in the forward direction has already been explained. The other discontinuities are caused by the fact that at these specific θ–angles, the ρ_c(Eq.(4–4)) of one of the edge diffracted rays becomes infinitely large. This means that the second caustic of that ray (the first caustic is at the edge) is at infinity (the far–field region). The GTD method will not apply at this far–field point because it is a caustic point in the sense the calculated gain function g(θ). The explanation for this is that not a spherical wave but a cylindrical wave originates from the edge point. Fig. 11–12 shows the position of the second caustic points on the diffraction cone as a function of ϕ for a certain edge diffraction point. It shows that the caustic distance becomes infinitely large for a particular ϕ–plane.

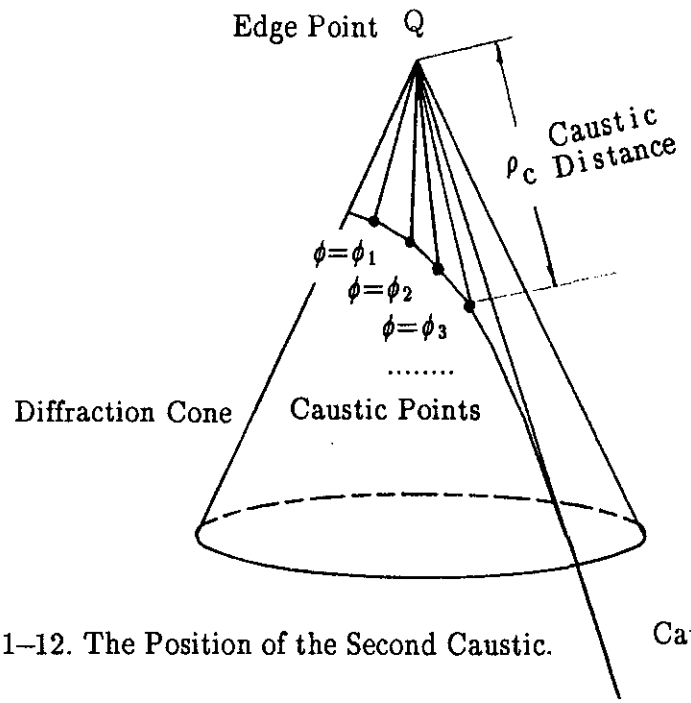

Fig. 11–12. The Position of the Second Caustic.

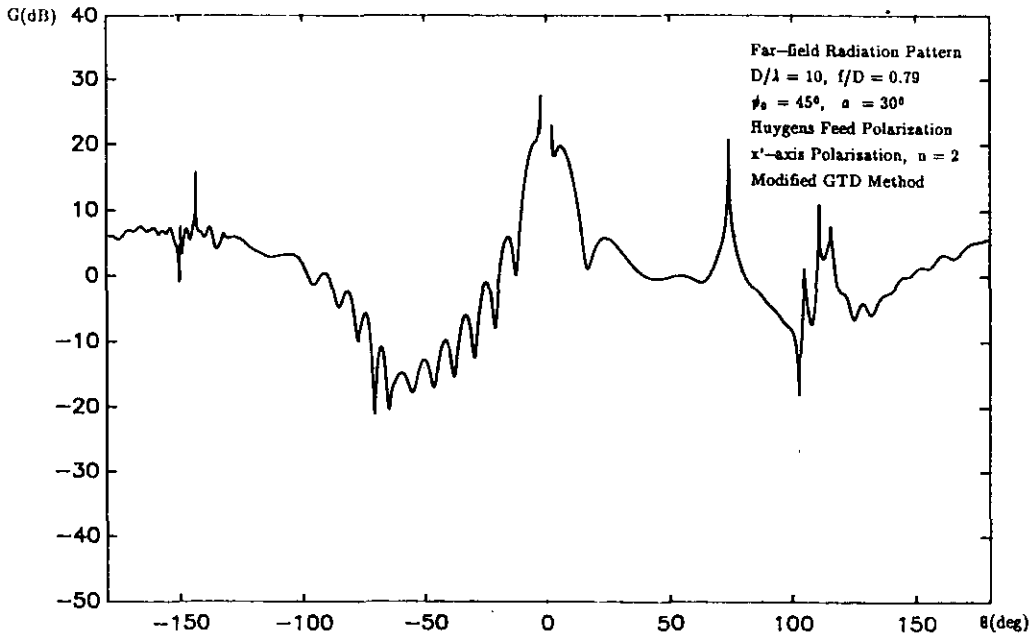

Fig. 11–13 Far–field Radiation Pattern of an Offset Paraboloidal Reflector Antenna in the Plane $\phi=\pi/3$.

For the pattern calculation in an arbitrary ϕ–plane, the θ angles where ρ_c becomes infinitely large can be calculated. The results are shown in Fig. 11–14.

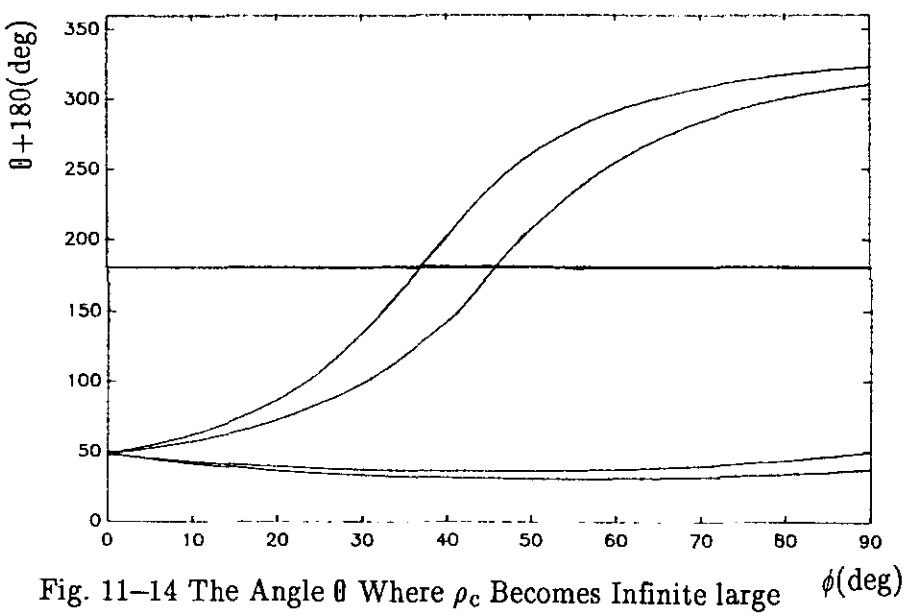

Fig. 11–14 The Angle θ Where ρ_c Becomes Infinite large as a Function of ϕ.

Since EEC is has been used successfully in this report for far–field caustic directions where all the diffraction points have $\rho_c=\infty$ and make in phase contributions to the far–field in the caustic direction, it is perhaps possible to use a modified EEC method for the angles where the discontinuities appear. For the standard EEC, the caustic divergence factor is taken to be:

$$A(\rho_c,s^d) = \sqrt{\frac{\rho_c}{s^d(\rho_c+s^d)}} \overset{\rho_c\to\infty}{\Rightarrow} \sqrt{\frac{1}{s^d}} \qquad (11\text{–}1)$$

The modified EEC–method should take into account any change in the caustic divergence factor for a part of the edge and modify the equivalent edge current accordingly.

12 Conclusions

In the first part of this report, high–frequency asymptotic techniques for determining the wide–angle far–field radiation patterns of axially symmetrical parabolic reflector antennas are reviewed. The asymptotic techniques considered were GTD, UTD, APO and CAPO. The far–field derived with these methods consists of the field coming directly from the feed, as well as the reflected and diffracted field contributions from the reflector. It appears that, for calculating the diffracted field contributions, the two–dimensional diffraction model is sufficient because of the axial–symmetry of the antenna system. The mathematical formulae describing the total far–field were derived for the different calculation techniques. By doing this, some conflicting statements in literature, associated with the validity of the methods in different regions, have been clarified.

Starting with Keller's GTD, it is shown that if Kouyoumjian's modified diffraction coefficients are used, and if the surface diffracted rays are included, continuous radiation patterns for the wide–angle region will be obtained when using this modified GTD (UTD) method.

From a comparison between the radiation patterns calculated by the GTD (UTD) and APO methods, it was found that they differed in the shadow region especially. This is explained by the incorrect nature of the edge currents used in APO. To compensate for this deficit, the corrected APO (CAPO) was suggested by Knop and Ostertag [8]. The patterns calculated with CAPO and GTD (UTD) appear to be almost identical. However, the CAPO method needs more computing time than the GTD (UTD) method, because more complicated mathematical formulas are involved in CAPO.

The pattern in the forward– and rear–axial region can be obtained with the PO and EEC methods, respectively, because the high–frequency asymptotic techniques will fail in those far–field caustic directions. It was shown that there is a smooth transition between PO, GTD(UTD) and EEC.

So, the conclusion from the first part of the report is that complete radiation patterns can be obtained using of the modified GTD (UTD) for the wide–angle region, and the PO and EEC in or near the two caustic directions. The results hold for a symmetrical parabolic reflector antenna configuration, when the effects of feed and support strut blockage are not taken into account.

The second part of the report deals with the far–field analysis of a reflector antenna configuration which is free from aperture blockage. It is shown that for such

an offset–reflector antenna, both the two– and three–dimensional diffraction models are needed to calculate the complete radiation pattern. For the symmetry plane ($\phi = 0^0$), the two–dimensional GTD (UTD) model which includes the surface diffracted fields, gives smooth patterns for the wide–angle regions. Besides a far–field caustic in the forward direction, a second caustic was found in the symmetry plane at a specific angle which is completely determined by the offset–parameters. For valid results in these near–caustic angle regions, PO and EEC had to be used. Again, a smooth transition was found between the three different methods.

For calculating the radiation pattern in the other ϕ–planes, the three–dimensional diffraction model was needed because the incident rays are generally not normal to the tangent of the reflector edge. Patterns from the three–dimensional model showed some discontinuities, which were due to the fact that the caustic distance of one of the two edge diffracted rays became infinitely large. The angles where this phenomenon occur can be calculated and the corresponding plots have been shown in this report.

So, from the theoretical analyses and the numerical calculations presented in the second part of this report, it was concluded that GTD (UTD) is a valid method for predicting the wide–angle radiation pattern in the symmetry plane of an offset reflector antenna and it can be used for any arbitrary plane except some specific angle regions where the caustic distance of one of the diffracted rays becomes very large. In those angle regions, contributions to the far–field come from a part of the reflector edge around that diffraction point, therefore it seems likely that a modified EEC method can be used to obtain a smooth radiation pattern in any arbitrary ϕ–plane.

References

1. Silver, S.
MICROWAVE ANTENNA THEORY AND DESIGN.
London: Peter Peregrinus, 1984.

2. Collin, R.E. and F.J. Zucker
ANTENNA THEORY.
New York: McGraw–Hill, 1969.

3. Balanis, C.A.
ANTENNA THEORY – ANALYSIS AND DESIGN.
New York: John Wiley, 1982.

4. Rusch, W.V.T. and P.D. Potter
ANALASIS OF REFLECTOR ANTENNAS.
New York: McGraw–Hill, 1969.

5. James, G.L.
GEOMETRICAL THEORY OF DIFFRACTION FOR ELECTROMAGNETIC WAVES.
London: Peter Peregrinus, 1976.

6. Kouyoumjian, R.G. and P.H. Pathak
AN UNIFORM GEOMETRICAL THEORY OF DIFFRACTION FOR AN EDGE IN A PERFECTLY CONDUCTING SURFACE.
Proc. IEEE, Vol. 62 (1974), p.1448–1461.

7. Rusch, W.V.T.
PHYSICAL–OPTICS DIFFRACTION COEFFICIENTS FOR A PARABOLOID.
Electron. Lett., Vol. 10 (1974), p. 358–360.

8. Knop, C.P., and E.L. Ostertag
A NOTE ON THE ASYMPTOTIC PHYSICAL OPTIC SOLUTION TO SCATTERED FIELDS FROM A PARABOLOIDAL ANTENNA.
IEEE Trans. Antennas Propag., Vol. AP–25 (1977), p.531–534.

9. Ryan, C. E. and L. Peter
EVALUATION OF EDGE–DIFFRACTED FIELDS INCLUDING EQUIVALENT CURRENTS FOR THE CAUSTIC REGIONS.
IEEE Trans. Antennas Propag., Vol. AP–17 (1969), p.292–299 (see also the Correction, Vol. AP–18 (1970), p.275).

10 James, G.L. and V. Kerdemelidis
REFLECTOR ANTENNA RADIATION PATTERN ANALYSIS BY EQUIVALENT EDGE CURRENTS.
IEEE Trans. Antennas Propag., Vol.AP–21 (1973), p. 19–24 (see also the comments, Vol. AP–21 (1973), p.756).

11. Knott, E.F. and T.B.A. Senior
EQUIVALENT CURRENTS FOR A RING DISCONTINUITY.
IEEE Trans. Antennas Propag., Vol. AP–21 (1973), p.693–695.

12. Keller, J.B.
GEOMETRICAL THEORY OF DIFFRACTION.
Journal of the Optical Society of America, Vol. 52 (1962), p.116–130.

13. Keller, J.B.
DIFFRACTION BY AN APERTURE.
Journal of Applied Physics, Vol. 28 (1957), p.426–444.

14. Rusch, W.V.T.
ANTENNA NOTES.
Electromagnetics Institute, Technical University of Denmark, Lyngby, NB84, 1974, vol. II.

15. Knop, C.P.
AN EXTENSION OF RUSCH'S ASYMPTOTIC PHYSICAL OPTICS DIFFRACTION THEORY OF A PARABOLOID ANTENNA.
IEEE Trans. Antennas Propag., Vol. AP–23 (1975), p.741–743.

16. Engelhart, N. J. M.
FROM COMMUNICATION ANTENNA TO RADIOMETRY ANTENNA.
M.Sc.Thesis. Telecommunications Division, Faculty of Electrical Engineering, Eindhoven University of Technology, 1990.

17. Safak, M.
CALCULATION OF RADIATION PATTERNS OF REFLECTOR ANTENNAS BY HIGH–FREQUENCY ASYMPTOTIC TECHNIQUES.
Eindhoven: Department of Electrical Engineering, Eindhoven University of Technology, 1976, TH–Report 76–E–62.

18. Ratnasiri, P.A.J., and R.G. Kouyoumjian, P.H. Pathak
THE WIDE ANGLE SIDE LOBES OF REFLECTOR ANTENNAS.
Columbus: Electroscience Lab., Ohio State Univ., March 1970, Technical Rep.2183–1.

19. Kouyoumjian, R.G.
NUMERICAL AND ASYMPTOTIC TECHNIQUES IN ELECTROMAGNETICS.
Ed. by R. Mittra, Berlin: Springer, 1975. Ch. 6, p.166–213.

20. Rudge, A. W. and N.A. Adatia
OFFSET–REFLECTOR ANTENNAS: A REVIEW.
Proc. IEEE, Vol. 66 (1978), p. 1592–1816.

21. Cook, J. S., and E.M. Elam, H. Zucker
THE OPEN CASSEGRAIN ANTENNA: PART I ELECTROMAGNETIC DESIGN AND ANALYSIS.
Bell System Technical Journal, Vol. 44 (1965), p. 1255–1300.

22. Peters, L. and T.E. Kiloyne
RADIATING MECHANISMS IN A REFLECTOR ANTENNA SYSTEM.
IEEE Trans. Antennas Propag., Vol. AP—13 (1965), p. 368—374.

23. Ierley, W. H. and H. Zucker
A STATIONARY PHASE METHOD FOR THE COMPUTATION OF THE FAR FIELD OF OPEN CASSEGRAIN ANTENNAS.
Bell System Technical Journal, Vol. 49 (1970), p. 431—454.

24. Rahmat Samii, Y.
USEFUL COORDINATE TRANSFORMATION FOR ANTENNA APPLICATION.
IEEE Trans. Antennas Propag., Vol. AP—27 (1979), p. 571—574.

25. Jiahai, C.
WIDE—ANGLE RADIATION PATTERN CALCULATION OF PARABOLOIDAL REFLECTOR ANTENNAS: A COMPARATIVE STUDY.
Eindhoven: Faculty of Electrical Engineering, Eindhoven University of Technology, Telecommunications Division Report, 1990.

26. Jiahai, C. and de Maagt P.J.I.
WIDE—ANGLE RADIATION PATTERN CALCULATION OF OFFSET PARABOLOIDAL REFLECTOR ANTENNAS USING GTD AND EEC.
Eindhoven: Faculty of Electrical Engineering, Eindhoven University of Technology, Telecommunications Division Report, 1991.

27. Safak, M.
COMPLETE RADIATION PATTERN OF A FOCUS—FED OFFSET PARABOLOIDAL REFLECTOR.
Proc. IEEE, Vol. AP—33 (1985), pp.566—570.

Eindhoven University of Technology Research Reports
Faculty of Electrical Engineering

ISSN 0167-9708
Coden: TEUEDE

(222) Jóźwiak, L.
THE FULL-DECOMPOSITION OF SEQUENTIAL MACHINES WITH THE SEPARATE REALIZATION OF THE NEXT-STATE AND OUTPUT FUNCTIONS.
EUT Report 89-E-222. 1989. ISBN 90-6144-222-2

(223) Jóźwiak, L.
THE BIT FULL-DECOMPOSITION OF SEQUENTIAL MACHINES.
EUT Report 89-E-223. 1989. ISBN 90-6144-223-0

(224) Book of abstracts of the first Benelux-Japan Workshop on Information and Communication Theory, Eindhoven, The Netherlands, 3-5 September 1989.
Ed. by Han Vinck.
EUT Report 89-E-224. 1989. ISBN 90-6144-224-9

(225) Hoeijmakers, M.J.
A POSSIBILITY TO INCORPORATE SATURATION IN THE SIMPLE, GLOBAL MODEL OF A SYNCHRONOUS MACHINE WITH RECTIFIER.
EUT Report 89-E-225. 1989. ISBN 90-6144-225-7

(226) Dahiya, R.P. and E.M. van Veldhuizen, W.R. Rutgers, L.H.Th. Rietjens
EXPERIMENTS ON INITIAL BEHAVIOUR OF CORONA GENERATED WITH ELECTRICAL PULSES SUPERIMPOSED ON DC BIAS.
EUT Report 89-E-226. 1989. ISBN 90-6144-226-5

(227) Bastings, R.H.A.
TOWARD THE DEVELOPMENT OF AN INTELLIGENT ALARM SYSTEM IN ANESTHESIA.
EUT Report 89-E-227. 1989. ISBN 90-6144-227-3

(228) Hekker, J.J.
COMPUTER ANIMATED GRAPHICS AS A TEACHING TOOL FOR THE ANESTHESIA MACHINE SIMULATOR.
EUT Report 89-E-228. 1989. ISBN 90-6144-228-1

(229) Oostrom, J.H.M. van
INTELLIGENT ALARMS IN ANESTHESIA: An implementation.
EUT Report 89-E-229. 1989. ISBN 90-6144-229-X

(230) Winter, M.R.M.
DESIGN OF A UNIVERSAL PROTOCOL SUBSYSTEM ARCHITECTURE: Specification of functions and services.
EUT Report 89-E-230. 1989. ISBN 90-6144-230-3

(231) Schemmann, M.F.C. and H.C. Heyker, J.J.M. Kwaspen, Th.G. van de Roer
MOUNTING AND DC TO 18 GHz CHARACTERISATION OF DOUBLE BARRIER RESONANT TUNNELING DEVICES.
EUT Report 89-E-231. 1989. ISBN 90-6144-231-1

(232) Sarma, A.D. and M.H.A.J. Herben
DATA ACQUISITION AND SIGNAL PROCESSING/ANALYSIS OF SCINTILLATION EVENTS FOR THE OLYMPUS PROPAGATION EXPERIMENT.
EUT Report 89-E-232. 1989. ISBN 90-6144-232-X

(233) Nederstigt, J.A.
DESIGN AND IMPLEMENTATION OF A SECOND PROTOTYPE OF THE INTELLIGENT ALARM SYSTEM IN ANESTHESIA.
EUT Report 90-E-233. 1990. ISBN 90-6144-233-8

(234) Philippens, E.H.J.
DESIGNING DEBUGGING TOOLS FOR SIMPLEXYS EXPERT SYSTEMS.
EUT Report 90-E-234. 1990. ISBN 90-6144-234-6

(235) Heffels, J.J.M.
A PATIENT SIMULATOR FOR ANESTHESIA TRAINING: A mechanical lung model and a physiological software model.
EUT Report 90-E-235. 1990. ISBN 90-6144-235-4

(236) Lammers, J.O.
KNOWLEDGE BASED ADAPTIVE BLOOD PRESSURE CONTROL: A Simplexys expert system application.
EUT Report 90-E-236. 1990. ISBN 90-6144-236-2

(237) Ren Qingchang
PREDICTION ERROR METHOD FOR IDENTIFICATION OF A HEAT EXCHANGER.
EUT Report 90-E-237. 1990. ISBN 90-6144-237-0

Eindhoven University of Technology Research Reports
Faculty of Electrical Engineering

ISSN 0167-9708
Coden: TEUEDE

(238) Lammers, J.O.
THE USE OF PETRI NET THEORY FOR SIMPLEXYS EXPERT SYSTEMS PROTOCOL CHECKING.
EUT Report 90-E-238. 1990. ISBN 90-6144-238-9

(239) Wang, X.
PRELIMINARY INVESTIGATIONS ON TACTILE PERCEPTION OF GRAPHICAL PATTERNS.
EUT Report 90-E-239. 1990. ISBN 90-6144-239-7

(240) Lutgens, J.M.A.
KNOWLEDGE BASE CORRECTNESS CHECKING FOR SIMPLEXYS EXPERT SYSTEMS.
EUT Eeport 90-E-240. 1990. ISBN 90-6144-240-0

(241) Brinker, A.C. den
A MEMBRANE MODEL FOR SPATIOTEMPORAL COUPLING.
EUT Report 90-E-241. 1990. ISBN 90-6144-241-9

(242) Kwaspen, J.J.M. and H.C. Heyker, J.I.M. Demarteau, Th.G. van de Roer
MICROWAVE NOISE MEASUREMENTS ON DOUBLE BARRIER RESONANT TUNNELING DIODES.
EUT Report 90-E-242. 1990. ISBN 90-6144-242-7

(243) Massee, P. and H.A.L.M. de Graaf, W.J.M. Balemans, H.G. Knoopers, H.H.J. ten Kate
PREDESIGN OF AN EXPERIMENTAL (5-10 MWt) DISK MHD FACILITY AND PROSPECTS OF COMMERCIAL (1000 MWt) MHD/STEAM SYSTEMS.
EUT Report 90-E-243. 1990. ISBN 90-6144-243-5

(244) Klompstra, Martin and Ton van den Boom, Ad Damen
A COMPARISON OF CLASSICAL AND MODERN CONTROLLER DESIGN: A case study.
EUT Report 90-E-244. 1990. ISBN 90-6144-244-3

(245) Berg, P.H.G. van de
ON THE ACCURACY OF RADIOWAVE PROPAGATION MEASUREMENTS: Olympus propagation experiment.
EUT Report 90-E-245. 1990. ISBN 90-6144-245-1

(246) Maagt, P.J.L. de
A SYNTHESIS METHOD FOR COMBINED OPTIMIZATION OF MULTIPLE ANTENNA PARAMETERS AND ANTENNA PATTERN STRUCTURE.
EUT Report 90-E-246. 1990. ISBN 90-6144-246-X

(247) Jóźwiak, L. and T. Spassova-Kwaaitaal
DECOMPOSITIONAL STATE ASSIGNMENT WITH REUSE OF STANDARD DESIGNS: Using counters as sub-machines and using the method of maximal adjacensies to select the state chains and the state codes.
EUT Report 90-E-247. 1990. ISBN 90-6144-247-8

(248) Hoeijmakers, M.J. and J.M. Vleeshouwers
DERIVATION AND VERIFICATION OF A MODEL OF THE SYNCHRONOUS MACHINE WITH RECTIFIER WITH TWO DAMPER WINDINGS ON THE DIRECT AXIS.
EUT Report 90-E-248. 1990. ISBN 90-6144-248-6

(249) Zhu, Y.C. and A.C.P.M. Backx, P. Eykhoff
MULTIVARIABLE PROCESS IDENTIFICATION FOR ROBUST CONTROL.
EUT Report 91-E-249. 1991. ISBN 90-6144-249-4

(250) Pfaffenhöfer, F.M. and P.J.M. Cluitmans, H.M. Kuipers
EMDABS: Design and formal specification of a datamodel for a clinical research database system.
EUT Report 91-E-250. 1991. ISBN 90-6144-250-8

(251) Eijndhoven, J.T.J. van and G.G. de Jong, L. Stok
THE ASCIS DATA FLOW GRAPH: Semantics and textual format.
EUT Report 91-E-251. 1991. ISBN 90-6144-251-6

(252) Chen, J. and P.J.I. de Maagt, M.H.A.J. Herben
WIDE-ANGLE RADIATION PATTERN CALCULATION OF PARABOLOIDAL REFLECTOR ANTENNAS: A comparative study.
EUT Report 91-E-252. 1991. ISBN 90-6144-252-4